



HAL
open science

Glass processing with ultra short laser pulses

David Sohr

► **To cite this version:**

David Sohr. Glass processing with ultra short laser pulses. Physics [physics]. Université Claude Bernard - Lyon I, 2022. English. NNT : 2022LYO10039 . tel-04072596

HAL Id: tel-04072596

<https://theses.hal.science/tel-04072596>

Submitted on 18 Apr 2023

HAL is a multi-disciplinary open access archive for the deposit and dissemination of scientific research documents, whether they are published or not. The documents may come from teaching and research institutions in France or abroad, or from public or private research centers.

L'archive ouverte pluridisciplinaire **HAL**, est destinée au dépôt et à la diffusion de documents scientifiques de niveau recherche, publiés ou non, émanant des établissements d'enseignement et de recherche français ou étrangers, des laboratoires publics ou privés.



THESE de DOCTORAT DE L'UNIVERSITE CLAUDE BERNARD LYON 1

Ecole Doctorale N°52
Ecole Doctorale de Physique et Astrophysique

Discipline : Physique

Soutenue publiquement le 23/09/2022, par :
David SOHR

Glass processing with ultra short laser pulses

Devant le jury composé de :

CONSTANT Eric	Directeur de Recherche CNRS	Université Claude Bernard Lyon 1	Président
COURVOISIER François	Directeur de recherche CNRS	FEMTO-ST	Rapporteur
NOLTE Stefan	Professeur des Universités	Friedrich-Schiller Universitaet Jena	Rapporteur
KROKER Stefanie	Professeure des Universités	Physikalisch-Technische Bundesanstalt	Examinatrice
MOTTO-ROS Vincent	Maître de Conférences	Université Claude Bernard Lyon 1	Examineur
NUTER Rachel	Chargée de Recherche CEA	CEA-DAM	Examinatrice
SKUPIN Stefan	Chargé de recherche CNRS	Université Claude Bernard Lyon 1	Directeur de thèse
THOMAS Jens Ulrich	Chercheur principal	SCHOTT AG	Invité

ABSTRACT

Set in the wide and continuously growing field of glass processing with ultra short laser pulses, this work deals with the cutting and edge shaping of glass sheets. Laser beams with elongated focal geometries have previously been used to perforate even thick glass sheets with single laser shots and thus enabled fast and clean cutting processes. These line foci so far have been limited to straight geometries resulting in sharp edges, which for many applications require an extra processing step to obtain a c-cut edge. The c-shaped Airy beam on the other hand has been employed in ablative processes to create curved edges and trenches in thin sheets of silicon and diamond. This work describes the application of the Airy beam to the micro perforation cutting process in glass.

For this, the linear propagation of the Airy beam focus is reviewed with respect to the achievable length, curvature and focal contrast that depend on the focusing conditions. With an effective numerical aperture of 0.13 volume modifications of up to more than 2 mm length are demonstrated in borosilicate glass, that follow very well the expected parabolic trajectory of the Airy beam with a bending radius of 12 mm. Applying the Airy modifications for micro perforation for the first time, glass sheets with rounded edges have been achieved after etching with a bending radius down to 727 μm in a 600 μm thick sheet.

The most crucial limitation of the Airy beam with respect to the micro perforation process is the relatively low focal contrast that leads to absorption and material damage in the side lobes of the beam. This can be observed experimentally as an effective tilt of the Airy beam due to the preferential absorption in the upper part of the glass modification and is corroborated by non linear simulation results. Adjustments of the optical setup allow the compensation of this tilt and lead to the production of a symmetric edge.

The influence of the damage in the side lobes proves particularly problematic for separation by mechanical cleaving. Further adjustments of the Airy beam can be used to align the cracks that are caused by the laser perforation process along the intended cutting direction, i.e. orthogonal to the plane of maximum curvature. Going further, the Airy beam is a promising candidate for light sheet cutting, which will enable even faster micro perforation cutting processes by replacing the focal line with a focal surface. In this work, the first sheet like in-volume modification induced by a single laser shot is demonstrated.

Contents

1	Introduction	1
2	Micro perforation process and its physical background	5
2.1	Glass cutting by micro perforation	5
2.2	Beam shapes used for micro perforation	7
2.2.1	Bessel beam	7
2.2.2	Modified Bessel beam for improved glass cutting	9
2.2.3	Spherically aberrated Gaussian beam	11
2.3	Laser induced modifications for separation by cleaving and etching	13
2.3.1	Void and crack formation	13
2.3.2	Increased etch rate: selectivity	15
2.4	Energy deposition and its dependence on pulse duration	16
2.4.1	Plasma creation and relaxation	19
2.4.2	Modeling of non linear pulse propagation	22
2.4.3	Self focusing	24
2.4.4	Distributed shielding and intensity clamping	25
2.4.5	Damage thresholds at surface and in volume	26
2.4.6	Cumulative effects and burst mode	26
2.5	Summary	27
3	Linear propagation of the Airy Gauss beam and its experimental realisation	29
3.1	Paraxial Helmholtz equation	29
3.1.1	Gaussian beam	31
3.2	Fourier optics - spatial spectrum of the optical field	32
3.2.1	Fourier transform by a single lens	33
3.2.2	4f and 6f setup	34
3.2.3	Numerical simulation of linear light propagation	35
3.3	The 1D case: Airy beam and Airy Gauss beam	36
3.4	2D Airy Gauss beam	38
3.5	Direct space production of the Airy beam - 4f setup	42
3.6	Tools for wavefront modulation	43
3.6.1	Liquid crystal spatial light modulators	44
3.6.2	Diffraction optical elements and fixed phase masks	45
3.7	Measurements of Airy profiles in air	45
3.7.1	Effect of spherical aberration	46
3.8	Summary	50
4	2D Airy Gauss modifications and their application to glass cutting	51
4.1	Laser processing and beam imaging methods	51
4.2	Airy volume modifications	52
4.3	Cracks, surface effects and etching behaviour	57
4.4	Separation results	59
4.5	Energy deposition during non linear Airy propagation	61

4.6	Discussion	64
4.7	Summary	65
5	Improved glass cutting with a shifted Airy beam	67
5.1	Paraxial analysis of offset	68
5.2	Micromachining methods and results	70
5.2.1	Optical setup and volume modifications	70
5.2.2	Mechanical cleaving on a stepped roll	71
5.2.3	Adapted processing strategy for etching	73
5.2.4	Result after etching	74
5.3	Discussion	76
5.4	Summary	77
6	Perspectives in glass cutting	79
6.1	Oblong Airy	79
6.1.1	Experimental methods and results	81
6.1.2	Linear simulation results	82
6.1.3	Discussion	82
6.2	Light blade glass cutting	85
6.2.1	Beam shaping concept	85
6.2.2	Experimental setup and results	86
6.3	Summary	88
7	Conclusions	89
	Bibliography	91
A	Preliminary results with aspheres	103
B	Image Analysis	105
C	Calibrating the effective electron collision time	107
D	CurvedBeams	109
D.1	Multispot	109
D.2	Accelerated Bessel	110
D.3	Oblong Airy beam	111
	Acknowledgements	113

Chapter 1

Introduction

In the past two decades ultra short pulsed lasers have become reliable, increasingly cheap and widely used tools in industry. The applications are manifold and reach from surface functionalization and permanent marking [Ala+19; LAS22] and micro machining of complex 3D structures [Got13; 3D] to writing of internal structures in dielectrics. Examples for internal structuring include wave guides or photonic structures for integrated optical circuits and data storage [Miu+98; Gle+96; Mic22] and micro welding of these brittle, transparent materials [RNT12; SCH22g]. One field that has also profited particularly from the availability of ultra short pulsed lasers is the laser cutting of glass sheets [NLS13; Dud+20].

Glass sheets are present in a broad range of products, for example as simple decor glass in home appliances, as cover glasses in smartphones or as interposers in integrated electronic devices [Kur+16]. Other rising fields that rely on the transparent and inert character of glass and that use glass sheets are biomedical, micro fluidic and sensor applications. Common to nearly all of these applications is the requirement of robust edges, as these are particularly exposed parts of the sheet and a small crack once formed at the edge may quickly lead to catastrophic failure of the whole product due to the brittle behaviour of glass.

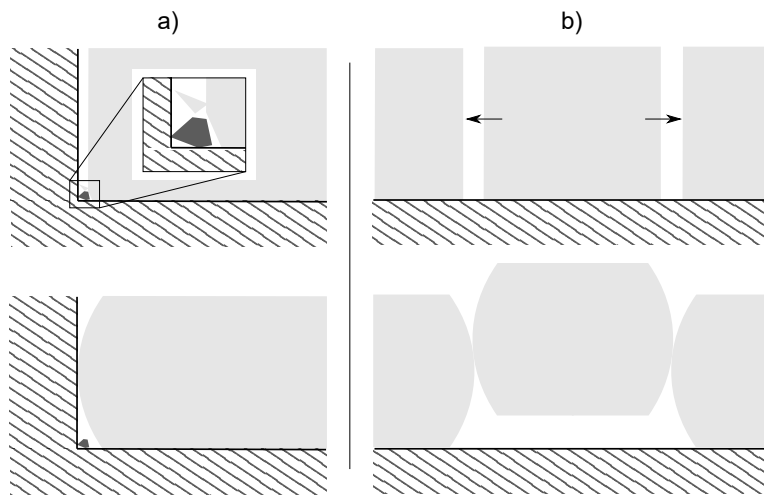


FIGURE 1.1: Two examples of improved handling of glass sheets with rounded edges: In comparison to straight edges these may lead to more accurate positioning at mechanical stops and avoiding of chipping due to debris (a) and a more tolerant, self adjusting flush positioning of parts (b).

Many glass products therefore are prepared with a chamfered or rounded edge, also referred to as pencil or c-cut [Swi17]. This increases the stability of the glass sheet, ensures a more accurate positioning at mechanical stops and can lead to a more robust flush joining of mechanical parts, see Fig. 1.1. This aspect is particularly important in the context of automation and high throughput analysis, for example in biomedical applications, which usually deal with sheet thicknesses reaching from

100 μm (microscopy cover glass) to 1 mm (microscope slide) [SCH22e]. C-cut edges also reduce cutting hazards and improve the aesthetic appearance, mostly relevant the decorative applications that use glass sheets which reach several millimetres in thickness [SCH22a]. The production of ultra thin glass sheets down to 30 μm or less on the other hand is motivated by the current trend towards foldable displays [SCH22h; Nip22]. Cover glasses provide protection for the display and the premium touch that is sought by consumers. The small bending radii that the glass sheet needs to support over years of use, poses particularly high requirements on the edge strength of those ultra thin sheets.

At the same time most products require flexible contour geometries, for example including cut outs for speakers and buttons in smartphones, smooth integration of displays and mechanical elements in automotive cockpit surfaces or application specific geometries in micro fluidics. The production of round contours, especially if high precision and small radii are required, is challenging if not impossible with mechanical cutting processes such as scribe and break techniques and usually requires additional mechanical grinding, which is a time consuming process associated with debris produced by abrasion of both glass and tools.

Many processes which required mechanical abrasion of the work piece are now performed by the interaction of photons with the material. A particular feature of the laser foci that replace the mechanical tools is that they can modify directly the interior of transparent workpieces. While ultra short laser pulses can also be used for abrasive glass cutting processes that employ ablation, a much cleaner and often faster process is provided by micro perforation of the work piece. For this, elongated line foci are used to weaken the work piece throughout its entire thickness and the glass is subsequently separated along the weakened surface, usually by direct mechanical cleaving or by etching. This way free form cuts can be performed along nearly arbitrary contours [SCH22f].

The non linear absorption that is responsible for the deposition of energy, which causes the material modification, is only achieved at very high intensities beyond ca. 10 TW/cm². The intensity distribution of the laser beam thus crucially determines the spatial distribution of the material modification. A large amount of research has therefore been dedicated by several companies and research groups in the past decade to the development of novel beam shaping concepts, that yield specific laser focus geometries to improve existing processes [HH12; Dud+19; Mey+17a; Jen+20; Bel+21; UL21; Fla+22].

The available pulse energy provided by industrial laser sources is continuously rising and thus enables fast processing of increasingly thick glass sheets by increasing the length of laser line focus [Sar+19]. On the other hand, a high lateral localization is required to avoid unwanted damage of the work piece and to achieve precise machining results. Quasi non-diffracting beams like the Bessel-Gauss beam exhibit a lateral intensity profile that remains unchanged over propagation distances that are far greater than the extent of their main lobe [Mar+01], meaning that they can easily be scaled up to provide a highly confined material modification with a length that is principally only limited by the size of the optics and the laser pulse energy.

The edges resulting from micro perforation cutting have a surface appearance that corresponds to fine sanding, with a surface roughness of ca. 1 μm , which in principle saves the extra grinding step that follows conventional cutting.

At the start of this project, however, micro perforation beam shapes were limited to straight geometries and the production of a rounded edge therefore required an additional grinding process. Going beyond the conventional mechanical grinding, rounded edges produced by an ablative laser process had previously been demonstrated in thin sheets of diamond and silicon employing the curved line focus of the 2D Airy-Gauss beam [Mat+12]. In this project, the 2D Airy-Gauss beam is combined with the focusing conditions of the micro perforation process to obtain a rounded edge as a direct result of the laser process.

The 2D Airy-Gauss beam can be produced as the Fourier transform of a Gaussian beam with a cubic phase along two orthogonal directions respectively [Siv+07]. The main lobe of the focused beam follows a parabolic trajectory in the mirror plane of the cubic phases and the resulting line focus has a length and curvature that are determined by the focusing conditions. For glass cutting

applications, a large length, high curvature and a high confinement would be favourable. However, they cannot all be maximized at the same time. In this work, the trade-offs between those parameters and their limitations are addressed, see chapter 3.

Also using the Airy beam, glass modifications have previously been demonstrated that follow the expected curvature for length in the range of few tens of μm [Fro+11]. Going to higher energies and longer focal lengths, volume modifications in borosilicate are demonstrated here that match the expected Airy profile with lengths of up to more than 2 mm and a bending radius of 12 mm, see chapter 4.

As a crucial deviation from the linear propagation profile, there is a preferential absorption in the upper part of the glass sheet and the modification in the lower part is suppressed. Also, a strong dependence of the modification morphology on the pulse duration is observed. Numerical simulations with an unidirectional pulse propagation model, that has previously successfully been applied to the non linear propagation of Bessel beams in similar focusing conditions [Mis+17], indicate that the ignition of plasma in the side lobes of the beam is responsible for both the observed asymmetry and the pulse duration dependence of modification morphology.

For a modification that penetrates the full thickness of a glass sheet also the interaction of the glass surface and the laser pulse needs to be taken into account. Various combinations of pulse energy, pulse duration, number of pulses in a burst and focus position within the glass were tested and the surface and volume modifications inspected by optical microscopy. The laser parameters and focusing conditions had to be finely tuned to achieve a continuous modification and at the same time avoid excessive damage in the side lobes of the beam to produce a well defined, rounded edge in a $525\ \mu\text{m}$ thick glass sheet could be produced by etching, as first demonstration of single pass cutting with the Airy beam. For this result, the linear focus had to be placed beneath the centre of the glass sheet to achieve a sufficiently evenly distributed material damage throughout the sheet. The resulting edge is asymmetric - effectively tilted with respect to the glass sheet.

A particular feature of the Airy beam, which in previous work has been called "ballistic control" [Hu+12], can be used to compensate the observed tilt, which is discussed in chapter 5. For this, the Gaussian input beam is moved laterally with respect to phase mask and microscope objective. At the focus, the intensity distribution is effectively shifted along the Airy parabola as a result of the Gaussian offset. Here, an intuitive description of the tilt is derived in terms of the low order aberration that are induced by this offset. The expected shift is confirmed in volume modifications. This effect is used to position volume modifications symmetrically in a $920\ \mu\text{m}$ thick glass sheet and thus a well defined, symmetric edge can be obtained after etching.

Mechanical cleaving along a curved surface turns out to be challenging. Here, the partial results that could be achieved with the 2D Airy Gauss beam are presented. Cracks along the side lobes of the Airy focal line are identified as main problem for mechanical cleaving. In terms of beam shaping there are two solutions to improve the process: If the focal contrast is increased, the energy deposition in the side lobes can be reduced. Alternatively, it would be favourable to align the cracks along the intended cutting direction. Several such concepts have previously been proposed for the Bessel beam.

The "oblong" Airy proposed by Ungaro and Liu [UL21] briefly after the publication of the first Airy cutting result achieved in this project combines both solutions and they demonstrate a mechanically cleaved edge after micro perforation with an Airy beam. For this they use the standard 2D Airy phase mask in combination with an input beam that is elongated along the mirror plane of the Airy beam. The propagation properties of this beam shape, in particular the contrast along the propagation, are examined here by means of numerical simulation and experimental imaging of the linear propagation in air. The oblong Airy beam is identified as the transition between the 2D Airy Gauss beam and an 1D Airy light sheet in chapter 6.

As a potential game changer in high throughput laser cutting of transparent materials, the concept of light sheet cutting [Ort+22b] is introduced here and in volume surfaces, i.e. 2D areas within

the volume of the glass sheet, are demonstrated that have been modified by a single laser shot respectively.

During this project two peer reviewed articles have been published [STS21c; STS22a] and patent applications in seven patent families have been submitted. In addition to the creation of curved edges by cutting with an Airy beam as discussed in this work [OST20] these deal with improvements of the laser process in combination with etching [Ort+20; Ort+22a], the production of wave guides [Kog+20] and improved cutting processes, that make use of the asymmetric lateral intensity distribution of the Airy beam [SWO20; SKN20].

This thesis sets out with a description of the micro perforation process in chapter 2, along with a review of the most important beam shapes, in particular the Bessel beam and its variations. The mechanisms that govern the energy deposition during the process and the resulting modification types and their scaling are presented as well in this chapter. Chapter 3 deals with the linear propagation of light as basis for beam shaping concepts and introduces the optical Airy beam in detail, showing how it is generated and how the focusing parameters can be used to scale the resulting line focus. The measurements of the linear propagation in air are also shown here. Chapter 4 deals with the micro machining with the standard 2D Airy-Gauss beam and the non linear simulations that are used to resolve the non linear propagation effects of the Airy beam and and to understand better the observed morphology of glass modifications. In chapter 5 the geometrical model for the shifted Airy is presented as well as the micro machining methods and results that lead to the production of a symmetric edge. Chapter 6 provides an outlook, reviewing the properties of the oblong Airy beam and presenting the first application of a light sheet for micro perforation cutting.

Chapter 2

Micro perforation process and its physical background

2.1 Glass cutting by micro perforation

There is a broad range of ways in which lasers are used to cut sheets of brittle dielectrics such as glass [NLS13; Kum+14; Lop+t ; Dud+20]. In this work I use a cutting process that in previous work has been termed laser volume scribing [Dud+20] or sometimes filamentation [Coh18; AH17; HH12], although usually a linearly elongated laser focal line is used rather than an actual non linear filament, see Sec. 2.4.4. For this process, discrete laser shots are used to weaken the material along the intended cutting surface throughout the sheet, see Fig. 2.1. For suitable focusing conditions and a resulting line focus with sufficient length, the material volume that is weakened by a single laser shot may extend through the entire depth of the work piece. This enables single pass cutting, where any lateral position along the intended cutting surface only needs to be irradiated once. The process time then depends only on the velocity with which the contour can be written. In principle this velocity v is limited by the distance between neighbouring modifications, the pitch p , and the pulse repetition rate of the laser source f_{rep} to a maximum value $v_{\text{max}} = p \times f_{\text{rep}}$. In many cases, however, the velocity is limited by the ability of the mechanical setup to position the sample with the required spatial accuracy¹. If multiple passes at different depths within the work piece are required to achieve a modification of the desired length, the processing time increases accordingly.

After laser processing the work piece can be separated accurately along the weakened surface either by mechanical breaking (cleaving) or etching. A related process is stealth dicing [Kum+07], where the work piece is usually not modified throughout its entire thickness, but sometimes this term is also used for the process that here is referred to as micro perforation [Mey+19].

The laser perforation itself is a kerf-less cutting process and hardly produces any debris, in contrast to, for example, cutting by rear side ablation [Dud+20]. This is despite the fact that in typical cutting regimes the modification also includes the formation of a void, see Fig. 2.2. Mass measurements of highly perforated sheets indicate that the mass loss during the laser perforation is negligible and the material is moved from the void into a surrounding densified zone [Sch17; Ber+18a], see Sec. 2.3.1 for more details.

For industrial applications it is favourable if the sample can be separated by cleaving, in particular, if this can be done in an automated fashion, e.g. by thermal crack propagation with a CO2 laser [Lop+t ; HH12]. In some cases even a direct self-separation after the USP laser process has been recorded in chemically strengthened glass [Mis+16].

However, separation by etching can also be done on industrial scale and leads to particularly strong edges, as micro cracks that in many cases are introduced by the laser process and that lead to weakening of the edge are removed during etching. The edge strength², given in terms of a bending

¹For typical values, e.g. $p = 10 \mu\text{m}$ and $f_{\text{rep}} = 100 \text{ kHz}$ this yields $v_{\text{max}} = 1 \text{ m/s}$, which is only reached after 10 cm with a constant acceleration of 5 m/s^2 .

²Typically the edge is the weakest part of a glass sample due to the accumulated defects, which act as seeds for cracks. Removing those initial defects leads to a higher edge strength and a narrower distribution of failure stresses [DJ20].

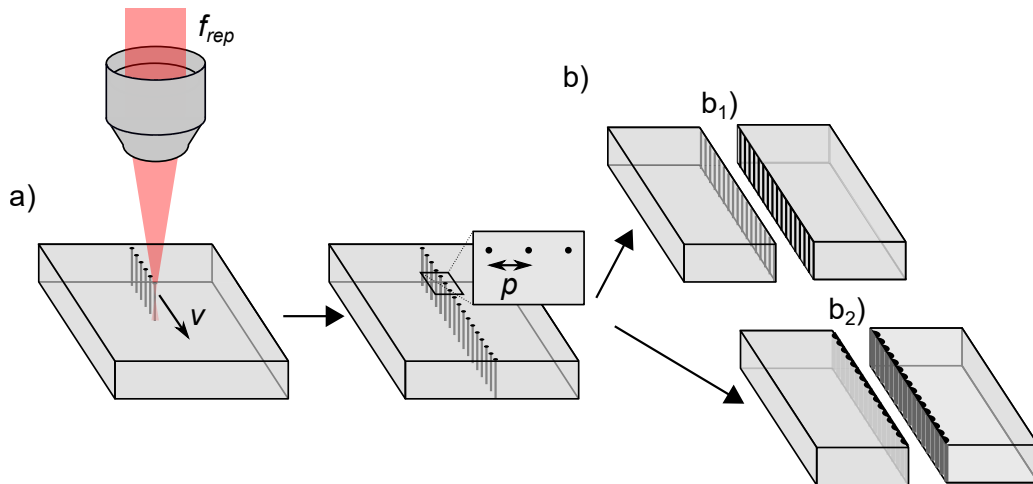


FIGURE 2.1: Schematic representation of the cutting process, starting with the laser structuring (a) for which a focal line of a pulse laser with repetition rate f_{rep} is moved horizontally relative to the sample along the intended cutting contour with speed v , resulting in a weakened surface throughout the material that is defined by distinct modifications separated by a pitch p . In a second step (b) the sample is separated either by mechanical cleaving (b_1) or etching (b_2).

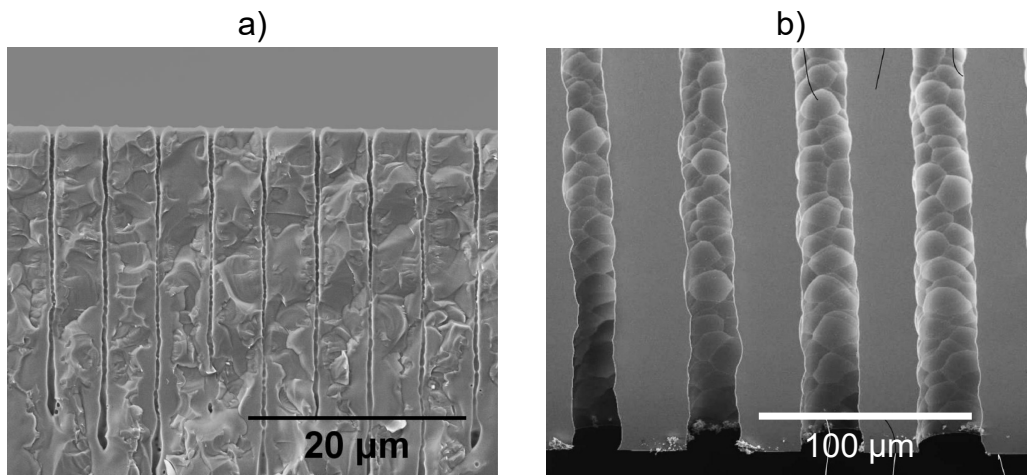


FIGURE 2.2: Scanning electron microscope (SEM) images of a glass edge produced by laser perforation and mechanical cleaving (a) [Sch17] and a partially etched perforation line (b) [Ort+18b] produced with a straight line focus. In (a) the equally spaced, elongated voids produced by the laser process can be seen, as well as the irregular cracks that connect them. (b) shows the typical bubble like cup structure within the etched channels.

stress, is typically determined by bending trials, e.g. in a four point bending setup [Dud+20].

The edges after mechanical cleaving have a surface roughness of about $1\ \mu\text{m}$ or less, in particular when the cracks that are created by the laser shots respectively can be aligned along the intended cutting direction [Mis+17], also see Sec. 2.3.1.

An elongated focal line is needed to enable the fast single pass glass cutting mentioned above. On the other hand, a confined mechanical damage is necessary to avoid weakening or even breaking the final workpiece. Industrial laser sources usually provide a beam with a Gaussian profile. For a Gaussian beam of a given wavelength however, the depth of focus and the transversal beam waist, i.e. length and width of the focal volume, are directly coupled and an increase in length would simultaneously lower the confinement. Other beam geometries on the other hand can be obtained by using bulk optics, such as for example a conical lens, a so called axicon, but also other phase changing elements can be used for this purpose, such as spatial light modulators or diffractive optical elements, see Sec. 3.6.

Several aspects relevant for glass cutting can be considered when designing these beam geometries. In particular, depending on the beam shape length and width of the focal volume can be adjusted independently, effects like the distributed plasma shielding can be reduced by going from a mostly on-axis energy flow to a increased lateral energy flow and even curved line geometries can be achieved. These adaptations of the beam shape provide the central tool for more robust and versatile laser cutting process. Here we will consider a selection of beam shapes that previously have been used for this cutting process, before reviewing the fundamentals of beam shaping together with the Airy beam in chapter 3.

2.2 Beam shapes used for micro perforation

The necessary tool for the cutting process as described in Sec. 2.1 is an extended laser focus geometry, a focal line, that enables fast processing of large depth ranges with a single laser shot. The design of such focal lines is a fundamentally different task to optical imaging, which is concerned with an accurate representation of an image in the transversal focal plane. Laser beam shaping for glass cutting on the other hand requires control over an extended volume, especially in the case of accelerated beams, see chapter 3 and appendix D. A high lateral localization of the main lobe of the intensity distribution and a broad, preferably constant intensity of the main lobe along the beam propagation direction are favourable for these applications.

Quasi non-diffracting beams are particularly interesting with respect to these demands, as they exhibit a constant lateral intensity profile over propagation distances that are far greater than the extent of their main lobe. For simplicity these beams are often referred to as non-diffracting beams, which are their theoretical base models, that can carry infinite amount of energy and thus truly remain non-diffracting over arbitrarily large distance. Physical beams in contrast will always be apodized and the beam will only exhibit non-diffracting features over a limited propagation distance.

2.2.1 Bessel beam

The Bessel beam and also its apodized variation, the Bessel-Gauss beam are among the first non-diffracting beams that were already theoretically described and experimentally demonstrated in 1987 [DME87]. The name of the beam relates to the focal electric field profile, that is described by the zero order Bessel function of the first kind $J_0(x)$. Corresponding to the Fourier transform of a ring, this focal profile can be created by imaging a ring aperture with an ideal lens, also see Sec. 3.2, but this would mean wasting large portions of the laser power³ and in practice it is nearly always

³In particular when one tries to approach the ideal Bessel beam, which corresponds to an infinitely thin ring.

produced in direct space, by adding a conical phase to the input beam. This conical phase can be produced by an axicon, a conical lens, see Fig. 2.3.

The resulting lateral intensity profile of the ideal Bessel beam

$$I(\rho) = |A_0|^2 J_0^2(k_T \rho) \quad (2.1)$$

has a pronounced central peak, which exceeds the first ring by a factor of 6.2, thus yielding a good focal contrast⁴. The radius of the central lobe

$$w_B = \frac{2.40}{k_T} = \frac{1.2\lambda}{\pi \sin(\theta_B)} \quad (2.2)$$

depends on the laser wavelength and the Bessel cone angle θ_B . Short wavelengths and high Bessel cone angles thus lead to a high confinement of the laser pulse energy, which is favourable for material processing, for example see [Mey+19].

The Bessel beam is called non-diffracting, because its transversal intensity profile does not change during propagation. The propagation invariance of the ideal Bessel beam can be understood in terms of its plane wave components, also see Sec. 3.2. These all have the same longitudinal wave number and thus there is no relative phase shift. The transform function of propagation Eq. 3.27 then reduces to a phase term, that changes linearly with z but is constant in the transversal plane and can thus be neglected, also see [Goo17].

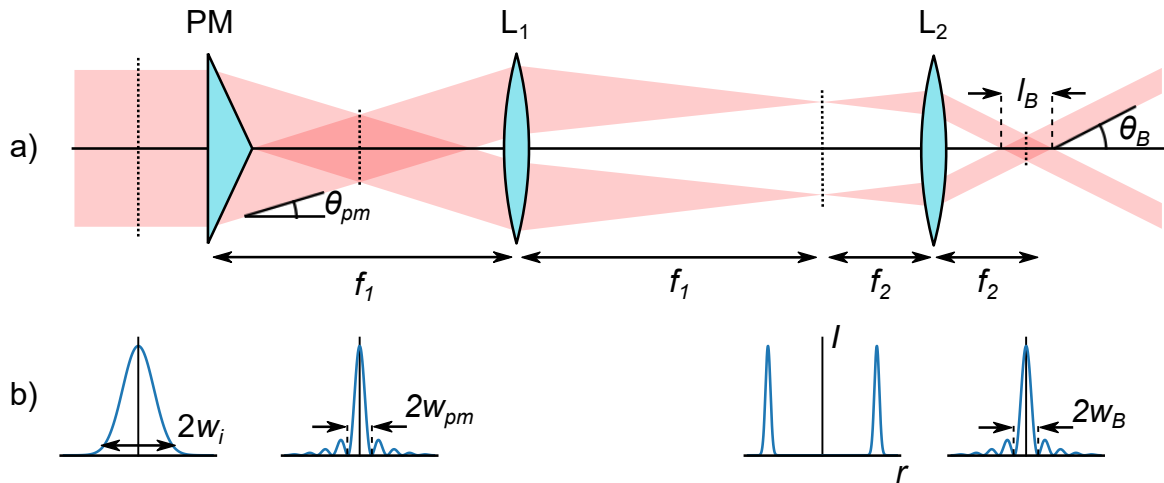


FIGURE 2.3: Optical setup for producing a Bessel Gauss beam (a) and schematic lateral cross sections of the intensity distribution (b) at the positions marked by the dotted lines respectively. The Bessel distribution right behind the phase mask PM is demagnified by a factor $M = f_2/f_1$ for material processing by a telescope setup with two lenses L_1 and L_2 . The Bessel cone angle $\theta_B = \theta_{PM}/M$ increases compared to the angle behind the phase mask θ_{PM} while the length l_B and the width w_B decrease for $f_2 < f_1$.

In practice, the beam has a finite extent which is determined by the width of the input beam w_i . For typical beam diameters this does not significantly affect the centre of the lateral intensity profile, i.e. the focal contrast or the main lobe diameter. The longitudinal intensity profile of the main lobe, however, strongly depends on the width and shape of the input beam [GGP87]. Apart from diffraction effects at the apex, that lead to a finite slope in the on-axis intensity right behind the axicon, it can be understood as the projection of the radial input beam profile onto the propagation axis, also see Sec. 2.2.2, so that the length can be estimated as $l_B = w_i / \cos(\theta_B)$. As the cone angle should be maximized for a narrow central peak, a large beam width is needed for producing long focal lines for material processing. Therefore one crucial limit for material processing is the size of the optics.

⁴Even higher focal contrasts have been reported for modified versions of the Bessel beam [Fla+19].

With current optics aspect ratios l_B/w_B exceeding 10,000 are readily reached [Mey+19]. The other important limitation of cutting applications is the pulse energy, as a sufficiently large intensity needs to be reached to produce the mechanical damage needed for separation. The length of modifications produced by a Bessel beam can be very well modeled by applying a constant threshold intensity to the linear propagation profile [Ber+18b; Feu+19].

Glass cutting of sheets with a thickness of up to 12 mm has been demonstrated with Bessel Gauss beams [Mey+19; Feu+19; Jen+20].

Another aspect that makes the Bessel beam particularly interesting for glass cutting is that its transversal intensity profile reconstructs behind obstacles in the beam path [MD05]. This property is due to the lateral energy flow towards the focal region and is often referred to as "self-healing", a feature shared with other non-diffracting beams, such as the Airy beam.

2.2.2 Modified Bessel beam for improved glass cutting

Several modifications of the Bessel beam and Bessel based beam shaping concepts have been proposed for improving its performance in glass cutting or adapting it to custom needs [Fla+19]. Two aspects that can be generalized to other beam shapes will be presented for the Bessel beam, which has been most extensively studied.

Intensity flattening The variation of the main lobe intensity along the propagation, i.e. the longitudinal contrast, can require a high pulse energy to ensure that the intensity exceeds the threshold for material damage at all depths within the sample. Despite the relatively large focal contrast of the Bessel beam, this can lead to unwanted effects such as distributed shielding, see [Mis+17] and Sec. 2.4.4, or excessive damage at the position of peak intensity. Lowering the longitudinal contrast along the focal line, i.e. flattening or homogenizing the longitudinal intensity profile, means that the peak intensity can be lowered while the lowest intensity in the specified region still exceeds the threshold for material modification. For example, for an ideal top hat distribution, the length of the modification will not any longer depend on the pulse energy, but the length of the top hat will be limited by the available pulse energy. This concept has been included in industrial glass processing optics [Fla+19].

This industrial realization is based on concepts for constructing arbitrary on-axis intensity distributions by combining ideal or apodized Bessel beams [ZR04; Dar+06]. First analytically derived expressions for phase delay required for constant on axis description by a direct energy mapping from an annulus in the input plane to an on-axis segment and their experimentally realisations by binary DOEs have been published 30 years ago [Soc+92].

More recently, iterative methods have been proposed and realized experimentally for an on-axis intensity shaping both with static, diffractive optical elements [Osi+10] and active spatial light modulator, which can even correct for non-uniform input beams [OI+16].

Preferential crack orientation Mechanical separation after laser modification with a line focus relies on the weakening of the material along the intended cleaving surface. For beams with rotational symmetry as the Bessel beam, however, the cracks that are created in the material for high pulse energies are oriented in various random directions [Dud+18]. This can lead to crack propagation to either side of the intended surface during separation, so that a small separation of the modifications, i.e. a small pitch, is required for a clean cut.

Defining a preferential direction by breaking the rotational symmetry of the beam can both lower the force required for separation, i.e. improve separability [Jen+20; Mey+17a], and also increase the strength of the resulting edge [Mey+17a]. The pitch, and thus also the processing speed⁵, can be increased and for mm thick sheets of Borofloat[®] 33 the separation force was even decreased when

⁵If the laser is used at its maximum repetition rate, which is rarely the case.

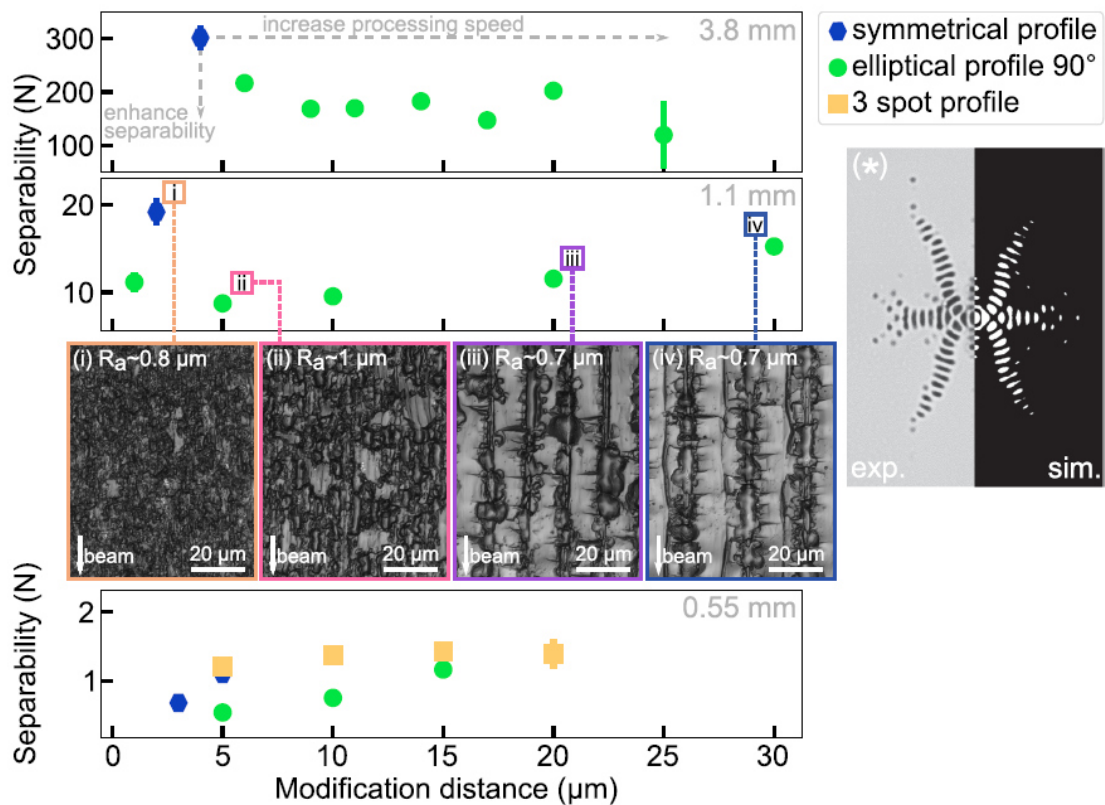


FIGURE 2.4: Separability of glass sheets of three different thicknesses for three Bessel based beam profiles and varying modification distance (pitch) [Jen+20]. One can see that with the elliptical profile the force needed for separation ("separability") is lower for all three samples at a given pitch and that cleaving with larger pitches is possible compared to the symmetrical profile. In the microscope images one sees extended areas of smooth fracture between of the laser induced channels for larger pitch (iii and iv). A three spot profile aligned along the cutting direction does not lead to a lower separability but also enables separation with a larger pitch compared to the symmetrical profile.

going changing the pitch from 5 μm to 30 μm , see Fig. 2.4. Although large portions of the cleaving surface are smooth for a large pitch, the mean surface roughness S_a is not significantly reduced [Jen+20]. Interestingly, the separability is not reduced for thin glass (550 μm).

Most commonly the preferential direction is defined by using a Bessel beam with an elliptical profile in lateral cross section. This can be obtained by using an axicon with an elliptical tip or tilting an axicon, both of which induce astigmatic aberrations in the beam profile [Dud+18; Dud+19]. Alternatively the ellipticity can be induced by blocking a rectangular region in the Fourier plane [Mey+17b], also see Sec. 3.2.2, by adding a constant phase to half of the Fourier plane⁶ or by specific phase mask design, which in fact enables a broad range of beam shapes [Jen+20].

The main mechanism for facilitation of glass cutting is the preferential crack orientation [DGR16; Jen+20], but also an enhanced stress localization at elliptical voids [Mey+17b] has been predicted by simulations⁷ and resulted in an improved separability [Mey+17a; Jen+20]. Interestingly the samples also cleave along the intended surface even when three voids are created that are aligned orthogonally to the cutting surface, compare [Mey+17b; Mey+17a], so that the ellipticity of the central void determines the cleavage plane. When the intensity is more evenly distributed across three focal lines [Jen+20], the set of voids is aligned with the cutting direction for the enhanced glass cutting, also see Fig. 2.4.

2.2.3 Spherically aberrated Gaussian beam

Similarly to the Bessel beam, spherical aberration can lead to an elongated focal line by constructive interference of light cones, see Fig. 2.5 a). In contrast to the Bessel beam those cones all have different cone angles. A beam with significant elongation of the on-axis intensity as shown in Fig. 2.5 b) and c) can be produced by focusing a Gaussian beam with a single spherical lens.

The on axis intensity shows the elongated focal distribution towards the lens and exhibits modulations, which are typically observed for spherical aberration. Another characteristic feature is the presence of a prominent Gaussian like peak at one end of the extended focal region. The transversal intensity profile in the tail on the other hand reminds of the Bessel beam, with pronounced concentric rings surrounding an narrow main lobe. Similarly to the Bessel beam [Ber+18b], the length of the modification increases with pulse energy⁸ and it can also be well described in terms of a constant intensity threshold, see Fig. 2.6.

⁶Amplitude glass module

⁷For simulations of von Mises stress at circular and elliptical modifications [Jen+20] assume a homogeneous decrease of Young's modulus (or void) shaped like the beam profile. For the prediction of the Young's modulus they refer to [AB15], which in turn validate the semi-empirical formula $E_{porous} = E_0(1 - p/p_c)^f$ [f depends on pore geometry] for porous, brittle material from [PN87], and combine this with observations of porous structures in silica waveguides written with fs lasers [Can+11]).

⁸These complementary results I have produced using the same industrial laser machine as for the main experiments in this study, see Sec. 4.1.

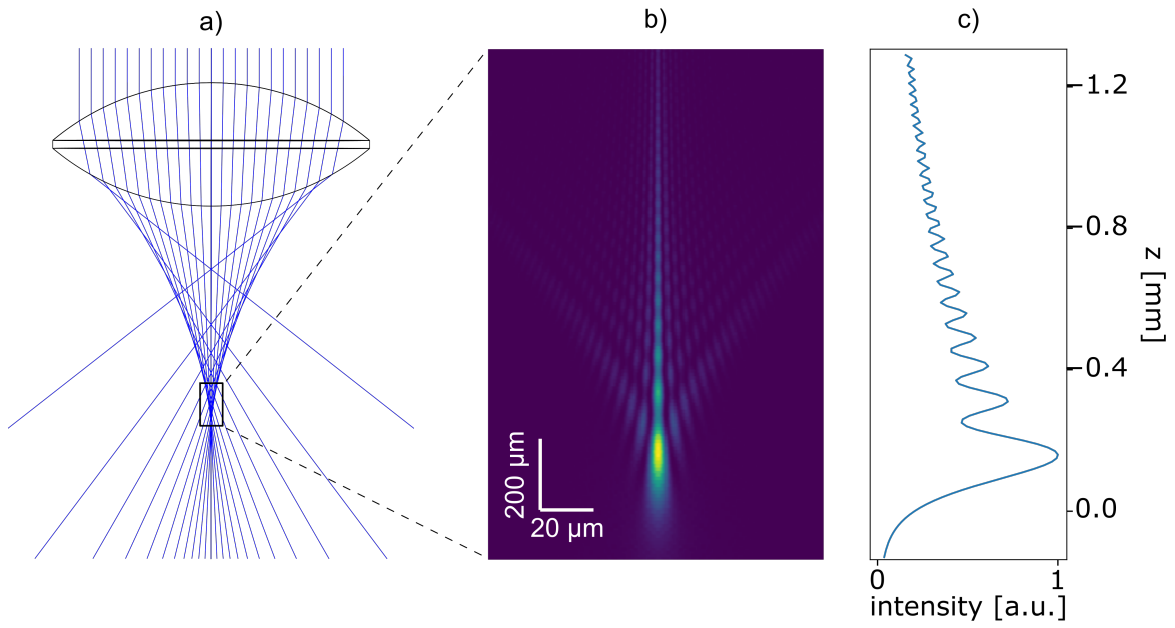


FIGURE 2.5: Ray trace representation (a), longitudinal cross section of the focal intensity distribution (b) and intensity profile on the optical axis (c) of a spherically aberrated beam produced by focusing a Gaussian beam with a biconvex lens. Note that the outer rays are focused closer to the lens and thus lead to an elongated focal intensity distribution.

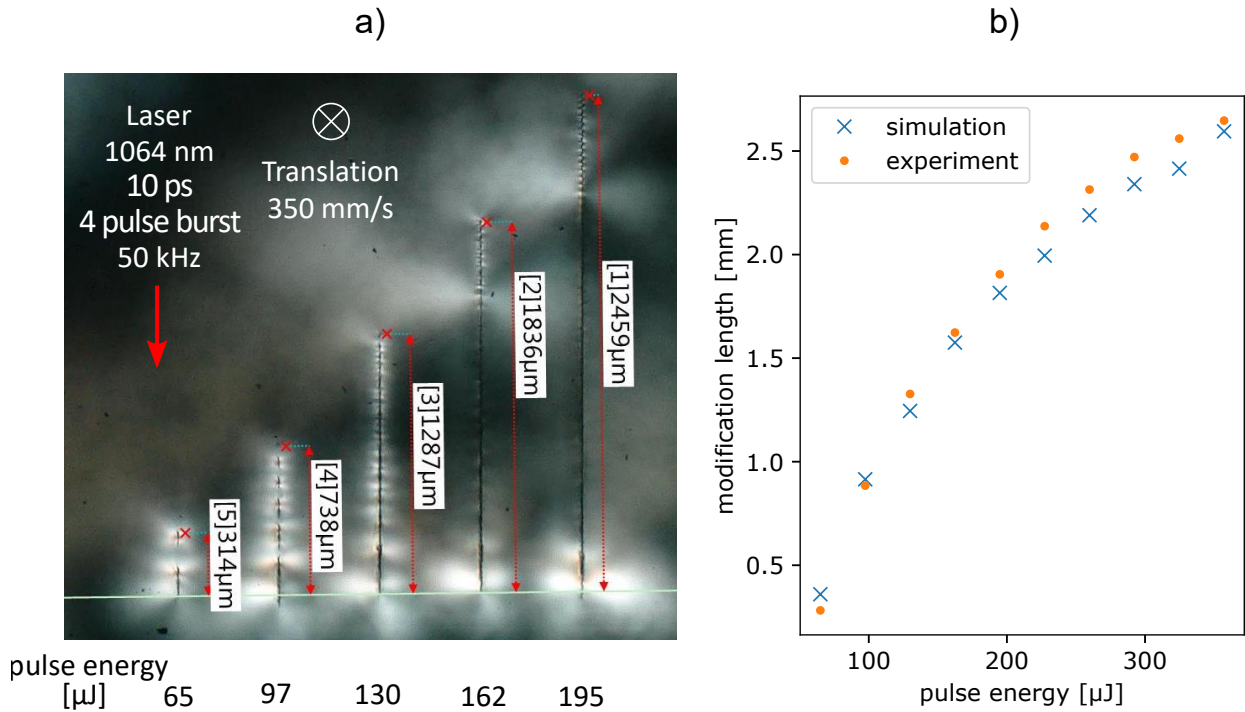


FIGURE 2.6: Microscopic cross section of glass modifications produced with a spherically aberrated lens (a) and comparison of measured modification lengths with length calculated from the linear intensity distribution for a constant damage threshold intensity $I_{th} = 4 \text{ TW/cm}^2$ (b).

2.3 Laser induced modifications for separation by cleaving and etching

The interaction of ultra short laser pulses with dielectrics can generate a wide range of modification types in dielectrics [Ito+06], ranging from local lattice defects [Mau+16; Vel+16] which can lead to colour changes [Lon+03] or a soft refractive index change at low pulse energies, to nano gratings within the material [Sud+99; Shi+03; Kaz+07] at intermediate energies and to significant mechanical disruption of the lattice, such as material removal (ablation) at the surface [Stu+96] or void and crack formation within the volume [Juo+06; Hen+16]. Here, we will review the modifications with respect to their use in the glass cutting process. Mechanical separation in the context of the micro perforation process generally relies on the presence of voids, cracks and stress fields as precursors for the intended catastrophic crack growth [Ber+18b; DGR16; Jen+20]. For etching, generally an enhanced local etching rate leads to the material removal that is needed for separation, but different types of modifications can lead to this increase, see Sec. 2.3.2.

2.3.1 Void and crack formation

Void formation as a result of a confined micro explosion induced by ultra short laser pulses has first been reported for 100 fs pulses in various dielectrics [GM98]. The void opening can be understood in terms of the rarefaction zone that follows a shock wave that radiates outward from the high energy laser interaction zone [Juo+06]. Driving pressures of up to several TPa have been reported in some cases [Gam+07]. However, it is questionable if for a system which is far from thermodynamic equilibrium, as is the interaction volume after irradiation with an ultrashort laser pulse [Ret+17], a macroscopic parameter such as pressure can be reliably applied by simply interpreting the energy density as pressure.

A frequently cited estimate of the size of shock affected region equates the absorbed energy with the elastic work done against the surrounding material for spherical geometries [Juo+06; HJM07]. For this they use the Young's modulus Y directly as a measure of the internal pressure of the material, against which the work is done. Following the same idea, but using instead the bulk modulus $B = Y/(3(1 - 2\sigma))$ [HJM07], which takes into account the lateral strain in terms of the Poisson's ratio σ and going to cylindrical coordinates for extended modifications produced by line focus geometries, an upper bound

$$r_{\max, \text{tr}} = \sqrt{\frac{E_{\text{abs}}}{\pi B}} \quad (2.3)$$

can be estimated for the radius of the transient void that is opened within the rarefaction zone behind the shock wave by equating the line density of absorbed energy E_{abs} and the elastic work that is needed to open a cylindrical void within a material with a Young's modulus Y . For the maximum line energy density obtained in our simulations, $110 \mu\text{J}/\text{mm}$, this yields $r_{\max, \text{tr}} \approx 990 \text{ nm}$. While the



FIGURE 2.7: Electron microscope top view (a) and optical microscopy longitudinal cross sections (b,c) of void in fused silica after laser processing with Bessel beam. The continuous character is shown by filling with water (c) [Bhu+14]

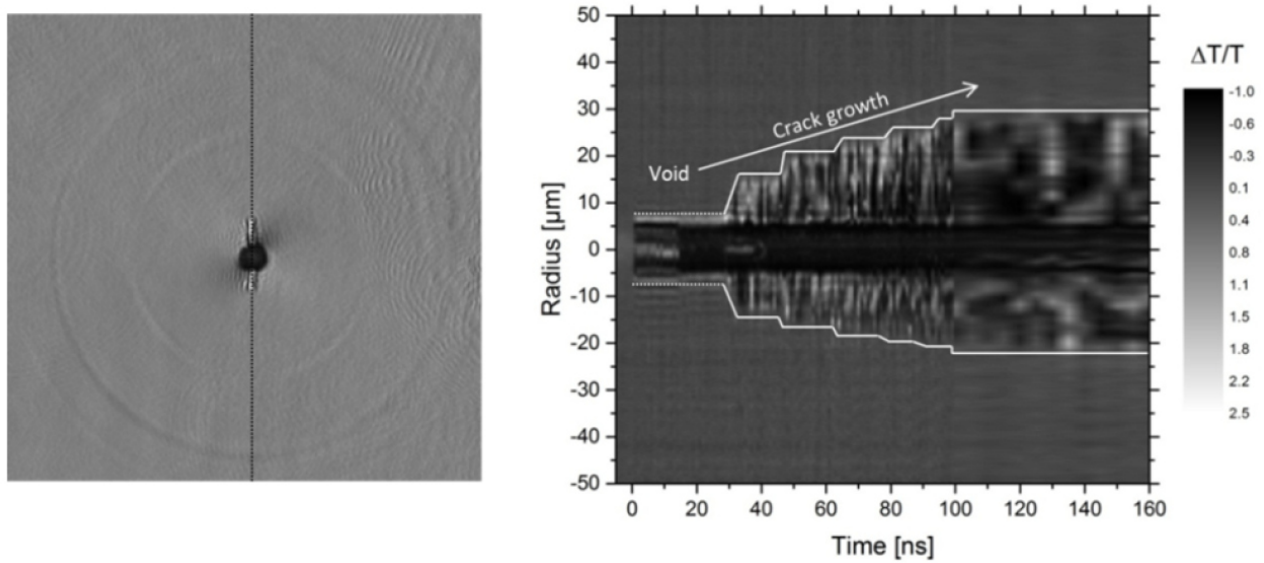


FIGURE 2.8: Top view (left) and cross section (right) of volume modification in soda lime glass produced by bursts of Gaussian pulses with NA 0.5, focal length 8 mm with $\tau_p = 350$ fs, $\lambda = 1040$ nm, $E_p = 13$ μ J and a pulse period within the burst of 13 ns. Image width on the left is ca. 200 μ m, note that the cross section is shown at a larger scale. The black line indicates the orientation and position of the cross section [Hen+16]. Note that the crack length increases in distinct steps, the timing of which corresponds well with the intra burst period.

shock wave itself is not observed experimentally, the sound wave that it relaxes to as it propagates outwards is a well reported observation in pump probe experiments [Hen+16; Ber+18a; AER18], also see Fig. 2.8. However, while experiments in fused silica demonstrate a linear scaling between $r_{\max, \text{tr}}$ and the final void radius, the void radius in glasses does not generally follow this scaling [HJM07]. This observation has been attributed to the mechanical relaxation of the glass. In particular they found a decrease of the threshold for void formation as the amount of a glass former (Si, Ge, P and B) in the glass composition increases.

Typical void diameters observed in dielectrics for processing with a line focus are in the range of 300 nm to 400 nm, see for example Fig. 2.7. While the formation of cracks during the laser process is notoriously difficult to simulate, hydrodynamic simulations have successfully predicted the opening and expansion of a void [Gam+07; Gam11; Bul+15; Beu+17; Beu19]. Depending on the model, the creation of an additional phase such as a gas phase in the void can not be described, but generally these simulations successfully predict a low density region with extents similar to the experimentally observed voids.

Even for continuous voids with a connection to the surface mass loss is minimal [Sch17]. Due to mass conservation the void therefore has to be surrounded by a densified region. This is predicted by the hydrodynamic simulations and has also been observed experimentally, for example by Brillouin-Scattering [Sch17]. Similar to the strengthening of glass, one might expect that this densification leads to a zone of compressive stress surrounding the void. If this compressive stress is not released, it might potentially cause cracks to run outside of the intended cutting line, see Fig. 2.9.

Different measures exist as proxies for the probability of crack formation during the laser process itself: It is modelled by compressive and shear stress [Beu+17], tensile stresses [Mis+17; Gri21] or maximum transient tangential strain [Kun18]. Experiments show a linear increase of crack length with laser pulse energy [DGR16]. Asymmetric intensity distributions of the laser beam or a rapid succession of closely spaced laser shots [Beu+18; Beu19] can lead to a localization of stress and strain and thus increase the probability of crack formation and at the same time control the orientation of the crack, see Sec. 2.2.2.

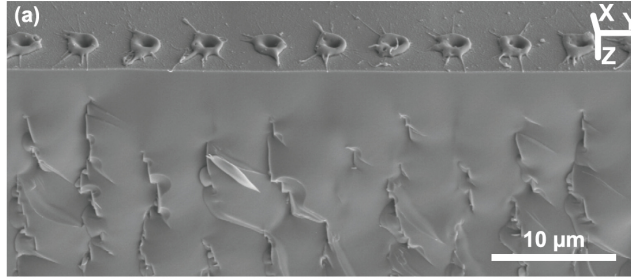
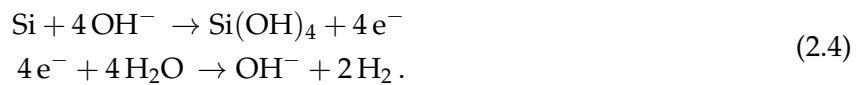


FIGURE 2.9: Cleaved glass sample laser processed with symmetric Bessel beam, showing a clear offset between the modifications and the crack [Mey+17a].

Microscope analysis of volume modifications The evaluation of modifications within the volume of the work piece can be challenging due to the difficult access and the small extent that renders creation of cross sections a tedious search. Electron microscopy (for example Scanning Electron Microscopy, SEM) is particularly useful to measure void diameters at the surface and to some extent can also be used to image cracks. A full tomographic characterization of a line modification can be obtained by stepwise mechanical surface removal [Liu+18], but this is very tedious. Previous work has shown that while phase contrast microscopy is needed to show soft refractive index changes (type I modifications) [Bhu+14; MB+08], optical transmission microscopy is suitable to detect stronger modifications that include mechanical damage [Bhu+14; Hen+16]. Comparison of optical and electron microscopy have shown for spherical voids, that the smallest optically recognizable voids typically had diameters of 100–150 nm [HJM07]. These values are in the range of the resolvable length scale predicted by Abbe’s formula $d = \lambda / (2 \text{NA})$ for optical light if objectives with high numerical aperture (NA), usually with oil immersion, are used.

2.3.2 Increased etch rate: selectivity

Using the increased etch rate in laser modified zones of glass is an established technique [Got13; Fla+15; But+21; BKM21] and applied in several industrial processes [Ort+18a; Kog+20; JW17; Lig21; LPK21]. The two predominantly used etching agents are hydrofluoric acid (HF) and potassium hydroxide (KOH) [But+21]. A more detailed discussion of the etching mechanisms and the etch rates for both agents is given in [Kiy+09]. Kiyama et al. attribute the increased etch rate of laser irradiated fused silica to the formation of silicon rich clusters, in which the silicon is dissolved by the reaction



The progress of the etching front, in dimensions length per time, measured along the laser modifications and normal to the surface for unstructured material is called etch rate. The absolute etch rate strongly depends on the parameters of the etching process such as concentration of etching agent and temperature and on the material itself. A more relevant parameter for etching of laser structured samples however is the selectivity S , that is the ratio between the etch rates of modified r_s and pristine material r_0 respectively [MJF14]. Studies on SLE usually do not vary the etching conditions, but focus on the dependence of the selectivity on the parameters of the laser process.

The selectivity is usually given as $S = (r_s + r_0) / r_0$ [MJF14; BKM21], when the progress of the etching front can be measured. Alternatively, the selectivity can be determined from the angle at the corner of the original and the newly created surface along the laser modification which is called taper, see Fig. 2.10 a). The taper can be used to estimate the selectivity as $S \approx \cot \theta_t$. This is particularly useful, when a laser modification in a thin sheet has been opened completely and the longitudinal etching rate r_s can not be determined, see Fig. 2.10 b). This method however is strongly limited by the angles that can reliably resolved and is insensitive for high selectivities.

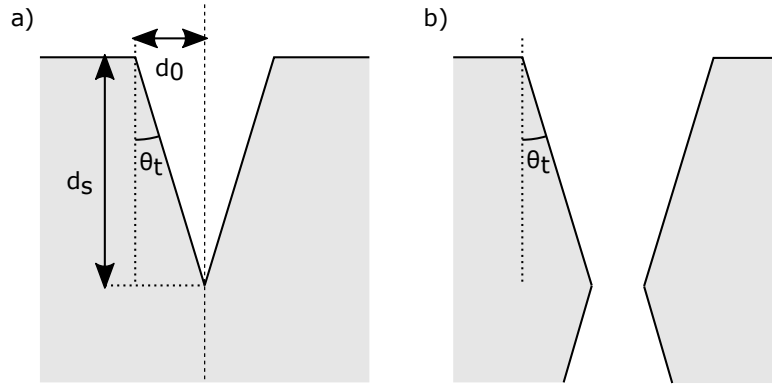


FIGURE 2.10: Schematic cross sections through the opening caused by etching along a thin laser modification (dashed line) demonstrating a) the relationship between taper θ_t and etching depths in unit time d_0 in pristine and d_s in modified and the laser modified material respectively. $d_s \gg d_0$, so that the selectivity is given by $S = d_s/d_0 = \cot \theta_t$. For an etched modification that completely penetrates a thin sheet (b) the etching depth d_s may not be measurable, but the selectivity S can still be estimated from the taper.

parameter	symbol	value	unit
refractive index at 587.6 nm	n_d	1.471	—
refractive index at 1030 nm	n_0	1.4625	—
Abbe number ($\nu_d = (n_d - 1)/(n_{F'} - n_{C'})$)	ν_d	67.3	—
Coefficient of Thermal Expansion (C.T.E.)	α	3.25×10^{-6}	K^{-1}
Thermal conductivity	λ	1.2	$\text{W}/(\text{m}\cdot\text{K})$
Specific heat capacity	c_p	0.83	$\text{kJ}/(\text{kg}\cdot\text{K})$
Density at 25°C	ρ	2.23	g/cm^3
Young's Modulus	Y	64	kN/mm^2
Poisson's Ratio	μ	0.2	—

TABLE 2.1: Optical, thermal and mechanical properties of Borofloat[®] 33 [SCH22c; SCH22d; SCH22b; Pol22]

The standard selective laser etching process (SLE) in fused silica relies on nano gratings, i.e. modifications without mechanical damage. In those, regions with reduced oxygen content readily react with the OH^- ions of the KOH solution. This way selectivities of over 1000 can be reached in fused silica [MJF14]. The preferential etching only of specific sub- μm regions and the dependence on the laser polarization is very well documented for HF etching of fused silica [Hna+06].

Hnatovsky et al. also report, however, that this process does not work for borosilicate glass: In BK7 they do not observe any nano gratings within their range of focusing conditions, the selectivity is low and varies strongly across the laser modified zone [Hna+06]. They suggest that thermal effects such as phase separation and migration of network modifiers prohibit the formation of nano gratings, an explanation which is reinforced by the modification microstructure that they observe in BK7.

However, preferential etching of laser modified zones in borosilicate glass has been demonstrated with KOH [Mat+09]. The intensity distribution within the material and the use of a burst mode can affect the etching behaviour and the resulting taper angle [Ort+22a; Ort+18b].

2.4 Energy deposition and its dependence on pulse duration

Transparency of the workpiece is a necessary condition for the high localization achieved in the laser process and also for enabling in volume structuring. A high transparency is equivalent to a low linear

absorption, meaning that at low light intensities no significant amount of energy will be deposited in the material as light passes through it. Many optical glasses are highly transparent for electromagnetic radiation in the visible spectrum and beyond, yielding a broad range of laser wavelengths that can be used, see Fig. 2.11. This high transparency is caused by the absence of any significant electromagnetic resonances within the glass lattice in this frequency range and by the tight bonding of the electrons, which means that at low intensities single photons do not have sufficient energy to remove electrons from their nuclei.

Transmittance at 250 – 2800 nm

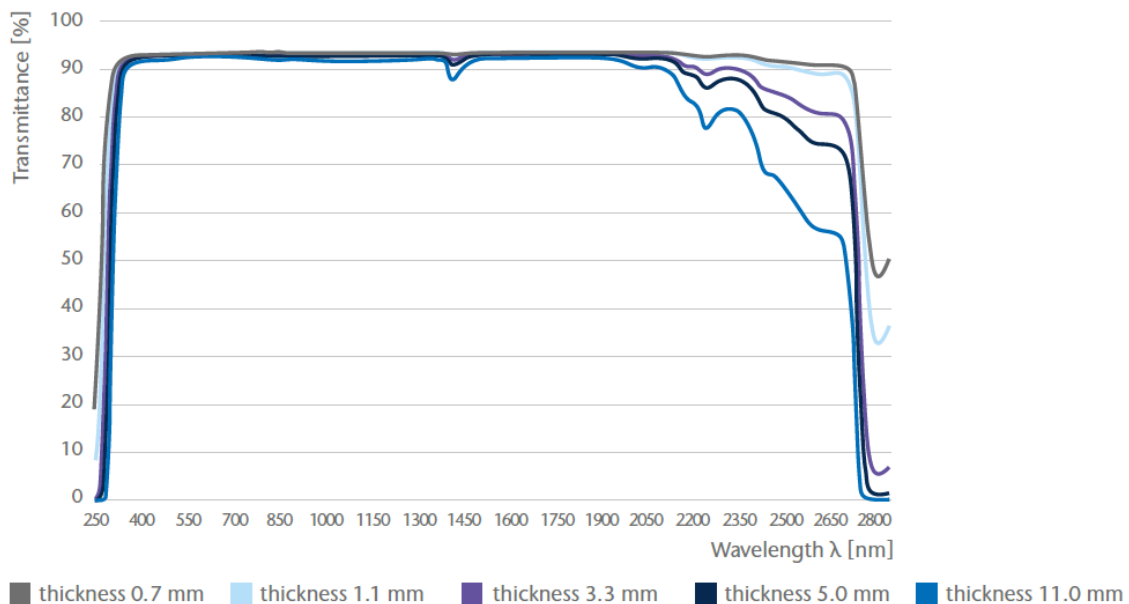


FIGURE 2.11: Transmittance of Borofloat[®] 33 [SCH22c].

At very high intensities⁹ however, the force exerted on the valence electrons within the glass by the laser electric field is sufficient to remove the electrons from their nuclei and thus create an electron cloud, a plasma. Within solids this process is described within the framework of band theory as promoting electrons from the valence band across the band gap to the conduction band. The resulting free electrons within the plasma act as an absorbing medium and eventually transfer energy from the laser pulse to the glass lattice. If a sufficient amount of energy is deposited within the material, permanent modifications of the material are created, as discussed above in Sec. 2.3.

The threshold character of the onset of non linear absorption that has been used for scaling the modification lengths, see Fig. 2.6, can also be seen in direct absorption measurements, see Fig. 2.12. The promotion of the electrons from the valence to the conduction band happens by direct photo ionization and avalanche ionization, i.e. the ionization by collision with free carriers (conduction band electrons) that have been heated by Inverse Bremsstrahlung, also see Fig. 2.13. The plasma dynamics, including the relaxation of the excited electrons, that leads to an energy transfer to the material lattice, are discussed in Sec. 2.4.1. The character and extent of the permanent modifications, however, does not only depend on the total amount of deposited energy but also the dissipation mechanisms of the material, the relative timing of the laser matter interaction and these dissipation mechanisms and the resulting distribution of energy density.

While laser absorption and energy transfer to the lattice happen on characteristic timescales smaller than few picoseconds, energy transport away from the interaction volume happens on longer timescales [SM02]. An overview of the most relevant time scales is shown in Fig. 2.14.

⁹typically in the range of TW/cm² for optical glasses

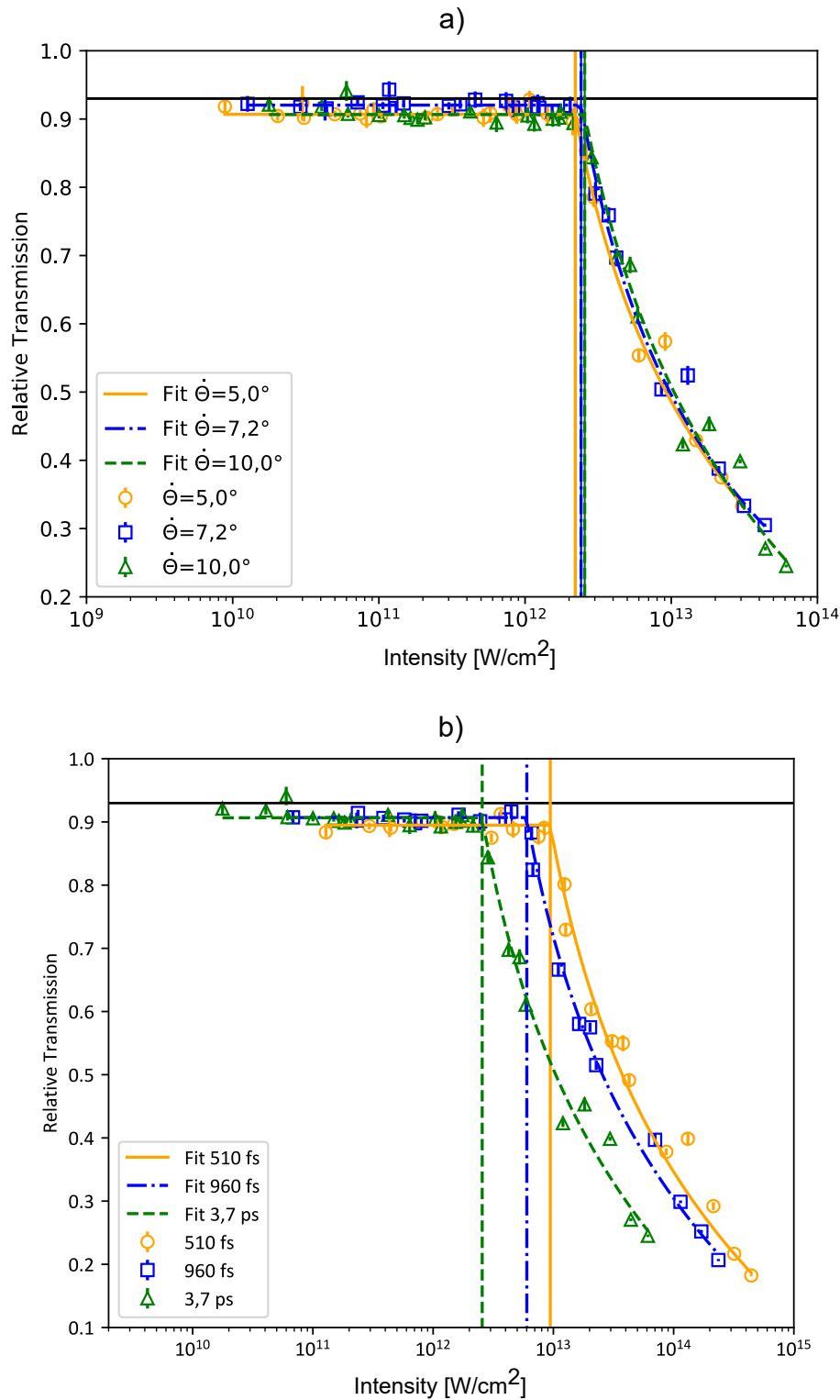


FIGURE 2.12: Transmission measurements for Bessel beams in borosilicate glass for varying Bessel cone angle at a constant pulse duration $\tau_p = 3.7$ ps (a) and for varying pulse duration at a constant cone angle $\alpha = 10^\circ$ (b) [Sch21]. Below a critical intensity threshold I_{th} the transmission remains just below the value expected for Fresnel reflection, above I_{th} the transmission rapidly drops, due to absorption by and defocussing at a plasma that is ignited by the laser pulse. The dependence of I_{th} on the pulse duration relates to the time dependence of the plasma dynamics.

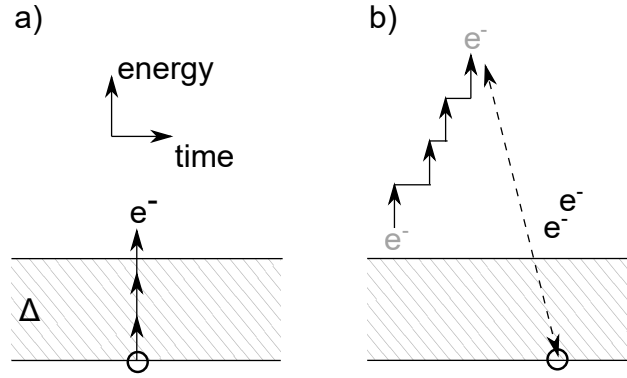


FIGURE 2.13: Schematic representation of multi photon (a) and avalanche ionization (b) for a material with band gap Δ . The arrows represent photons that are absorbed simultaneously (a) or successively (b).

The absorption by excitation of free electrons and the relaxation mechanisms, including the thermalization of the electrons and the energy transfer to the lattice during the relaxation of the plasma are discussed in more detail in Sec. 2.4.1. Here we will briefly review the thermal and structural events that are responsible for the dissipation of energy.

Pump and probe measurements of the interaction of Gaussian pulses with glass that resolve sub ps timescales show that pressure waves leave the interaction volume at a timescale of 500 ps at a velocity that slightly exceeds the sound velocity v_s in glass (5500 m/s) [Ber+18a]. Other means of energy transport such as the propagation of a melt front also move with a velocity close to v_s [Gam+07], which yields a distance of 3 μm at a timescale of 10 ps.

Another important dissipation mechanism is thermal diffusion. For a thermal conductivity λ_{th} , a density ρ , a specific heat capacity c_p and a resulting thermal diffusivity κ , the characteristic thermal diffusion length scale [BSL60]

$$l_{\text{th}}(t) = \sqrt{2\kappa t} \quad \text{where} \quad \kappa = \frac{\lambda_{\text{th}}}{\rho \cdot c_p} \quad (2.5)$$

during a pulse with a duration of 10 ps is 4 nm in borosilicate glass, see also Tab. 2.1 for the technical data of Borofloat[®] 33. This length is negligible compared to the diameter of the laser focal line which is in the order of magnitude of the laser wavelength. There is therefore no significant heating of the material that surrounds the interaction volume that is directly affected by the laser pulse on the timescale of the pulse duration. The presence of an "athermal" regime at ultrashort laser pulses is particularly relevant in brittle materials with a non-zero coefficient of thermal expansion, such as glass, a significant heating of parts of the work piece will induce stress. If the stress distribution is well controlled, it can be used for cutting, e.g. for laser induced thermal-crack propagation [ZZW14] or for thermal cleaving of a perforated surface [HH12], but it can also lead to unwanted material failure.

Because the time scales for absorption and thermalization are much shorter than relevant energy transport mechanisms, the optical propagation and energy deposition can be decoupled from the subsequent changes in the material for single laser pulses in the low ps regime. The energy density distribution after the laser pulse, that can be directly obtained as a result of numerical simulations of the non linear pulse propagation, can thus be used as a proxy for the material modification that is produced.

2.4.1 Plasma creation and relaxation

Taking into account the creation of the free electrons by direct photoionization, avalanche ionization and the recombination of electron-hole pairs, that leads to a relaxation of the plasma, the density of

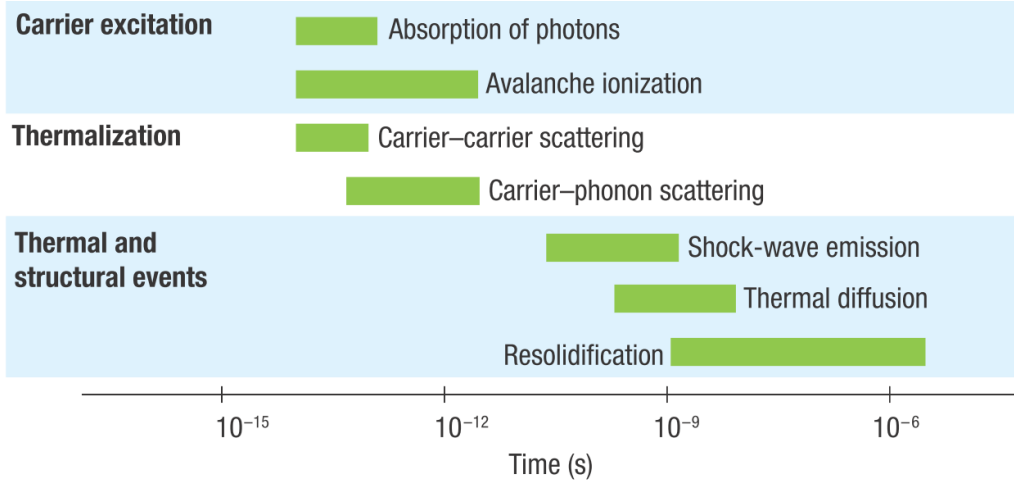


FIGURE 2.14: Relevant processes and their timescales for interaction of ultra short laser pulses and transparent dielectrics [GM08].

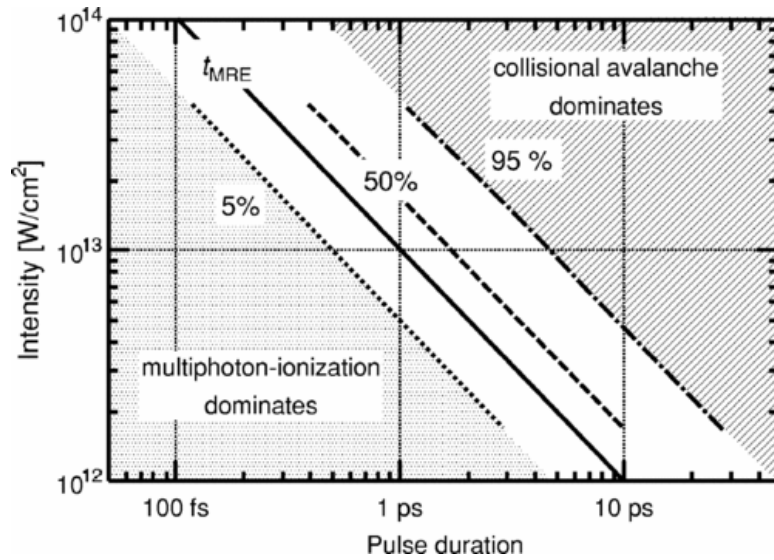


FIGURE 2.15: MPI vs. Avalanche proportion of impact ionized electrons for photon energy $\hbar\omega = 2.48$ eV in SiO₂ [Ret06]

free electrons in the conduction band $N_e(x, y, t, z)$ can be described as

$$\partial_t N_e = W_{PI} \frac{N_i - N_e}{N_i} + N_e \frac{\sigma I}{E_g} - \frac{N_e}{\tau_{rec}}, \quad (2.6)$$

where ∂_t denotes the partial derivative with respect to time. The photo ionization rate W_{PI} used here is derived from Keldysh [Kel65] and N_i represents the initial density of valence electrons. σ represents an effective cross section for electron collisions (also see Eq. 2.9), which leads to avalanche ionization, E_g is the band gap of the material, and τ_{rec} is a characteristic time scale for the recombination of electron-hole pairs. A spatial broadening of the N_e due to electronic heat diffusion has not been taken into account here.

The free electron density has been used to define damage thresholds [Stu+96]. This parameter is particularly suitable as proxy for damage onset and extent, because it directly gives the (minimum) amount of energy that is available to modify the material $\rho_{E,\min} = N_e E_g$. In many studies, the maximum electron density that is reached at some point during the pulse propagation was used. For

example a value of $1 \times 10^{20} \text{ cm}^{-3}$ for the maximum free electron density has been determined as ablation threshold for fused silica and has also been used for borosilicate glass [Sun+13a]. This choice of an instantaneous value is particularly suitable for long pulses, when both the energy transfer to the lattice and the lattice relaxation mechanisms, such as heat diffusion, take place during the duration of the pulse and a local balance between incoming energy and outgoing can be reached. It can also reasonably be used for very short pulses, for which there is no significant plasma relaxation during the pulse duration, so that the maximum energy density reached is a good measure for the total energy deposited in the material.

In this study we consider the time integrated losses of the laser pulse as proxy of material damage, i.e. the density of the energy accumulated during the full pulse propagation, because on the time scales considered here, the plasma relaxation can potentially play a role, but lattice relaxation mechanisms are much slower.

In the following we will consider the respective ionization and recombination rates that determine which terms dominates the plasma dynamics in the model.

Photo ionization: multi photon vs. tunnel ionization In 1965 Keldysh derived theoretically the ionization probability of atoms and solids when exposed to a strong electromagnetic wave [Kel65], considering tunnelling and the simultaneous absorption of multiple photons. He introduced the parameter $\gamma = \omega \sqrt{2m_r E_g} / (e\psi)$ with laser frequency ω , reduced electron mass m_r (electron-hole), bandgap E_g and peak electric field amplitude ψ [Kel65]. The equivalent expression in term of the intensity is $\gamma = \omega \sqrt{c\epsilon_0 n_0 m E_g / I} / e$ [Sun+13a]. For $\gamma \ll 1$ at high intensities the ponderomotive energy of electrons oscillating in the electric field is much larger than the band gap and tunnel ionization is likely. For the parameters in this work however, we only reach intensities of up to 5 TW/cm^2 within the volume, which gives $\gamma = 1.7$. This means that multi photon ionization can be considered as the dominant process and Kennedy's approximation can be used¹⁰ [Sun+13a; Ken95; Ber+08]. The photo ionization rate is then given by

$$W_{PI} = \sigma^{(K)} \times I^K, \quad (2.7)$$

with the number of absorbed photons $K = \langle E_g / \hbar\omega_0 + 1 \rangle$ and the photo ionization cross section

$$\sigma^{(K)} = \frac{2\omega_0}{9\pi} \left(\frac{m_r \omega_0}{\hbar} \right)^{\frac{3}{2}} \Phi_0 \left(\sqrt{2 \left(K - \frac{E_g}{\hbar\omega_0} \right)} \right) e^{2K} \left(\frac{e^2}{8m_r \omega_0^2 E_g \epsilon_0 c n_0} \right)^K, \quad (2.8)$$

where m_r and e are the reduced mass and charge of an electron respectively, \hbar is the reduced Planck's constant, ϵ_0 the permittivity of free space, c the speed of light and Φ_0 denotes the Dawson integral. Note that for small K , such as for borosilicate glass, the polarization of the laser beam does not have a large effect on the ionization rate, but for larger K the choice of polarization can have a significant influence [LAW11].

Determination of the optical band gap in borosilicate glass The band gap of borosilicate glass has been determined as 3.9 eV by an absorption spectrum fitting (ASF) method [SS09; Rao+18] in previous SCHOTT internal measurements [Sei+14]. The ASF method extends the Tauc model [TGV66] to transmission spectra that are readily available. An indirect allowed transition has been assumed for the Tauc model.

Avalanche ionization The cross section for electron-electron collisions

¹⁰The non linear simulations shown in this work however include the more complete model, which also accounts for the full photo ionization rate according to Keldysh [Kel65].

$$\sigma = \frac{k_0 e^2 \tau_c}{n_0^2 \omega_0 \epsilon_0 m_e (1 + \omega_0^2 \tau_c^2)}. \quad (2.9)$$

that is used to calculate the creation of free electrons by avalanche ionization in Eq. 2.6, is derived based on a Drude model, also see Sec. 2.4.4.

The effective electron collision time τ_c is a phenomenological parameter, which is rather loosely constrained, for a more detailed discussion see [Ret+17]. Multiple rate equations that take into account the different energy levels of electrons in the conduction band have been proposed previously [Ret04] but in this work we do not differentiate those, assuming a fast thermalization by electron-electron collisions in line with a two temperature model [Ret+17], and τ_c has been assumed to be constant.

The avalanche source term in Eq. 2.6 scales proportionally with the number of free electrons. This exponential contribution means that avalanche ionization typically comes in in the trailing part of the laser pulse, once a significant number of free electrons have been seeded by photo ionization, but also defects in the material can lead to a significant initial number of free electrons, that can act as seeds. In particular for long pulses avalanche ionization dominates, see also Fig. 2.15, and can lead to high plasma densities. This is of particular interest in terms of the stability of the laser process: Free electrons associated with material defects can act as seed electrons for avalanche ionization, leading to a strong dependence of the free electron density on the presence and density of material defects for long pulses [Stu+96]. The influence of the different ionization mechanisms can also be seen for different temporal pulse shapes [Eng+08].

Energy transfer to lattice and recombination The free electrons in the conduction band are in an excited state. Various mechanisms can lead to relaxation of this high energy state [Mau+16], for example the fast self trapping of excitons which is particularly observed in fused silica and happens on the time scale of 150 fs. The availability of such fast relaxation mechanisms determines, how much energy is available for slower relaxation mechanisms [Mau+16]. In particular, structural changes, such as plastic expansion and void creation, which are of paramount interest for material processing, happen on longer time scales. The transfer of energy from electrons to the lattice is possible as intra band process described in terms of electron phonon collision [Gam11] or can be modelled as three-body process, for example Auger recombination [Ret+17], the rates of which scale differently with N_e .

In practice however, pump-probe experiments that show the temporal evolution of the plasma are typically used to define a characteristic relaxation time τ_{rec} [Mau+16; Qua+06; AER18]. This can be understood as a term collecting all relaxation mechanisms in a simple exponential behaviour that is empirically determined. Here, we use the value $\tau_{rec} = 150$ fs that was previously used for soda lime glass [Mis+17], although also longer relaxation times have been reported and used for borosilicate glass [Mau+16; DC+15]. In pump-probe experiments even values of up to 113 ps have been reported as relaxation time scale in K9 (borosilicate crown) glass [Qua+06].

2.4.2 Modeling of non linear pulse propagation

If only the plasma generation is considered, as in the section above, it seems that an increase in intensity, for example by lowering the pulse duration and keeping the pulse energy constant, should lead to an improved energy deposition. In fact however, this can lead to a suppression of material modifications as shown in Fig. 2.16. These observations can be understood in terms of the propagation of the laser pulse in the presence of non linear effects in the material. Those include the optical Kerr effect, which leads to a change of the refractive index and in particular the interaction of the laser light with the plasma.

The non linear propagation simulations presented in this study use a pre-existing unidirectional pulse propagation model [Ber+08; DC+15] to calculate the energy density distribution within the

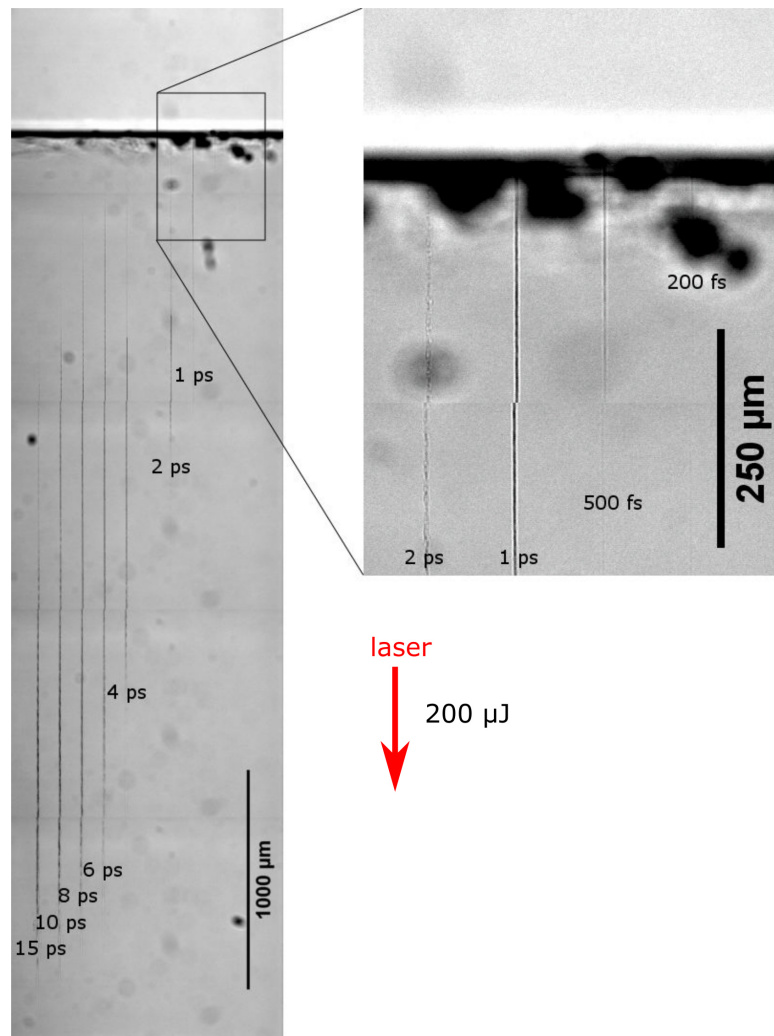


FIGURE 2.16: Permanent glass modifications in borosilicate glass after produced with a spherically aberrated lens for varying pulse duration at a constant pulse energy $E_p = 200 \mu\text{J}$ [Sch17].

glass which is equivalent to the spatially resolved loss of energy of the laser pulse along its propagation through the glass. Low back scattering and paraxial focusing conditions are the crucial assumptions for reducing the full vectorial description of the electric field according to the Maxwell equations to this model [MJ04; Ber+08]. The change of the slowly varying complex field envelope $E(x, y, \bar{t}, z)$ along the propagation direction z

$$\partial_z E = i \left(\frac{1}{2k_0} (\partial_x^2 + \partial_y^2) E - \frac{k''}{2} \partial_{\bar{t}}^2 E + \frac{2\pi n_2}{\lambda} I E - \frac{k_0}{2n_0^2 N_c} N_e E \right) - \frac{E_g W_{PI} (N_i - N_e)}{2N_i I} E - \frac{\sigma}{2} N_e E \quad (2.10)$$

is then, going from left to right on the right hand side, determined by non absorptive terms that describe

- the diffraction of the light for a laser pulse with a wave number $k_0 = 2\pi n_0 / \lambda$ in a medium with a linear refractive index n_0 at the centre optical wavelength of the driving pulse in vacuum λ ,
- the temporal evolution of the laser pulse, where the retarded time $\bar{t} = t - z/v_g$ is defined in a frame moving with the pulse at a group velocity v_g and k'' represents the second order group velocity dispersion in the material,

the changes of the refractive index due to

- the Kerr non linearity with a non linear refractive index n_2 of the material and a laser intensity $I = |E|^2$
- and the plasma, where N_c is the critical electron density in the conduction band, see Eq. 2.16 and Sec. 2.4.4 for more details,

as well as absorptive terms that account for the creation of new free electrons and that directly correspond to the source terms in the evolution of the electron density, see Eq. 2.6, so that overall energy is conserved and the energy density in the material is given by the spatially resolved energy loss of the laser pulse.

2.4.3 Self focusing

At high electric field strengths, the electromagnetic wave can change the refractive index of the material that it passes through, which can be understood in terms of third order contributions to the polarization p that is induced by the electromagnetic wave as the approximation of harmonic charge potentials in the material no longer holds, see [Boy08] for a detailed derivation. The refractive index can then be expressed as $n = n_0 + n_2 I$, where n_0 describes the linear refractive index, n_2 the non linear refractive index. This change in refractive index results in a self-phase modulation of the laser pulse and is also known as the optical Kerr effect. The value of the non linear refractive index has previously been derived theoretically as $n_2 = 3\chi^{(3)} / (2n_0^2 \epsilon_0 c) \simeq \mathcal{O}(1.0 \times 10^{-21} \text{ m}^2/\text{W})$, using an order-of-magnitude estimate for the third order susceptibility in condensed matter $\chi^{(3)} \simeq \mathcal{O}(\chi^{(1)} / E_{at}^2) = 4 \times 10^{-24} \text{ m}^2/\text{V}^2$ where E_{at} is the atomic field strength [Boy08].

The more material specific, empirically derived expression [BGO78]

$$n_2 = \frac{68(n_d - 1)(n_d^2 + 2)^2}{v_d \sqrt{1.517 + \frac{(n_d^2 + 2)(n_d + 1)}{6n_d}} v_d} \times \frac{8.38 \times 10^{-7}}{n_d} \quad (2.11)$$

provides an estimate of n_2 based on the Abbe number¹¹ $v_d = (n_d - 1) / (n_{F'} - n_{C'})$ and the refractive indices n_d , $n_{F'}$ and $n_{C'}$, which are defined at Fraunhofer absorption lines at optical wavelengths

¹¹While the Abbe number is generally defined as a linear approximation of the chromatic dispersion $dn/d\lambda$ in the optical spectrum, the wavelengths that are used for its calculation vary slightly in literature, e.g. compare v_e in [SCH22c] and v_d in [BGO78], referring to different Fraunhofer absorption lines used as centre wavelength.

587.6 nm, 480.0 nm and 643.8 nm respectively. The last factor in Eq. 2.11 is added to convert from esu to SI units. This expression for n_2 has also been confirmed experimentally by [ACP87]. For our borosilicate glass this yields a values of $5 \times 10^{-20} \text{ m}^2/\text{W}$. While this value is defined in the mid-optical range, we assume that the dispersion in n_2 can be neglected and this value can be used as a reasonable estimate in the near infrared.

In general, n_2 is positive, thus creating a focusing effect for convex beam shapes, similar to a collecting gradient index (GRIN) lens. This self focusing effect will occur for powers above a critical value

$$P_{\text{cr}} = \frac{\alpha \lambda^2}{8\pi n_2 n_0} \quad (2.12)$$

independent of beam diameter, if the propagation distance is sufficiently long. The constant α depends on the beam shape. A lower limit for the critical power for any beam shape is given by $\alpha = 3.72$, which is calculated for the Townes mode, a radially-symmetric soliton that can lead to theoretically unlimited self-focusing [CGT64; Sku05; Ber+08]. For tightly focused beams, the non linear phase contribution may be small compared to the phase curvature caused by the focusing optics even for pulse powers above P_{cr} . For a rough quantitative comparison, the Kerr effect can be expected to be negligible, if the self focusing distance z_f for a collimated input beam with Rayleigh length z_0 given by the Marburger formula [Kar+18]

$$z_f = \frac{0.367z_0}{\sqrt{\left(\sqrt{P_{\text{peak}}/P_{\text{cr}}} - 0.852\right)^2 - 0.0219}} \quad (2.13)$$

is much larger than the focal length of the focusing optics.

2.4.4 Distributed shielding and intensity clamping

The interaction of a free electron cloud with the oscillating electromagnetic field can be described by a Drude model [Ret+17]. The interaction leads to a modified dielectric function of the material

$$\epsilon_m = \epsilon_r - \left(\frac{\omega_p}{\omega_0}\right)^2 \frac{1}{1 + i/(\omega_0 \tau_c)} \quad (2.14)$$

for a relative dielectric constant $\epsilon_r = n_0^2$ of the pristine, unperturbed material and a plasma frequency [Ret+17]

$$\omega_p = \sqrt{N_e e^2 / (m_e \epsilon_0)}. \quad (2.15)$$

At a critical electron density

$$N_c = \epsilon_0 \epsilon_r \frac{m_e \omega_0^2}{e^2} \quad (2.16)$$

the real part vanishes. The real part of the refractive index $n_m = \sqrt{\epsilon_m}$ thus also drops to zero, the plasma behaves like a metal and light can not propagate further into the plasma. The simulated electron densities in this work remain far below N_c , but even at those plasma densities, the reduction of the refractive index, which can then be approximated as

$$\Delta n_m \approx -\frac{N_e}{N_c}, \quad (2.17)$$

leads to defocusing of the laser beam for convex plasma distributions as for example for a Gaussian beam.

Generally, absorption and defocusing due to the plasma both decrease the intensity of the laser beam further along the propagation. This effect is called distributed shielding effect, see [Ber+18a].

For a given material and laser wavelength and pulse duration this results in a maximum intensity that can not be increased by increasing the laser pulse energy. This effect has first been reported for collimated fs pulses in gases [Bec+01] and is called intensity clamping. It also has been demonstrated for fs pulses in solids [Liu+02] and ps pulses in gases [SS+16]. The increase in energy instead leads to a transverse broadening of the laser irradiated region and thus to a broad plasma that can absorb large portions of the laser pulse energy without reaching higher energy densities.

For suitable focusing conditions, repeated cycles of self-focusing and plasma defocusing can lead to an extended region of repeated plasma ignition along the laser propagation [CM07], a process called (non linear) filamentation.

2.4.5 Damage thresholds at surface and in volume

For a micro perforation process that modifies the work piece in its entire thickness up to the surfaces, both damage thresholds at surface and volume need to be considered, as plasma ignition at the surface can impact the propagation of the laser pulse.

Apart from the difference in damage morphologies that arise from the different mechanical confinement at the surface and in volume, also a difference in ionization mechanisms and rates has to be considered. Even with careful handling the surface will naturally accumulate some mechanical damage and absorbing dirt can additionally lower the threshold for surface damage [Stu+96]. Specifically, they can provide an increased initial free electron density, acting as seeds for avalanche ionization. Being randomly distributed, both dirt and defects will lead to a less deterministic process as the pulse duration is increased and their contribution to the ionization rate becomes more important. Indeed this effect has been found in previous ablation experiments [Stu+96; San+10]. Even in experiments on ion beam polished samples a surface damage threshold has been determined that is lower than the volume threshold by a factor of 4-5 [Giu72]. This may be attributed to the breakdown of the band model, that works in volume and thus a collapse of the band gap which leads to easier ionization. However, according to Bloembergen [Blo73], this effect is negligible. He states that even for the polished samples the local field enhancement due to surface defects such as dents and microcracks is sufficient to explain the observed differences in the respective damage thresholds.

2.4.6 Cumulative effects and burst mode

The distributed shielding caused by the plasma can be reduced if the laser power is distributed among several pulses. If they are repeated at timescales that are shorter than the characteristic heat diffusion time, heat accumulates within the processing volume and leads to temperature increases of up to several thousand Kelvin [Mis+17; Sun+13b].

For the creation of continuous larger features (several μm to tens of μm) such as waveguides [Eat+05; Eat+08] or micro welds [MCS11] the laser is typically continuously firing at kHz to low MHz repetition rates. For applications such as glass cutting [Mis+17], that rely on the localized mechanical damage that is created by an explosive material reaction, burst mode operation with several tens of MHz repetitions rates are used, which are limited by the laser oscillator frequency. A typical pattern for the burst consists of pulses with decreasing energy, due to the depletion of the amplifier, e.g. [Ber+18b]. Here, we use a burst mode, that evenly distributes the energy between the pulse in the burst, also see Fig. 2.17.

Simulations for laser welding applications indicate that thermal ionization can play a significant role by providing seed electrons for avalanche ionization for microprocessing with pulse trains [MCS11; Sun+13b]. For example at 3600°C , the simulated free electron density due to thermal ionization is around $5 \times 10^{18} \text{ cm}^{-3}$ [Sun+13b]. This effect is even more pronounced at longer wavelength, when more photons are required for photo ionization [IKM18].

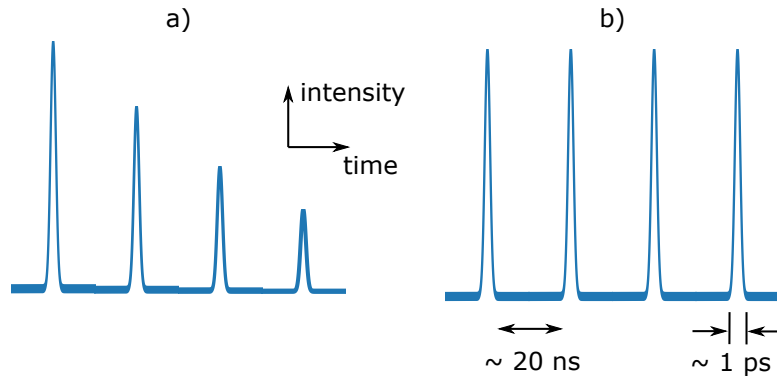


FIGURE 2.17: Schematic representation of the burst mode for decreasing (a) and constant (b) pulse energy respectively with typical timescales for the intra-burst pulse period and the pulse duration.

Another pathway for cumulative damage effects, that remains available over time scales much longer than the thermal diffusion time, could be provided by permanent modifications which lead to an elevated energy state of the irradiated area compared to pristine material. The type of modification depends on the relaxation pathways available in the material, see Sec. 2.4.1. In terms of numerical modelling the elevated energy state could be represented as reduced band gap or an increased initial free electron density.

In many simulations however, this seed mechanism is neglected and the more efficient energy deposition can be solely attributed to the reduction of the distributed plasma shielding when the energy is split between multiple pulses within a burst [Mis+17]. This reduction of the shielding relies on the fact that the relaxation time of the plasma is much shorter, than the typical time between subsequent pulses in the burst (typical value: 20 ns).

Regarding the mechanical damage, the repeated loading by pressure waves of several laser shots at the same location, e.g. for a laser used in burst configuration, can also cause cracks to grow in length [Hen+16], see Fig. 2.8. Hendricks et al. explain the crack growth by tensile stresses induced by the shear wave that radiates outward from the absorption volume, referring to earlier pump and probe observations in LiF crystals, where the crack tip propagation speed equals secondary (i.e. shear) wave velocity[Sak+11].

2.5 Summary

The micro perforation process provides a fast, clean and precise method for defining weakened surfaces in transparent dielectrics which can be used for glass sheet cutting in combination with a subsequent separation step, either mechanical cleaving or wet etching. In borosilicate glass, both separation mechanisms rely on the presence of mechanical damage.

Particularly low laser process times can be achieved when the glass sheet is modified throughout its full thickness with a single laser shot. In transversal direction, on the other hand, a high confinement is required for precise micro machining results, i.e. modifications are required to have high aspect ratios. For quasi non diffracting and similar beams the length of the focal intensity distribution can be scaled independently from the lateral width. The maximum length of glass modifications that can be reached depends on the available pulse energy and the size of the optics. Beam shapes used for micro perforation so far have been limited to straight line geometries.

The separation process requires joining of neighbouring modifications. Mechanical cleaving in particular can be improved by aligning cracks that are produced by the laser process along the intended cutting direction.

In-volume modifications within transparent materials and a high localization of the modifications are possible due the ignition of a plasma, which is a process that scales non linearly with the intensity, leading to a strong increase of absorption above a critical intensity threshold. For pulse durations in the low ps regime and below, the energy deposition takes place on time scales that are shorter than the material response. Therefore variations of permanent glass modification with the pulse duration can be attributed to changes of the energy density that is reached within the material after the laser pulse. Distributed shielding due to defocusing and absorption by the plasma limits the achievable energy densities.

Burst mode operation of the laser enhances the energy deposition and increases the length of cracks.

Chapter 3

Linear propagation of the Airy Gauss beam and its experimental realisation

The Airy beam is a non diffracting beam featuring a curved line focus, that is to say its main lobe appears to be accelerated in the transverse plane during propagation. After the theoretical description of non dispersing Airy wave packets in 1979 [BB79], the optical, finite-energy Airy-Gauss beam was first described theoretically and demonstrated experimentally in 2007 [SC07; Siv+07]. While the applications that followed reach from 1D light sheets [Yan+14] to light bullets formed by a ring-Airy [Pan+13; Zha+18], the most commonly treated case is still the 2D case given by the linear combination of cubic phases along two perpendicular axes in the far field [Mat+12; Fro+11; Pol+09]. As the first of a whole group of accelerating beams [Efr+19], the 2D Airy beam has been used before to create long, curved plasma channels (ca. 1 m length) in air [Pol+09]. Two ablation based micro machining concepts have been demonstrated with the 2D Airy beam: The shaping of existing edges of thin sheets of silicon and diamond [Mat+12] by laterally moving the beam closer to the edge in an iterative process and the creation of curved trenches in silicon by repeated vertical illumination onto a flat surface [Mat+12; Mat+13b].

This chapter deals with the derivation of the linear, paraxial description of the Airy beam, starting with the 1D case and then moving to the 2D case before discussing the scaling of the crucial properties of the beam, principally curvature, length and focal contrast of the beam. Different ways to produce the Airy beam are introduced, along with the physical realisation of the phase mask that is used to produce the Airy beam. This chapter also provides the theoretical background for fast numerical tools, that can be used to calculate arbitrary fields. This tool can be checked against the analytical results and used for those cases in which the propagation is not readily described by analytical expressions, see for example 3.7.1.

3.1 Paraxial Helmholtz equation

Even if any volume structuring process inherently involves non linear effects it is useful and instructive to first consider the linear propagation of the Airy beam. Firstly, at the intensities reached in the experiments in this work, the propagation to the work piece in air is adequately described by free space propagation. The field at the surface of the glass sheet can thus be directly calculated and be used as input field for the non linear simulations. Secondly, because of the localization of the non linear absorption and the self healing properties of the Airy beam [Bro+08] we can expect that the linear scaling of the beam is a good approximation to the observed modifications. This is indeed what we observe, see Sec. 4.2.

In this section we will recapitulate the derivation of the paraxial Helmholtz equation [ST01; Goo17] and point out the assumptions and approximations that it is based upon.

In the absence of free charge, which we can assume for propagation in air and in dielectrics at sufficiently low intensities, the evolution of electromagnetic fields is described by the Maxwell equations

$$\begin{aligned}
\nabla \times \mathbf{E} &= -\mu_0 \frac{\partial \mathbf{H}}{\partial t} \\
\nabla \times \mathbf{H} &= \epsilon \frac{\partial \mathbf{E}}{\partial t} \\
\nabla \cdot \mathbf{E} &= 0 \\
\nabla \cdot \mathbf{H} &= 0
\end{aligned} \tag{3.1}$$

using the conventional vector notation of the electric field \mathbf{E} , the magnetic field \mathbf{H} and the divergence $\nabla \cdot$ and curl $\nabla \times$. As we are dealing with non-magnetic materials, we use the permeability of free space μ_0 and the permittivity in the dielectric material $\epsilon = \epsilon_r \epsilon_0$ is given by the relative permittivity and permittivity of free space.

By applying the vector identity $\nabla \times (\nabla \times \mathbf{A}) = \nabla^2 \mathbf{A} - \nabla (\nabla \cdot \mathbf{A})$, where ∇^2 denotes the Laplacian operator, to the electric field and inserting from Eq. 3.1 we obtain $\nabla^2 \mathbf{E} = \nabla \times (-\mu_0 \partial \mathbf{H} / \partial t)$. For linear conditions without temporal-spatial coupling and for a constant permittivity this can further be simplified, by swapping the order of operators and again inserting from Eq. 3.1 to

$$\nabla^2 \mathbf{E} - \mu_0 \epsilon \frac{\partial^2 \mathbf{E}}{\partial t^2} = 0. \tag{3.2}$$

In the micro machining experiments in this work the light is linearly polarized, the angles of incidence at phase boundaries, e.g. the air-glass interface, are moderate and lateral variations of the permittivity can be neglected. The wave equation 3.2 can thus further be simplified to obtain the scalar wave equation

$$\nabla^2 e - \frac{n^2}{c^2} \frac{\partial^2 e}{\partial t^2} = 0. \tag{3.3}$$

with the speed of light in vacuum $c = 1/\sqrt{\mu_0 \epsilon_0}$ and the refractive index $n = \sqrt{\epsilon_r}$ of the dielectric medium, which in dispersive media depends on the frequency ν . As we are for now interested in the spatial propagation properties, we can drop the the time dependence in the scalar electric field $e(x, y, z, t) = A(x, y, z) \exp(-i\omega t)$ for a monochromatic wave with angular frequency $\omega = 2\pi\nu$ and use the Helmholtz equation

$$(\nabla^2 + k^2)A = 0. \tag{3.4}$$

in terms of the complex amplitude $A(x, y, z)$ and the wave number $k = 2\pi/\lambda$, which directly relates to the optical wavelength $\lambda = c/(n\nu)$.

If the complex amplitude of a wave travelling in the positive z direction can be adequately described in terms of an envelope function $E(\mathbf{r})$ that varies only slowly along the propagation as

$$A(\mathbf{r}) = E(\mathbf{r})e^{ikz} \tag{3.5}$$

and the change of the derivative of $E(\mathbf{r})$

$$\left| \frac{\partial^2 E}{\partial z^2} \right| \ll \left| k \frac{\partial E}{\partial z} \right| \tag{3.6}$$

so that it can be neglected, one arrives at the paraxial Helmholtz equation

$$(\nabla_T^2 + i2k \frac{\partial}{\partial z})E = 0, \tag{3.7}$$

which has the same form as the potential free Schroedinger equation.

3.1.1 Gaussian beam

An important solution of the paraxial Helmholtz equation is the Gaussian beam. Expressed in cylindrical coordinates with $\rho = \sqrt{x^2 + y^2}$, the slowly varying envelope

$$E(\rho, z) = A_0 \frac{W_0}{W(z)} \exp \left[-\frac{\rho^2}{W^2(z)} + i \left(k \frac{\rho^2}{2R(z)} - \zeta(z) \right) \right] \quad (3.8)$$

of a Gaussian beam with its waist at $z = 0$ is fully characterized by its amplitude A_0 and its Rayleigh length z_0 or alternatively its waist radius $W_0 = \sqrt{\lambda z_0 / \pi}$ [ST01]. The propagation dependence of the beam radius $W(z) = W_0 \sqrt{1 + (z/z_0)^2}$, the wavefront radius $R(z) = z (1 + (z_0/z)^2)$ and the Guoy phase $\zeta(z) = \tan^{-1}(z/z_0)$ can be dropped if the propagation distances are much smaller than z_0 . For the input beams that we use in our optical system, this is usually the case. Also, the beams are well collimated, i.e. we are close to the waist of the beam and the phase is flat, so that the input beam can be characterized by a simplified version of Eq. 3.8 as

$$A(\rho) = A_0 \exp \left[-\frac{\rho^2}{w_0^2} \right]. \quad (3.9)$$

The amplitude A_0 is determined by the normalization condition that the integral of the intensity $I = |A|^2$ over the transversal plane equals the laser power

$$P = \int_0^{2\pi} \int_0^\infty \rho I d\rho d\phi = A_0^2 \frac{\pi}{2} w_0^2, \quad (3.10)$$

so that

$$A_0 = \sqrt{\frac{2P}{\pi w_0^2}}. \quad (3.11)$$

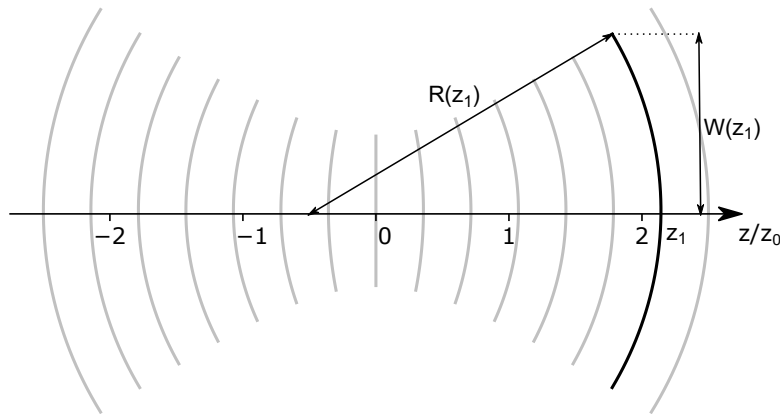


FIGURE 3.1: Evolution of the wavefronts of a Gaussian beam with Rayleigh length z_0 and wavelength $\lambda = z_0$ nears its waist.

Focussing by multiple lenses Within the paraxial approximation for which the Gaussian beam description holds, the effect of a thin lens with focal length f can be described as an extra phase

$$\phi_{tl} = \frac{-k\rho^2}{2f} \quad (3.12)$$

which is the quadratic approximation for a spherical wave front. For multiple lenses with focal lengths f_1 and f_2 respectively an effective focal length

$$\frac{1}{f_{\text{eff}}} = \frac{1}{f_1} + \frac{1}{f_2} \quad (3.13)$$

can be defined just as in ray optics when the change in wavefront radius $R(z)$, see Fig. 3.1 during the propagation between them can be neglected. If $f_1 \gg f_2$, Eq. 3.13 reduces to

$$f_{\text{eff}} = f_2 - \frac{f_2^2}{f_1}. \quad (3.14)$$

A more complete description within Gaussian optics for the optical system can be obtained using a matrix formalism that holds for any paraxial system [ST01]. The complex beam parameter $q = z + iz_0$ fully defines the propagation behaviour of a Gaussian beam. The real part of the beam parameter

$$q_2 = \frac{Aq_1 + B}{Cq_1 + D} \quad \text{with} \quad \begin{bmatrix} A & B \\ C & D \end{bmatrix} = \begin{bmatrix} 1 + \frac{d}{f_1} & d \\ \frac{d+f_1+f}{f_1 f_2} & 1 + \frac{d}{f_2} \end{bmatrix} \quad (3.15)$$

for a beam at the output plane of an optical system of two lenses as above, separated by a distance d , directly gives the distance to the beam waist behind the second lens. The beam parameter for the collimated input beam is given by $q_1 = iz_0 = i\pi w_0^2/\lambda$.

For more general beam shaping, however, we also need to consider the propagation of a beam with an arbitrary optical field in a paraxial optical system. Fourier optics provide the appropriate theoretical description for this case.

3.2 Fourier optics - spatial spectrum of the optical field

An arbitrary normalizable complex valued function $g(x, y)$ defined with respect to the spatial coordinates x and y can be equivalently written as $G(\nu_x, \nu_y)$ in terms of its spatial frequencies ν_x and ν_y . They can be converted into each other by the Fourier transform

$$\mathcal{F}(g) = \iint_{-\infty}^{+\infty} g(x, y) \exp[-i2\pi(\nu_x x + \nu_y y)] dx dy \quad (3.16)$$

and the inverse Fourier transform

$$\mathcal{F}^{-1}(G) = \iint_{-\infty}^{+\infty} G(\nu_x, \nu_y) \exp[i2\pi(\nu_x x + \nu_y y)] d\nu_x d\nu_y \quad (3.17)$$

respectively. If the function $g(x, y)$ is separable in the Cartesian coordinates x and y , i.e. can be written as product of two functions that only depend on one variable respectively, so that $g(x, y) = g_x(x)g_y(y)$, the Fourier transform of $g(x, y)$ is given by the product of two one dimensional Fourier transforms as

$$\mathcal{F}(g(x, y)) = \mathcal{F}_x(g_x(x)) \mathcal{F}_y(g_y(y)) \quad (3.18)$$

The same holds for the inverse Fourier transform.

Applied to propagating optical fields [Goo17], a pair of spatial frequencies ν_x and ν_y in the input plane can be interpreted as a plane wave $E(x, y, z) = A \exp[i(k_x x + k_y y + k_z z)]$ travelling in the

direction of its wave vector $\mathbf{k} = (k_x, k_y, k_z)$, the lateral components $k_x = 2\pi\nu_x$ and $k_y = 2\pi\nu_y$ of which directly relate to the spatial frequencies of the field in the input plane and their combined length in the transversal plane $k_T = \sqrt{k_x^2 + k_y^2}$ is also referred to as the transversal wave number. The longitudinal wave number

$$k_z = \sqrt{k^2 - k_T^2} = \sqrt{k^2 - k_x^2 - k_y^2} \quad (3.19)$$

can be straightforwardly computed due to the condition that the length of the wave vector must correspond to the wave number k to satisfy the Helmholtz equation, given in Eq. 3.4. Plane wave components with $k_T > k$ will not propagate far behind the input plane but rapidly (on the order of few wavelengths) decay in amplitude along z . For the beam shaping considered in this work these evanescent waves can be neglected.

3.2.1 Fourier transform by a single lens

Collecting lenses in paraxial focusing conditions can be used to optically perform the Fourier transform of an input beam. This relationship holds exactly for two conjugated transversal planes which are on either side of the lens at a distance that equals the focal length f of the lens. As both input beam and its spectrum are represented in physical space in this case, these planes are called direct and Fourier plane respectively. Repeated cycling between direct and Fourier space is possible with multiple lenses. This will be discussed in Sec. 3.2.2 in more detail. Here we will briefly recapitulate the derivation of this important property for a single lens, which is considered in more detail in [Goo17].

The paraxial phase contribution of a thin lens, as given in Eq. 3.12, but this time in Cartesian coordinates, to an input field just in front of the lens $E_l(x, y)$ yields a field

$$E_l'(x, y) = E_l(x, y) \exp \left[-i \frac{k}{2f} (x^2 + y^2) \right] \quad (3.20)$$

right behind the lens.

Using the Fresnel diffraction formula¹ to calculate the field $E_f(u, v)$ at the back focal plane of the lens at $z = f$ for spatial coordinates u and v

$$E_f(u, v) = \frac{\exp \left[i \frac{k}{2f} (u^2 + v^2) \right]}{i\lambda f} \times \iint_{-\infty}^{+\infty} E_l'(x, y) \exp \left[i \frac{k}{2f} (x^2 + y^2) \right] \exp \left[-i \frac{k}{f} (xu + yv) \right] dx dy \quad (3.21)$$

leads to exact cancellation of the quadratic phase contribution of the lens, so that

$$\begin{aligned} E_f(u, v) &= \frac{\exp \left[i \frac{k}{2f} (u^2 + v^2) \right]}{i\lambda f} \iint_{-\infty}^{+\infty} E_l(x, y) \exp \left[-i \frac{2\pi}{\lambda f} (xu + yv) \right] dx dy \\ &= \frac{\exp \left[i \frac{k}{2f} (u^2 + v^2) \right]}{i\lambda f} S_l \left(\frac{u}{\lambda f}, \frac{v}{\lambda f} \right), \end{aligned} \quad (3.22)$$

where $S_l(u/(\lambda f), v/(\lambda f)) = \mathcal{F}(E_l(x, y))$ is the Fourier spectrum of the field in front of the lens. This field can also be calculated by using the paraxial transfer function from Eq. 3.28 with spatial angular

¹This can be found in many textbooks, for example also in [Goo17].

frequencies $k_x = uk/f$ and $k_y = vk/f$ for the Fourier spectrum $S_0(k_x, k_y)$ of the input field $E_0(x, y)$ at a distance d in front of the lens, see also Fig. 3.2 as

$$S_l(k_x, k_y) = S_0(k_x, k_y) \exp \left[\frac{-i\lambda d}{2} (k_x^2 + k_y^2) \right]. \quad (3.23)$$

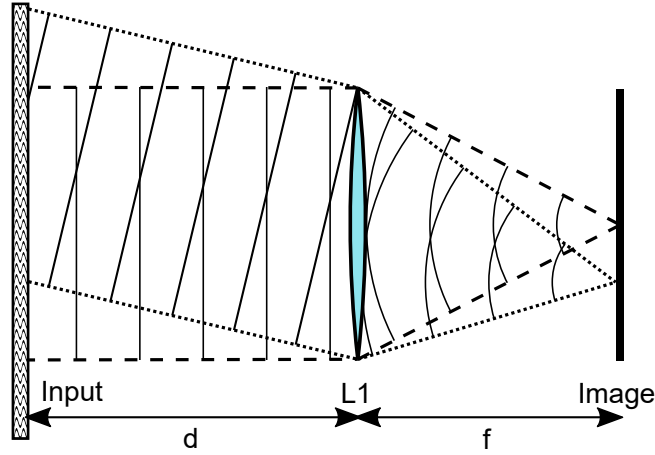


FIGURE 3.2: Schematic representation of focusing of plane waves by a single collecting lens L1. The different spatial frequencies are mapped to different locations in the image plane. For $d = f$ this corresponds to the often cited $2f$ setup.

Substituting Eq. 3.23 into Eq. 3.22 then yields

$$E_f(u, v) = \frac{\exp \left[i \frac{k}{2f} \left(1 - \frac{d}{f} \right) (u^2 + v^2) \right]}{i\lambda f} S_0(k_x, k_y). \quad (3.24)$$

For $d = f$ the quadratic phase term cancels and the input and image plane are related by an exact Fourier integral. The intensity at the image plane

$$I_f(u, v) = |E_f|^2 = \frac{1}{\lambda^2 f^2} |S_0(k_x, k_y)|^2 \quad (3.25)$$

is independent of the distance between input plane and lens, but the additional phase terms for $d \neq f$ will affect the further propagation of the beam, leading to an effective change in focal length, which can be relevant when line focus geometries are considered instead of a single image plane.

3.2.2 4f and 6f setup

The focal intensity obtained behind a single lens can in some cases be used directly for material processing, as for example for the Airy beam, see Sec. 3.4. However, some beam shaping elements, in particular LCOS-Spatial light modulators (Liquid Crystal on Silicon, see Sec. 3.6.1 for more details), produce unwanted diffraction orders, that carry significant portions of the beam power. By placing a diaphragm at the Fourier plane behind a first lens L_1 with long focal length f_1 , the unwanted diffraction orders can be removed, see Fig. 3.3. This is also referred to as spatial filtering or Fourier filtering, for example see [Mat+13a].

In many cases, the 0th order, i.e. the unshaped light², carries the most energy after the 1st diffraction order with the intended beam shape. In those cases, a sufficient angular separation of the 0th

²Often it is also referred to as undiffracted light, because it forms at the angle of transmission or reflection, independent of the spatial frequencies in the grating. Because of this independence it does not carry the information of the grating structure, unlike all other diffraction orders.

and 1st order need to be ensured, e.g. by adding a blazed grating to the phase mask. Alternatively an aperture that is adapted more specifically to the beam shape can be used as spatial filter.

A second lens L_2 , placed at a distance of f_2 behind the Fourier plane, converts the beam back to direct space, i.e. L_1 and L_2 form a telescope. This combination of collecting lenses is also called 4f setup. The choice of the focal lengths determines the magnification

$$M = \frac{f_2}{f_1}. \quad (3.26)$$

An appropriate demagnification (i.e. $f_2 < f_1$) can be particularly useful if a broad beam coming from a relatively large phase mask that is fully illuminated needs to be fitted into the smaller aperture of a microscope objective, L_3 , which in turn forms another telescope with L_2 . The full resulting 6f setup, as shown in Fig. 3.3, is used for Fourier space imaging, while the 4f setup, an example of which is shown in Fig. 2.3, is used for direct space imaging - according to whether the Fourier transform or a demagnified image of the beam at the input plane is used for material processing.

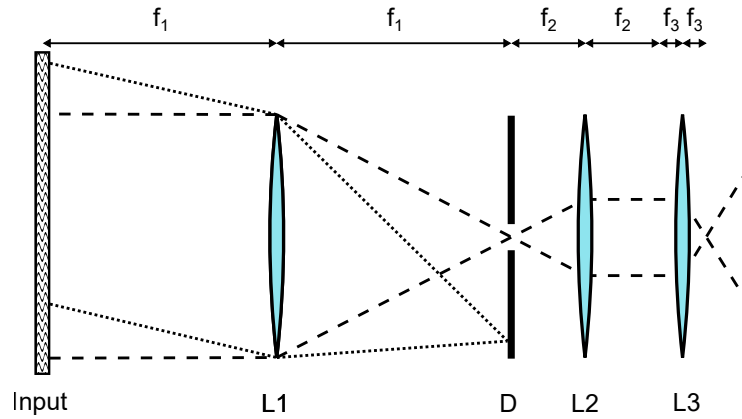


FIGURE 3.3: Schematic representation of a 6f setup, which can be interpreted as the combination of a 2f setup and a telescope formed by two collecting lenses (L_2, L_3). If a diaphragm D is placed at the image plane of L_1 , unwanted spatial frequencies, e.g. unwanted diffraction orders, can be removed.

3.2.3 Numerical simulation of linear light propagation

On propagating through free space, the complex angular spectrum $S(k_x, k_y, z = 0) = \mathcal{F}(E(x, y, 0))$ of a complex input field $E(x, y, 0)$ will remain constant. However, the relative phases of the plane wave components within the spectrum will change: The extra phase gained by a plane wave with longitudinal wave number k_z will be $\phi(z) = k_z z$. Expressing this phase change in terms of our spatial spectrum yields the so called transfer function of propagation through free space

$$T(k_x, k_y) = e^{ik_z z} = \exp \left[ik_0 z \sqrt{1 - \left(\frac{k_T}{k_0} \right)^2} \right], \quad (3.27)$$

also see [Goo17] for a detailed derivation and discussion. If the transversal wave number is sufficiently small, the paraxial transfer function

$$T(k_x, k_y) = \exp \left[ik_0 z \left(1 - \frac{k_T^2}{2k_0^2} \right) \right] \quad (3.28)$$

can be used. The propagated angular spectrum $S(k_x, k_y, z) = T(k_x, k_y) S(k_x, k_y, z = 0)$ can then be used to calculate the propagated optical field as

$$E(x, y, z) = \mathcal{F}^{-1} (T(k_x, k_y) \mathcal{F} (E(x, y, 0))). \quad (3.29)$$

As the paraxial transfer function is separable with respect to x and y , the calculation of the paraxial propagation for separable fields can be done in 1D for each dimension, also see Eq. 3.18.

Making use of the transfer function for optical propagation in combination with discrete Fourier transforms (DFT), the spatial evolution of the optical field can be calculated numerically. This propagation yields accurate results for arbitrary fields, when the non-paraxial transfer function, Eq. 3.27 is used. Fast Fourier Transform (FFT) algorithms [Pre+07] enable the calculation of even very large fields if sufficient memory is available. Here, the Python package "pyfftw" [Gom22] is used, which is a wrapper for the widely used FFTW library.

The sampling requirements and the computational complexity of DFTs are discussed in detail in [Goo17]. In particular, to avoid aliasing, any parts of the numerical box in which the amplitude of the field is significant, need to be sampled at a spatial frequency f_{samp} that is higher than twice the highest frequency f_{sig} in the signal, also see Nyquist–Shannon sampling theorem. Frequencies higher than $f_{\text{lim}} = 1/\lambda$, however, can be neglected as these correspond to evanescent waves, which do not propagate further.

The number of pixels $n_x = 2x_{\text{lim}} f_{\text{samp}} = 4x_{\text{lim}} f_{\text{sig}}$ is required to resolve frequencies up to f_{sig} in a box with half width x_{lim} . The box size needs to cover the size of the aperture or the parts of the beam that carry significant energy. If all propagating spatial frequencies for an optical wavelength $\lambda = 1030$ nm need to be resolved in 2D for a Gaussian beam with half width $w_0 = 2.65$ mm and $x_{\text{lim}} = 2w_0$, more than 400 Megapixels are required. With a typical size of 48 bytes per pixel³, a single field would require more than 10 GB of memory, exceeding the available memory of the local computer used in this work. The propagation of such large fields can be calculated by using multiprocessing routines to distribute the data on many processors in computational clusters ("supercomputers").

Alternatively, the number of pixels can be reduced for example by reducing the beam size, but care needs to be taken to scale all relevant parameters, so that the effect under consideration can still be observed, for an example also see Sec. 3.7.1.

3.3 The 1D case: Airy beam and Airy Gauss beam

Based in quantum mechanics, Berry and Balazs [BB79] demonstrated the non dispersive character of an Airy wave packet. Due to the parallel structure of the potential free Schrödinger equation and the paraxial Helmholtz equation, see Eq. 3.7, it is clear by direct analogy, that an electric field

$$E(\xi, 0) = \text{Ai}(\xi), \quad (3.30)$$

where $\text{Ai}(\xi) = 1/\pi \int_0^\infty \cos(t^3/3 + \xi t) dt$ is a solution of the Airy equation $f'' - xf = 0$ [Mil74] and $\xi = x/x_0$ is a non dimensional length, will not diffract during propagation. Indeed, solving the normalized, one dimensional Helmholtz equation (also see Eq. 3.7)

$$\left(\frac{\partial^2}{\partial \xi^2} + i2 \frac{\partial}{\partial \xi} \right) E = 0, \quad (3.31)$$

for a dimensionless longitudinal coordinate $\zeta = 2z/(kx_0^2)$ yields

$$E(\xi, \zeta) = \text{Ai} \left(\xi - \frac{\zeta^2}{4} \right) \exp \left[\frac{i\zeta}{2} \left(\xi - \frac{\zeta^2}{6} \right) \right]. \quad (3.32)$$

The non-diffracting character of the beam is clear, when considering the intensity

³Standard size of complex number in Python.

$$I(\xi, \zeta) \propto |E(\xi, \zeta)|^2 = \text{Ai}^2 \left(\xi - \frac{\zeta^2}{4} \right). \quad (3.33)$$

which does not change shape, but is merely shifted along the trajectory $\xi = \zeta^2/4$. The electric field as given in Eq. 3.30, however, is not square normalizable and carries infinite energy. A physical solution with finite energy is given when the slowly decaying tail of the Airy function is apodized by an exponential function [SC07], so that

$$E(\xi, 0) = \text{Ai}(\xi) \exp [a\xi] \quad (3.34)$$

for $a > 0$ and consequently

$$E(\xi, \zeta) = \text{Ai} \left(\xi - \frac{\zeta^2}{4} + ia\zeta \right) \exp \left[a\xi - \frac{a\zeta^2}{2} - \frac{i\zeta}{2} \left(\xi + a^2 - \frac{\zeta^2}{6} \right) \right]. \quad (3.35)$$

Due to the finite transversal extent, the beam has to have a finite length and indeed, by considering the real part in the exponential, that depends on ζ , one finds that the field drops to $1/e$ of its maximum value at $\zeta = \sqrt{2/a}$. If a is small, the width of the main lobe is further given by the first zero of the Airy function at $\xi = 1.6$.

The Fourier spectrum of this normalized field is given by [SC07]

$$S(\kappa) = \mathcal{F} (E(\xi, \zeta = 0)) = \exp [-a\kappa^2] \exp \left[\frac{i}{3} (\kappa^3 - 3a^2\kappa - ia^3) \right], \quad (3.36)$$

which corresponds to a Gaussian with a cubic phase. Considering the Fourier transform properties of an ideal lens, the Airy beam can in paraxial conditions be produced by focusing a Gaussian beam with a cubic phase⁴. We now can introduce the scaling factor β for the cubic phase, so that $\kappa = \beta x$ and the Gaussian half beam width (at $1/e^2$ intensity) w_0 , so that $a = 1/(w_0^2\beta^2)$. With an optical wavelength λ and a focal length f , we obtain the transverse length scale factor $x_0^{1D} = f\beta/k$.

Note that as the field curvature is reduced when a beam propagates from air into glass, for all calculations of the Airy focus shape in the material, the focal length has to be adjusted as $f = f_0 n$ where f_0 is the focal length in air and n the refractive index of the material.⁵ The wave number k as introduced above also depends on n , so that $k = k_v n$ for a wave number k_v in vacuum.

The propagation features of the 1D Airy Gauss beam can be seen in direct comparison with the corresponding Gaussian beam for the same focussing conditions but without the cubic phase in Fig. 3.4. As the cubic scale factor is increased, the peak intensity but also the intensity contrast along the propagation decreases. One can clearly see the non-diffracting character for $\beta = \beta_0$ in Fig. 3.4, as the intensity profile hardly changes at all. For the intermediate case $\beta = 0.6\beta_0$, one can see that the curvature of the main lobe trajectory is larger than for $\beta = \beta_0$, but the length over which the non-diffracting character and the parabolic main lobe trajectory is exhibited decreases [BS07]. Note also that the focal contrast between main lobe and first side lobe is reduced for larger values of β .

This 1D Airy can be produced by a phase mask in combination with a cylindrical lens. If a rotationally symmetric microscope objective is used, the intensity will be scaled by the evolution of the Gaussian in the perpendicular direction and decay with the Rayleigh length.

⁴Neglecting the linear phase term, which will result in a small lateral offset behind the lens.

⁵The deviation of the actual focus position in the glass sheet from the focus position in air, on the other hand, depends on the distance between glass and focusing optics, see Fig. 4.1.

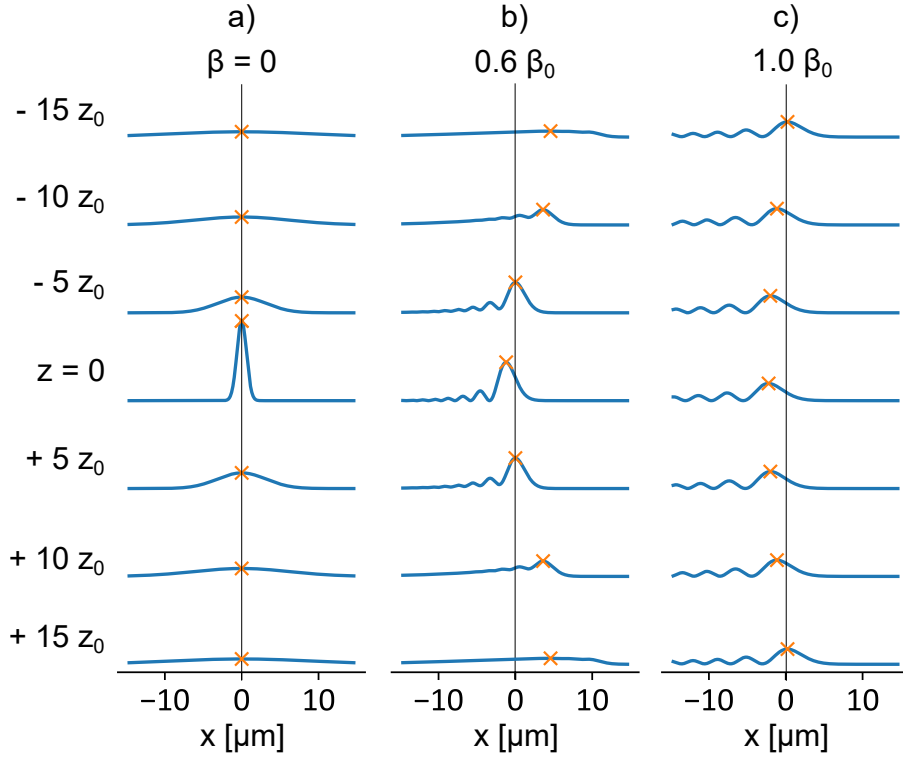


FIGURE 3.4: Lateral intensity profiles demonstrating the propagation dynamics of the 1D Airy Gauss beam for two cubic scale factors (b, c) and as a result a different confinement. The propagation distance z is given in terms of the Rayleigh length z_0 of the corresponding Gaussian beam (a). Parameters are as in Sec. 4.1 with $f = 10$ mm.

3.4 2D Airy Gauss beam

To obtain an extended focal line, two 1D Airy beam profiles can be combined along orthogonal axes $x' = (x + y)/\sqrt{2}$ and $y' = (x - y)/\sqrt{2}$, so that

$$E_0(x, y) = A_0 \exp\left[-\frac{x^2 + y^2}{w_0^2}\right] \exp[i\beta^3(x^3/3 + xy^2)/\sqrt{2}]. \quad (3.37)$$

with the normalized amplitude of the Gaussian beam, as given in Eq. 3.11. The corresponding phase is shown in Fig. 3.5. The phase profile can be imprinted on a Gaussian input beam by a specifically designed phase mask, such as a diffractive optical element (DOE, also see Sec. 3.6), a spatial light modulator (SLM) or cylindrical lenses [Pap+10; RAG18; Yan+14].

Along the axes x' and y' , i.e. the direction of the cubic phases, the beam laterally extends into characteristic "legs", see Fig. 3.5 b).

The propagation of the complex electric field with respect to the focal plane at $\zeta = 0$ is then given by

$$E(x, y, \zeta) = \frac{A_0}{i\lambda f} \text{Ai}\left(\frac{x-y}{x_0} - \frac{\zeta^2}{4} + ia\zeta\right) \text{Ai}\left(\frac{x+y}{x_0} - \frac{\zeta^2}{4} + ia\zeta\right) \\ \times \exp\left[a\left(\frac{2x}{x_0} - \zeta^2\right) - i\zeta\left(\frac{\zeta^2}{6} + a^2 + \frac{x}{x_0}\right)\right], \quad (3.38)$$

using Eq. 3.24 and redefining $x_0 = \sqrt{(2)}f\beta/k$ for convenience. The main lobe of the intensity profile then follows a parabolic trajectory $p(z)$ in the xz -plane with

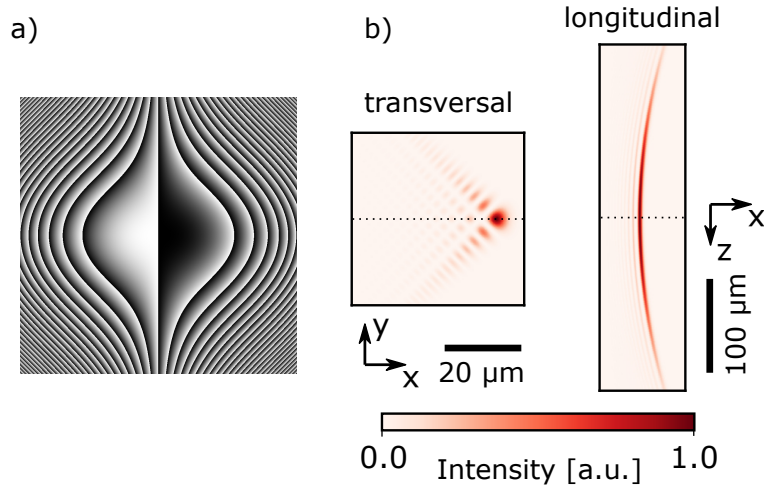


FIGURE 3.5: Phase distributions for 1D and 2D Airy beam and the theoretical intensity profiles for an Airy beam with $f = 10$ mm and $\beta = 3^{1/3}$ mm $^{-1}$. For the phase distributions the colors represent values from 0 (black) to 2π (white).

$$p(z) = qz^2 \quad \text{and} \quad q = \frac{1}{k^2 x_0^3} = \frac{k}{(f\beta\sqrt{2})^3}, \quad (3.39)$$

see also Fig. 3.5 b). At the vertex of the parabola this corresponds to an effective radius

$$r = 1/(2q) = k^2 x_0^3 / 2 = \frac{\sqrt{2}(f\beta)^3}{k} \quad (3.40)$$

and the angle α between the optical axis and the line focus varies along z a

$$\alpha(z) = \arctan(2qz), \quad (3.41)$$

also see Fig. 3.6. As the beam diffracts in two dimensions, the non dimensional half length reduces to $\zeta = \sqrt{1/a}$ and the total length

$$l \approx 2w_0 f^2 \beta^3 / k = \frac{\sqrt{2}w_0 r}{f} = \sqrt{2} \text{NA}_{\text{eff}} r \quad (3.42)$$

where the intensity of the main lobe exceeds $1/e^2$ of its maximum and where the effective numerical aperture $\text{NA}_{\text{eff}} = w_0/f = a_{\text{fill}} \text{NA}$ may only be a fraction of the numerical aperture of the focussing optics, which is given in terms of a fill factor a_{fill} . While we are generally aiming for a long and strongly curved focal line, it is clear from Eq. 3.42, that there is a trade-off between length and curvature, but with a larger NA larger curvatures can be reached for a given length or vice versa. The angle

$$\alpha_{1/e^2} = \arctan(w_0/f) = \arctan(\text{NA}_{\text{eff}}) \quad (3.43)$$

reached at the $1/e^2$ points, consequently can also be maximized by maximising the used NA. Microscope objectives with an NA up to 0.65 are commercially available for high power applications in the near infrared, which would correspond to a theoretical maximal bevel angle to 24° in glass if $a_{\text{fill}} = 1$, i.e. for a Gaussian beam this means overfilling the optics. For an unclipped Gaussian beam typically $a_{\text{fill}} \leq 0.5$ is used. For more details on apodized versions of the Airy beam, e.g. the effect of a top hat instead of a Gaussian input beam, see [RHD13; Cho+13].

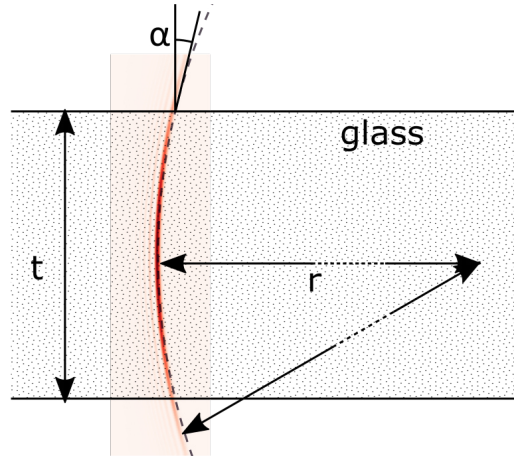


FIGURE 3.6: Schematic representation of the positioning of an Airy beam focus with an effective radius r in a glass sheet of thickness t for a micro perforation process. For a symmetric position, the bevel angle of the resulting edge $\alpha = \arctan\left(\frac{kt}{(f\beta\sqrt{2})^3}\right)$, see Eq. 3.39 and Eq. 3.41.

focal length f [mm]	10	20
NA_{eff}	0.265	0.133
bending radius, r [mm]	1.48	11.9
$1/e^2$ length [mm]	0.556	2.22
$1/e^2$ angle [°]	100	5.2
bevel angle $\alpha(t)$ [°]		
$t = 0.3$ mm	5.8	0.73
$t = 0.5$ mm	9.6	1.2
$t = 1$ mm	19	2.4
$t = 2$ mm	34	4.8

TABLE 3.1: Scaling of Airy beam in glass for the two focal lengths used with $w_0 = 2.65$ mm, $\beta_0 = 3^{1/3}$ mm $^{-1}$ and $\lambda = 1030$ nm.

Another aspect to consider is the focal contrast, i.e. the intensity ratio of the main lobe with respect to the largest lobe. By expressing the cubic phase in terms of the confinement factor a and inserting this into the expression of the length, we get

$$l = \frac{2}{a^{3/2} k \text{NA}_{\text{eff}}^2}, \quad (3.44)$$

which means that the length for a given NA and wavelength will decrease if the focal contrast is increased, which means moving away from the ideal Airy beam with confinement factor $a = 0$. Fig. 3.7 shows this trade of between length and focal contrast.

For a micro perforation process in which the glass sheet is fully perforated, the top angle α of the resulting edge does not depend on the length of the Airy beam, but on the thickness t of the sheet and the curvature of the Airy beam, schematically shown in Fig. 3.6. Theoretical values for the scaling of the Airy beam in glass are given in table 3.1 for optical configurations that will be used in this study and for various glass thicknesses.

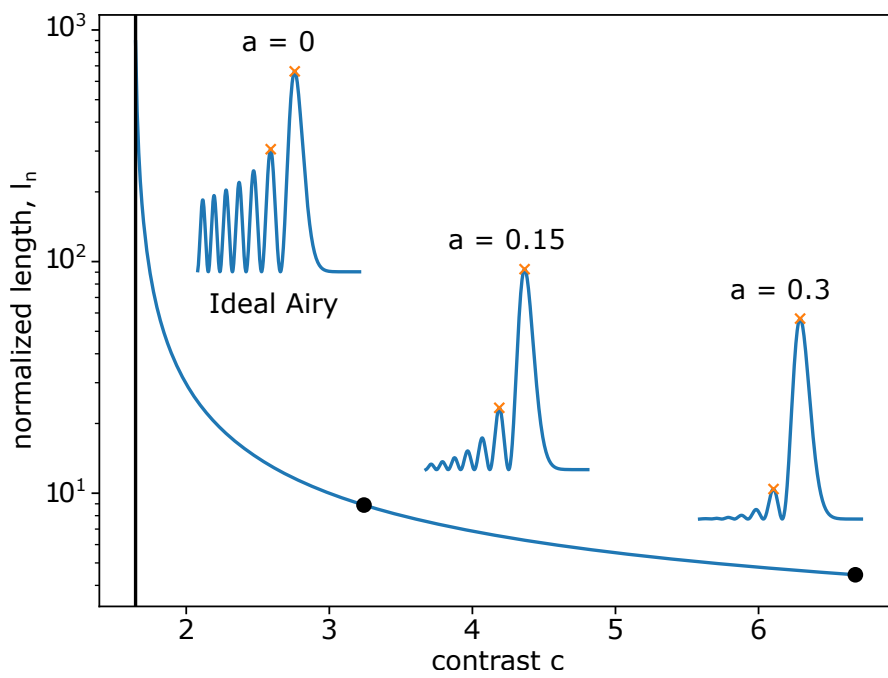


FIGURE 3.7: Normalized length $l_n = l \text{NA}_{\text{eff}}^2/k$ as a function of the focal contrast c . The contrast is directly related to the confinement factor a and exemplary focal 1D intensity distributions, given by $z = 0$ in Eq. 3.35, are shown as insets. As the confinement is lowered going towards the ideal non diffracting Airy beam with infinite length, the contrast approaches a limit of 1.63.

3.5 Direct space production of the Airy beam - 4f setup

Alternatively to the Fourier space phase definition, the Airy beam can also be produced by defining the phase in direct space with an exponent of $3/2$ [CDH09; Fro+11]. The beam is then typically imaged by a 4f setup, similar to the Bessel beam setup presented in Fig. 2.3. As stated by [CDH09], this scaling of the direct space phase can be understood in terms of the approximate solution of the Airy function

$$\text{Ai}(x) \approx x^{-1/4} \exp \left[iCx^{3/2} \right], \quad (3.45)$$

where C is a constant and the slowly decaying amplitude term will be replaced by an apodizing function for physical beams.

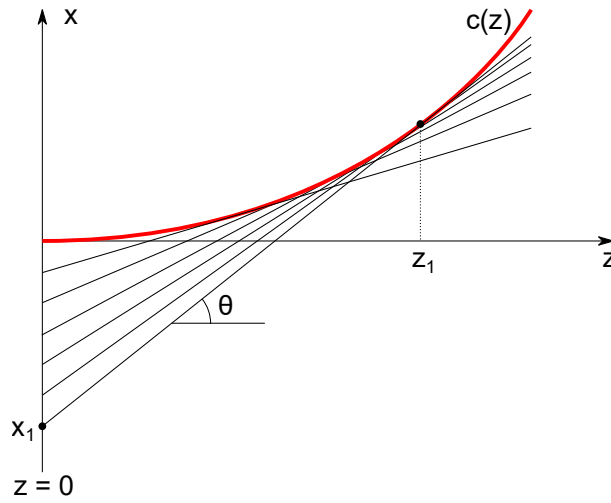


FIGURE 3.8: Geometrical concept for construction of a caustic $c(z)$ by a phase mask which is placed at $z = 0$.

The phase for direct space shaping can also be derived by means of a geometrical argument. Already Berry and Balazs [BB79] pointed out the caustic nature of the Airy beam. This means that the creation of a high intensity main lobe can be understood in terms of a group of rays that are all tangent to the caustic envelope $c(z)$, that defines the position of the main lobe, see Fig. 3.8. The slope $\tan(\theta)$ of a tangent to $c(z)$ at z_1 is given by $c'(z_1) = dc(z_1)/dz$ as well as by $(c(z_1) - x_1)/z_1$, so that for any monotonous function there is unique value of x_1 for a given $z = z_1$. Additionally using the requirement that the local wavefront at the phase mask must be perpendicular to the ray at x_1 , so that $d\phi(x_1)/dx = k \sin(\theta)$, one obtains [Fro+11]

$$\frac{d\phi(x)}{dx} = \frac{kc'(z)}{\sqrt{1 + [c'(z)]^2}} \quad (3.46)$$

which corresponds to a Legendre transform. For a parabolic curve $c(z) = qz^2$ this yields $\phi(x) = -4/3\sqrt{q}kx^{3/2}$ [Fro+11], so that by inserting the normalization factors from above, one obtains

$$\phi(x) = -4/3 \left(\frac{k}{f\beta\sqrt{2}} x \right)^{3/2}. \quad (3.47)$$

This would produce the focused beam as behind the Fourier lens, see Sec. 3.3. The steep phase gradients that are typically reached for tight focussing with small f are to realize in a phase mask, also see Sec. 3.6. To reach micro meter resolution, the direct space shaping is therefore combined

with a demagnifying telescope (e.g. in [Fro+11]), lowering the phase gradients at the phase mask. The cubic phase scaling factor behind a telescope with magnification M decreases to β/M .

3.6 Tools for wavefront modulation

Beam shaping for material processing applications is usually done with optical elements which alter the phase. Amplitude masks would reduce the pulse energy, which in many cases is a limiting factor, for example when maximizing the modification length, also see [Feu+19]. In addition, for high power applications the cooling of absorptive elements can be challenging and the energy lost at the amplitude mask makes the process less efficient.

For applications in research and development, electro-optical spatial light modulators (SLMs) are particularly useful, as they enable fast switching between different phase distributions. The phase difference can be induced by changes in the spatial length of the light path, for example by translation of micro mirrors in Digital micro mirror devices (DMDs), which additionally can make use of the varying deflection by the micro mirrors, or by changes of the refractive index, for example due to rotation of liquid crystals molecules in LC-SLMs.

A much better spatial resolution, however, is achieved by fixed optical elements, such as a lens, which induces the phase modulation by variations in surface height. For complex phase masks these are typically produced by multistep or greyscale lithography. These are often referred to as diffractive optical elements (DOEs), although the more general term beam shaping element is more appropriate: For wavefront modulators usually the instantaneous phase is considered. This reduces the optical path length difference that is required to one wavelength, which reduces the thickness of the optical element. Nevertheless, for low phase gradients and sufficiently high spatial resolution and a high number of discrete levels N for quantized phase masks, the optical element locally acts like a refractive optic. The high contrast required at the discontinuities that are included in the instantaneous phase poses a challenge in the design of phase masks. Also, at high phase gradients, i.e. strong local deflection, the interaction of the deflected light with the discontinuities can become significant and lead to scattering, i.e. loss of useable laser power.

Additionally, for high phase gradients, i.e. high spatial frequencies ν within the phase spectrum, the quantization of the phase mask becomes an important factor and directly affects the diffraction efficiency η , which represents the portion of input power that contributes to the desired beam shape (usually the first diffraction order). The diffraction efficiency [Goo17]

$$\eta = \left(\frac{N \sin\left(\frac{\pi}{N}\right)}{\pi} \right)^2 \quad (3.48)$$

for a quantized blazed phase grating as shown in Fig. 3.9 rapidly drops when the number of discrete levels N decreases. The limiting factor can be an inherently low N , as for binary gratings with $N = 2$ from single step lithography, or a low lateral resolution where effectively $N(\nu) = \lfloor 1/(l\nu) \rfloor$ where l

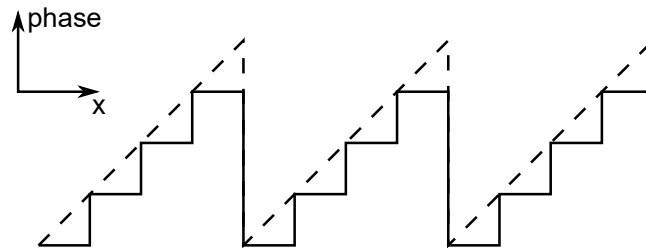


FIGURE 3.9: Sketch of a quantized blazed grating with $N = 4$. The dashed lines indicate the continuous, reduced phase that the quantized phase tends to as N increases.

represents the minimum resolvable lateral length scale of the phase mask. Spatial frequencies greater than $2/l$ are not sufficiently sampled and will not contribute significantly to the diffraction pattern.

The total resolution of the phase mask determines the bandwidth of spectrum that can be adequately represented. It thus acts as the available numerical aperture of the phase mask and limits for example the maximum angles of curved trajectories that can be produced with the optical element.

In this work both a fixed beam shaping element, later simply called DOE, and a LC-SLM are used as phase masks. In the following we will briefly discuss their working principles and their limitations.

3.6.1 Liquid crystal spatial light modulators

There are various types of spatial light modulators that make use of the birefringence of liquid crystals (LCs) for modulation of polarization, amplitude or phase, see [Goo17] and sources therein. In birefringent crystals, the refractive index depends on the orientation of the light polarization with respect to the crystal lattice. Liquid crystals are composed of birefringent molecules, which can alter their relative orientations, for example when an electric field is applied.

The most common application of liquid crystals is amplitude modulation in consumer liquid crystal displays (LCDs). This is typically achieved by combining the change in polarization in twisted nematic liquid crystals with polarizing filters at input (polariser) and output (analyser) plane, which can coincide for reflective configurations. Without polarizing filters the same display can be used for polarization control.

Phase modulation on the other hand is nearly exclusively done with untwisted nematic liquid crystals. Depending on their orientation with respect to the display they are called parallel aligned nematic (PAN) or vertically aligned nematic (VAN) [HOL22]. For light which is linearly polarized along a plane that contains two principal axes of the optical indicatrix, that correspond to different refractive indices n_1 and n_2 , the optical path length can be changed by rotating the liquid crystal molecules about the normal of that plane. To ensure an accurate translation of the greyscale phase mask to the the actual phase retardance, the device needs to be calibrated. The maximum phase shift, for which an upper limit is given by $\phi_{\max} = k_0|n_1 - n_2|t$, also depends on the thickness t of the LC layer and should be at least 2π for full phase control.

The pixel size of the active matrix that controls the LC rotation is limited in particular by the cross talk between neighbouring pixels [PEG12], which increases with increasing thickness t . While the number of phase levels is usually high for LC-SLMs, the typical pixel sizes of several micrometers pose the crucial limit for diffraction efficiencies at higher spatial frequencies.

It has been pointed out [Fla+19] that the lower angles for digital axicon profiles produced by SLMs can be increased virtually. For accelerated beams however, a large spatial bandwidth of the phase mask is important to produce a long focal line with strong curvature, also see Eq. 3.39 and Eq. 3.42.

Another important limitation of the available pulse energy after a LC-SLM is the fill factor, i.e. the proportion of the display area in which light is transmitted or reflected respectively. SLMs are built both in transmissive and reflective configuration but significantly higher fill factors are typically reached in reflective configuration [HSS05]. This can be understood in terms of the controlling electronics in the backplane of the SLM: While in transmission any non-transparent material will block the light, the backplane in an reflective SLM can be dielectrically coated. Reflective SLMs are typically realized as liquid crystal on silicon (LCOS) chips, which can be directly addressed electronically by an underlying CMOS chip.

The spatial light modulator used in this work, a Holoeye PLUTO-2 NIR 149, is a LCOS chip with a dielectric coating for the relevant NIR wavelength range, see Tab. 3.2 for the relevant specifications.

Phase levels	256 (8 bit)
Active area	15.36 mm × 8.64 mm
Resolution	1920 × 1080 pixels
Pixel pitch	8.0 μm
Fill factor	93%
Reflectivity at $\lambda = 1030$ nm	93%

TABLE 3.2: Spatial light modulator (Holoeye PLUTO-2 NIR 149) specifications

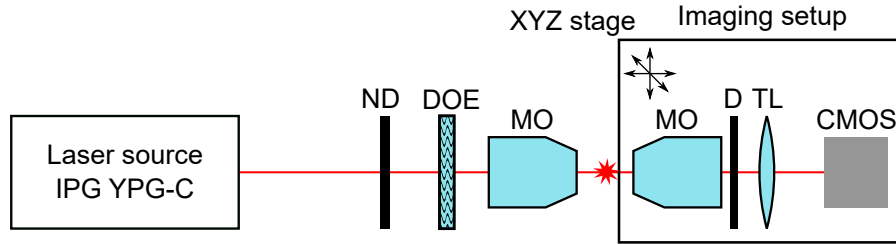


FIGURE 3.10: Optical setup for imaging the Airy Profile in air. The Airy beam focus is produced by adjusting the pulse energy with neutral density filters (ND) adding a cubic phase with a diffractive optical element (DOE) and focusing the beam by a microscope objective (MO). The imaging setup used to record the resulting focus is comprised of a microscope objective (MO), a diaphragm (D), a tube lens (TL) and a camera (CMOS).

3.6.2 Diffractive optical elements and fixed phase masks

While fixed phase masks, such as diffractive optical elements (DOEs), are less flexible than spatial light modulators, they have several advantages that make them favourable tools for beam shaping: There is no steering electronics that blocks light, i.e. they have a fill factor of 100%. Typically made from fused silica, DOEs generally have very high damage thresholds. A lateral resolution much smaller than the NIR wavelength can readily be achieved by lithographic methods nowadays, so that theoretically any propagating parts of the spatial spectrum (i.e. non-evanescent waves) can be realized with significant diffraction efficiencies, if scattering effects at the discontinuities can be neglected. In practice, at a laser wavelength $\lambda = 1 \mu\text{m}$ high diffraction efficiencies can be reached up to beam deflections of 10° , which corresponds to a grating period $p = 1/\nu = 10 \mu\text{m}$ [Fla+19], with DOEs produced by laser grayscale lithography. The quasi continuous phase variation of grayscale lithography leads to very high diffraction efficiencies ($> 99\%$) [Fla+19]. The diffractive optical element used in this study for the generation of the Airy beam (Airy Beam Generator, Holo/Or) has 16 levels, which corresponds to a theoretical diffraction efficiency of 98.7%, see Eq. 3.48.

3.7 Measurements of Airy profiles in air

As a first characterization of the experimentally produced Airy beams, I measured the linear propagation in air using an optical setup with the diffractive optical element (DOE) with a fixed cubic phase $\beta_0 = 3^{1/3} \text{mm}^{-1}$. The laser used for these first experiments was an IPG YPG-C, see Tab. 3.3.

I took care to always use a microscope objective with higher NA compared to the focusing optics, unless otherwise stated the objective was a Nikon N40X-PF. This objective has a plan fluorite design and is corrected also for the near infrared (NIR)⁶. The tube lens always was a Thorlabs TTL200-S8 with a focal length of 200 mm. The complementary metal oxide semiconductor (CMOS) camera used

⁶The correction is done for microscopy applications including a cover glass of 0.17 mm thickness. The spherical aberration that is induced by the lack of a cover glass in my setup can be neglected because the focussing optics had a sufficiently low numerical aperture.

	Amphos 200 XHE	Amplitude Tangor 50	IPG YPG-C
Wavelength λ [nm]	1030	1030	1064
Beam radius w_0 [mm]	2.65	3.3	3 to 4.5
Beam quality M^2	1.1	1.09	1.5
Polarization	linear	linear	random
Pulse duration t_p [ps]	1 to 10	0.41 to 3.7	10^5
Pulses in burst n_{burst}	1 to 4	1 to 246	n/a
Intra burst period [ns]	25	24.4	n/a
Max. pulse energy E_{burst} [μ J]	> 1700	300	n/a

TABLE 3.3: Specifications of lasers used in this study

in the imaging setup was a Daheng Imaging MER-530-20GM-P NIR, with an improved performance in the near infrared.

Focusing with spherical lenses (Thorlabs AL1210, AL1225, AL2018) in the first trial lead to significant distortions of the beam compared to the theoretical profile, see Fig. 3.11 b), which also affected the resulting glass modifications, see appendix A for more details. Similar features could be seen in linear simulations of beam propagation for a spherically aberrated lens, see also Sec. 3.7.1.

To avoid these distortions in further experiments I used a microscope objective (MO, Trumpf TopCleave, two different models with focal lengths 10 mm and 20 mm respectively) as focusing optics as shown in Fig. 3.10. The beam width and thus the effective NA was limited by the clear aperture of the DOE (9 mm clear aperture diameter).

To minimize the effect of an extra spherical contribution, which may affect the effective NA, the phase mask has to be placed at the front focal plane of the focussing optics, see Eq. 3.24. I estimated the position of the front focal plane by illuminating the rear side of the MO with a collimated beam and measuring the beam diameter behind the MO. I found that the front focal plane of the MO lies within the housing of the MO, so the DOE could not be placed exactly at this plane. Rather the DOE has been placed as close to the MO as the mechanical parts allowed (effective distance 4 mm).

This way, clean intensity profiles were achieved, see Fig. 3.11 and Fig. 3.12. For example, the bending radius $r = (5.90 \pm 0.07)$ mm for $f = 20$ mm is very close to the theoretical value of 5.75 mm, see Eq. 3.40. Also, deviations to higher radii can be expected, if the cross section for analysis is not exactly placed on the mirror plane of the Airy beam. The corresponding observed length $l = (1.57 \pm 0.04)$ mm is in the middle of the range, that is expected theoretically (1.2 to 1.8 mm, see Eq. 3.40).

For a direct comparison with the micro machining experiments, as shown in Fig. 4.2, the intensity profile was again recorded in air using the Amplitude laser which has the same wavelength as the Amphos laser that is used for micro machining.

3.7.1 Effect of spherical aberration

Qualitative comparisons of the intensity profiles measured in air with simulations of an ideal lens with added fourth order spherical aberration indicate that the fragmented character observed for the asphere as shown in Fig. 3.11 b) can be explained by spherical aberration.

For the simulation a fourth order term was added to the phase of the ideal thin lens so that the total phase of the lens

$$\phi_{tl} = k_0 \left(\frac{1}{2f} r^2 + c_4 (12.5/f^3) r^4 \right). \quad (3.49)$$

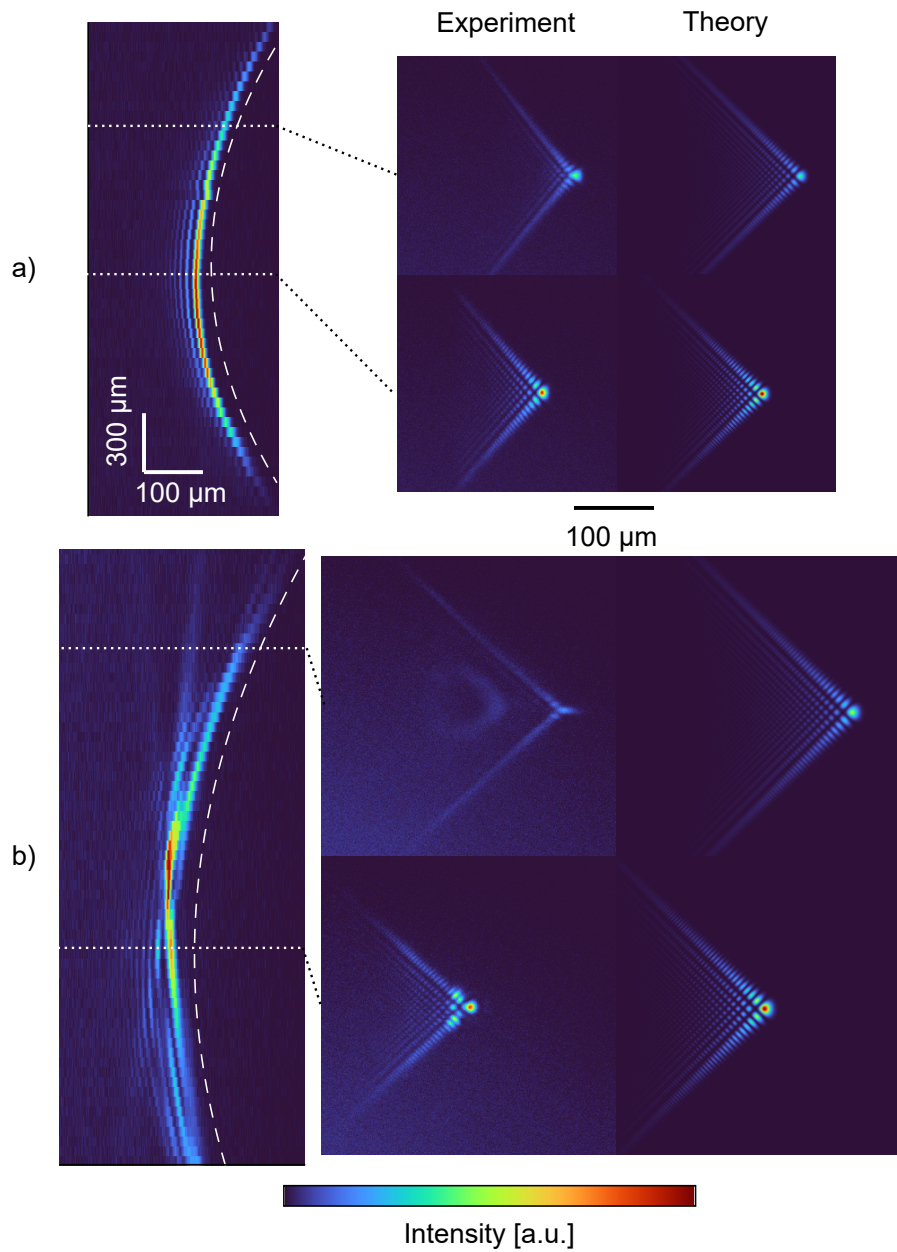


FIGURE 3.11: Intensity profiles measured in air for a microscope objective with $f = 20$ mm (a) and an asphere with $f = 25$ mm (b). The longitudinal profiles on the left are drawn to same scale and transversal sections at the indicated positions are shown on the right for experiment and theory. Here, the Trumpf TopCleave $f = 10$ mm objective is used for imaging.

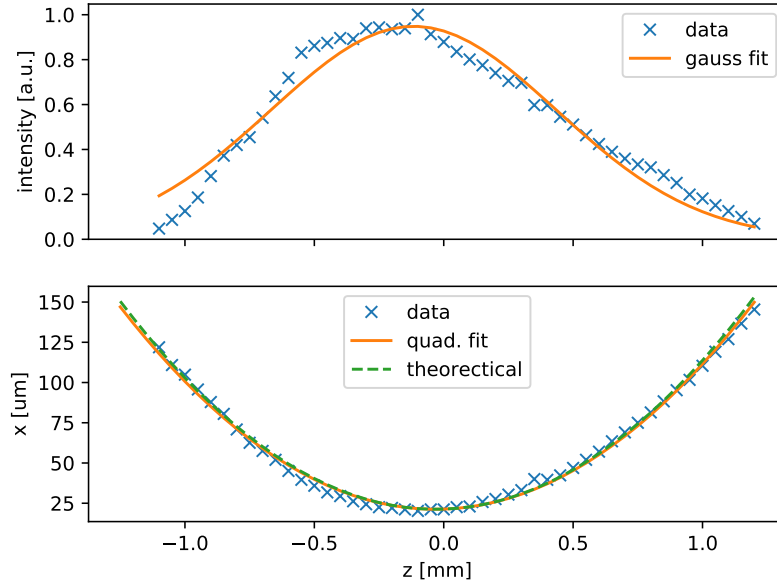


FIGURE 3.12: Intensity (top) and lateral position (bottom) of the Airy main lobe for $f = 20$ mm as shown in Fig. 3.11 a). The fits yields a length $l = (1.57 \pm 0.04)$ mm and a bending radius $r = (5.90 \pm 0.07)$ mm.

where the constant factor $12.5/f^3$ is chosen for a convenient scaling of the spherical aberration. With spherical aberration no separation of variables is possible, therefore the 2D FFT propagator had to be used. In order to enable simulation on a local machine and to save computation time (also see Sec. 3.2.3), the simulations were performed for a smaller beam than the experimental system, but the cubic scale factor β has been adjusted accordingly to obtain the same confinement factor a . The simulation parameters are listed in Tab. 3.4.

Two characteristic transversal cross sections along the propagation for experiment and simulation respectively are shown in Fig. 3.13 for demonstration. This is plausible as the aspheres are usually corrected for spherical aberration to create a single spot from a collimated beam, but not for imaging the broader range of spatial frequencies which is necessary for creating the Airy beam.

In the case of the focusing with aspheres, spherical aberration is detrimental to the industrial process because of the high intensity in the side lobes.

parameter	value	unit
physical parameters		
optical wavelength λ	1030	nm
gaussian beam width w	500	μm
cubic scale factor β	$(2.65/0.5)^{3^{1/3}}$	mm^{-1}
focal length f	10	mm
spherical aberration c_4	0 ... 0.3	-
numerical parameters		
n_x	4096	-
x_{lim}	2	mm

TABLE 3.4: Parameters for linear simulations of Airy beam with spherical aberration.

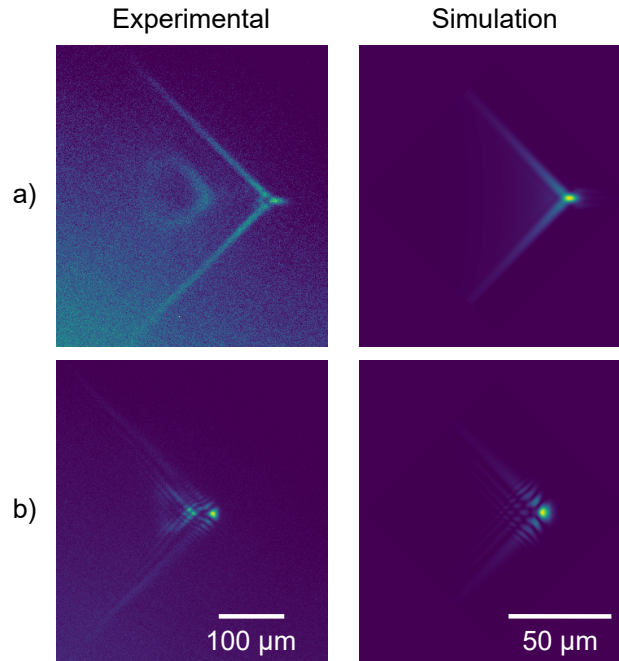


FIGURE 3.13: Experimental intensity profiles measured in air and simulated intensity profiles with fourth order spherical aberration showing characteristic profiles of a spherically aberrated Airy beam. Note that while the focussing conditions are different for experiment (AL1225, $f=25$ mm) and simulation ($f=10$ mm) characteristic features are shared in the evolution of the intensity profile, in particular the continuous side lobes (a) and the bend side lobes (b). The parameters used for the linear simulations are given in Tab. 3.4. Experimental profiles from same recording as Fig. 3.11.

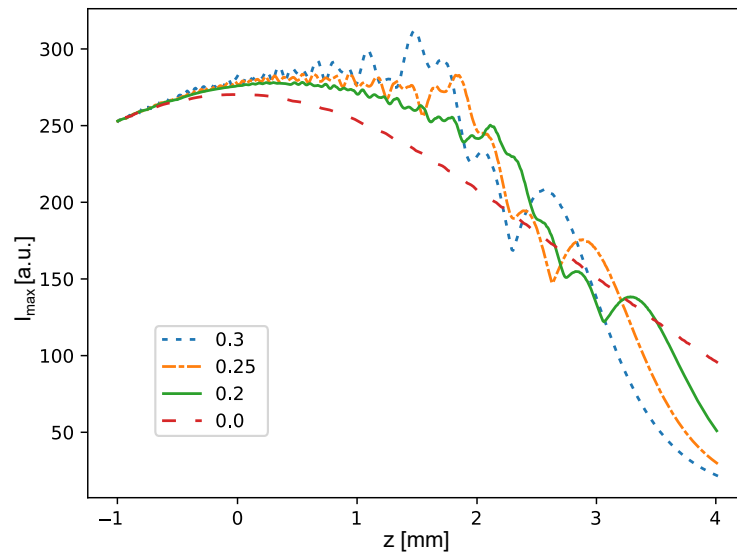


FIGURE 3.14: Effect of spherical aberration in simulated longitudinal intensity profiles showing the intensity of the main lobe. By increasing the characteristic modulations of spherical aberration can be seen.

Linear simulations with moderate spherical aberration however, indicate that this can lead to an extended region with an approximately uniform intensity of the main lobe, see Fig. 3.14. Increasingly large spherical aberration leads to increased oscillations and asymmetry about the linear focus, similarly to the features of the spherically aberrated Gaussian beam, see Sec. 2.2.3.

confinement factor	a	$1/(w_0^2\beta^2)$
transverse length scale factor	x_0	$\sqrt{2}f\beta/k$
longitudinal length scale factor	ζ/z	$2/(kx_0)^2$
bending radius of focal line	r	$k^2x_0^3/2 = \sqrt{2}(f\beta)^3/k$
full $1/e^2$ length of focal line	l	$2w_0f^2\beta^3/k = \sqrt{2}NA_{\text{eff}}r$
$1/e^2$ angle	α_{1/e^2}	$\arctan(NA_{\text{eff}})$

TABLE 3.5: Scaling factors and relations for the Airy beam, for details see Sec. 3.4.

3.8 Summary

The optical Airy beam is a one dimensional non-diffracting, caustic beam with a main lobe that follows a parabolic trajectory during propagation. The propagation of the complex field envelope can be calculated analytically as a solution of the paraxial Helmholtz equation. A physical, finite-energy solution is given by the Airy Gauss beam that can be created by focusing a beam with Gaussian amplitude and cubic phase, but also a direct space shaping is possible with an exponential $3/2$ scaling of the phase.

A 2D version of the Airy beam with a curved focal line is given by the orthogonal interference of two 1D Airy profiles. The scaling relations of the 2D Airy Gauss beam are summarized in Tab. 3.5. The focal contrast, i.e. the ratio between the main lobe and the first side lobe, reduces with the confinement factor and asymptotically approaches a value of 1.63 for the ideal Airy beam.

Diffractive optical elements with high diffraction efficiency up to large spatial frequencies and a high damage threshold are useful for material processing applications. LCOS spatial light modulators are more limited in spectral bandwidth that can be imaged with high efficiency, but they are well suited for testing new beam shapes due to their changeable phase. Airy beam profiles produced with the two focusing microscope objectives used in this study show the expected behaviour in linear propagation. Low spherical aberration can homogenize the longitudinal intensity profile on one side of the linear focus, but strong spherical aberration may be responsible for detrimental distortions of the focal line.

Chapter 4

2D Airy Gauss modifications and their application to glass cutting

The 2D Airy-Gauss beam is a good starting point and an interesting benchmark when exploring beam shapes for creating curved edges by a USP laser process. Its Gaussian apodization that is typically given as output from industrial lasers and the existence of an analytical expression for its linear propagation respectively mean that it can be produced with a small experimental setup and the numerical load for simulations is strongly reduced. In this section methods and results based on this well established beam shape are presented and discussed. Despite the important limitations of its applicability for glass cutting, the results achieved with the 2D Airy-Gauss beam provides a fundamental understanding for more adapted beam shapes that will be presented in the following section and in Chapter 6.

4.1 Laser processing and beam imaging methods

The micro machining was performed at an integrated industrial laser machine with an Amphos 200 XHE as laser source, see Tab. 3.3. As described in Sec. 3.4, the Airy-Gauss beam can be readily produced as the focal image of a beam with a cubic phase, see Fig. 4.1 a). For all micro machining experiments at this machine I used the HoloOr Airy Beam Generator as phase mask, also see Sec. 3.7. Sheets of borosilicate glass (SCHOTT Borofloat[®] 33) of thicknesses between 0.3 mm and 6.5 mm were placed horizontally on a motorized XY stage with the laser beam coming from the top, parallel to the Z axis along which a motorized linear stage is used to move the focusing optics.

The Airy beam profile was characterized by inspecting the ablation pattern at the glass surface for various distances between focusing optics and glass sheet. The focus position was then defined as the half-way position within the depth range in which an ablation pattern is observed. For a symmetric longitudinal intensity distribution, which is expected for the Airy beam, this corresponds to the position, for which the maximum intensity lies at the surface of the glass sheet, see Fig. 4.1 b). The focus position was thus determined to an accuracy of 50 μm .

As the orientation of the DOE could only roughly be adjusted by the lens tube system, the ablation pattern was also used to determine the orientation of the Airy profile. The XY movement was then adjusted to ensure that the cutting lines are perpendicular to the acceleration direction of the beam, which lies in the mirror plane of the beam, thus maximising the curvature of the cross section profile. The focus of the Airy beam was subsequently placed within the glass volume by decreasing the distance between the focusing optics and the glass sheet by a defined distance Δz , see Fig. 4.1 a). The glass was then moved horizontally with respect to the laser beam while picking single laser pulses, resulting in discrete modifications, separated along the lateral translation direction by a constant distance, a so-called pitch, of 10, 25 or 50 μm respectively.

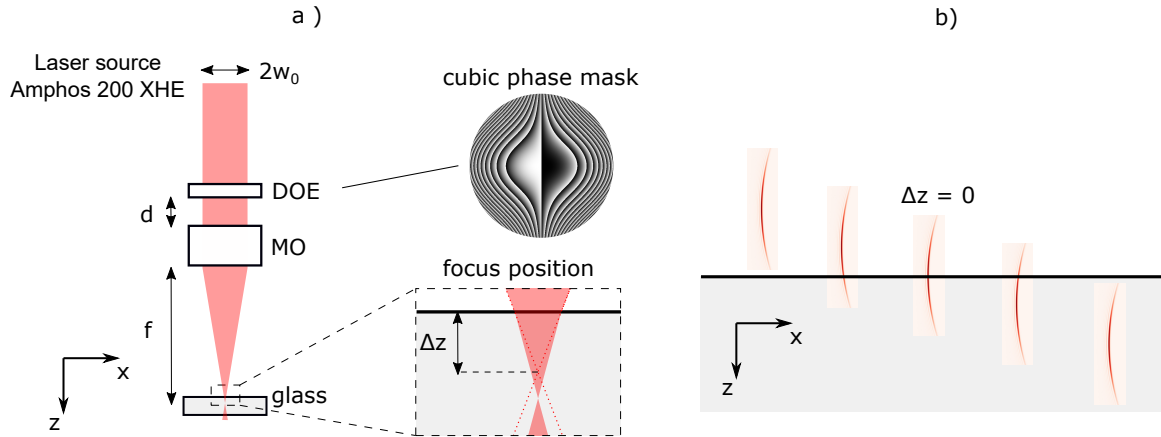


FIGURE 4.1: Experimental 2f-setup (a) used for creating an Airy-Gauss beam at the industrial laser machine. Throughout the thesis, the focus position is given as the shift Δz of the glass surface with respect to the focus position in air (dotted line). The reference position is defined with respect to the glass surface (b).

4.2 Airy volume modifications

In order to first examine the pure volume modification, I placed the focus deeply within a 6.5 mm thick glass sheet ($\Delta z = 2$ mm) thus avoiding plasma ignition at the surface. I inspected the longitudinal profile of the volume modifications by cutting the glass perpendicularly to the above mentioned lateral translation direction, polishing it and looking along this translation direction using reflected light microscopy (Keyence VHX 6000). For these profile measurements I took special care to avoid double shots, implementing a pulse on demand operation, and only single pulses were used.

I found that the volume modifications follow the expected curvature for a wide range of experimental parameters, see Fig. 4.2. With increasing pulse energy the trajectory remains unchanged while the length and lateral extent of the modifications increase, for $f = 20$ mm reaching lengths of up to more than 2 mm and a maximum angle $a_{max} = 5^\circ$, also see Fig. 4.3. For 1 ps pulses the modifications remain broad and indistinct. More confined and stronger modifications are observed for longer pulse durations. The experimental profiles show a shift of the maximum intensity or damage respectively with respect to the vertex of the ideal trajectory, which can be attributed to a slight misalignment of the Gaussian input beam. This effect was made use of in further experiments and will be discussed in detail in Sec. 5. In particular, however, I observe an increasingly asymmetric damage distribution along the parabola with increasing pulse energy, with the most extensive damage shifted towards the laser source and a long tail away from it.

For a more quantitative analysis of the length, curvature and asymmetry of the modifications, the end points of the modifications and the position with the damage largest extent were recorded five times in total by three different persons. The average curvature of the fits to the longest 6 lines is $r = (11.6 \pm 1.8)$ mm¹, which is in very good agreement with the theoretical value $r_{th} = 11.9$ mm. Going towards a more reproducible analysis, a specifically developed line detection algorithm, see Fig. 4.4, was tested in comparison with the manual data. The results of the algorithm depend on the parameters used for image processing, for details see appendix B. Reliable detection for all but the two smallest manually detected modifications could be achieved, also see the breakdown of the measured length for low energies in Fig. 4.5. The resulting radius $r = (10.4 \pm 0.4)$ mm is significantly lower than the theoretical value, which can be explained by the influence of the side lobes: An absorption in the side lobes would lead to a preferential broadening away from the main lobe, thus increasing the curvature.

¹If all discernible modifications are included, which partially suffer from rough estimates, the result is $r = (10 \pm 6)$ mm.

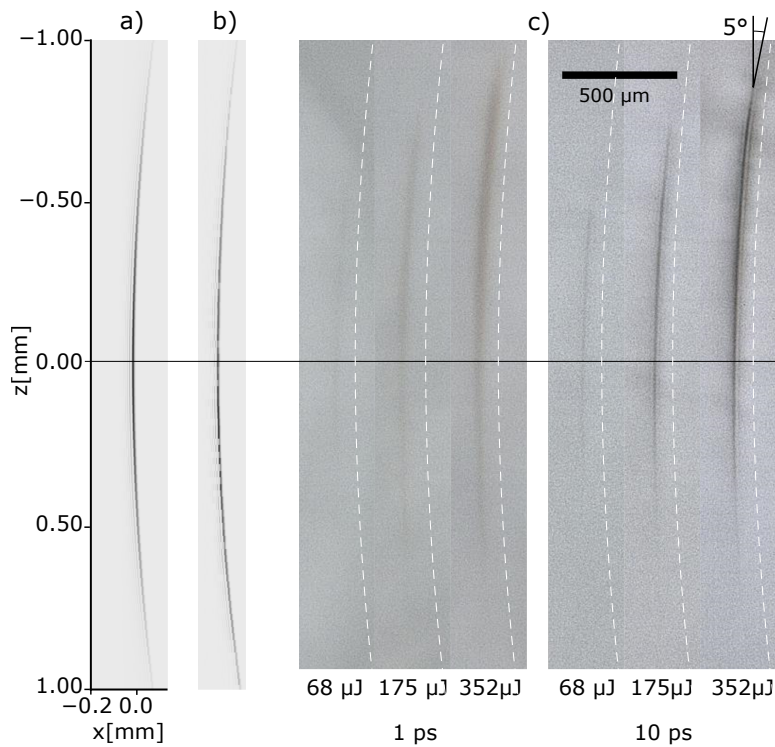


FIGURE 4.2: Light microscopy cross sections of permanent in-volume modifications for $f = 20$ mm in glass (c) follow the parabolic trajectory that is theoretically expected (a) from Eq. 3.38 and has been measured in air (b). This profile is also shown by the dashed white lines on the microscope images for comparison. The z scale of the profiles in air in (b) is stretched by the refractive index of borosilicate glass ($n = 1.46$) to mimic propagation in glass. Numerical simulation results corresponding to the lowest and highest pulse energy are shown in Fig. 4.13 for both pulse durations respectively. Note the increase in length with pulse energy, the much more confined and pronounced modification for longer pulse durations and the preferential energy deposition before the focus. The interruptions in (b) are attributed to the recording process rather than the propagation itself.

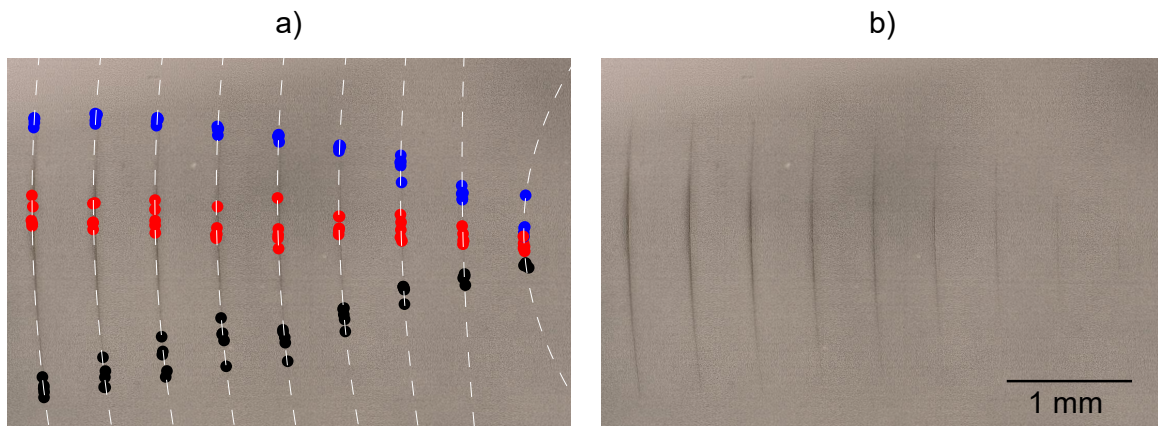


FIGURE 4.3: Manual measurements (a) of the Airy modifications with $f = 20$ mm, $t_p = 10$ ps and decreasing pulse energy from the left starting at $380 \mu\text{J}$ and decreasing in steps of $38 \mu\text{J}$. The fits yield $r = (11.6 \pm 1.8)$ mm and lengths that are used for the estimation of the threshold intensity in Fig. 4.5 and the determination of the effective electron collision time, see appendix C.

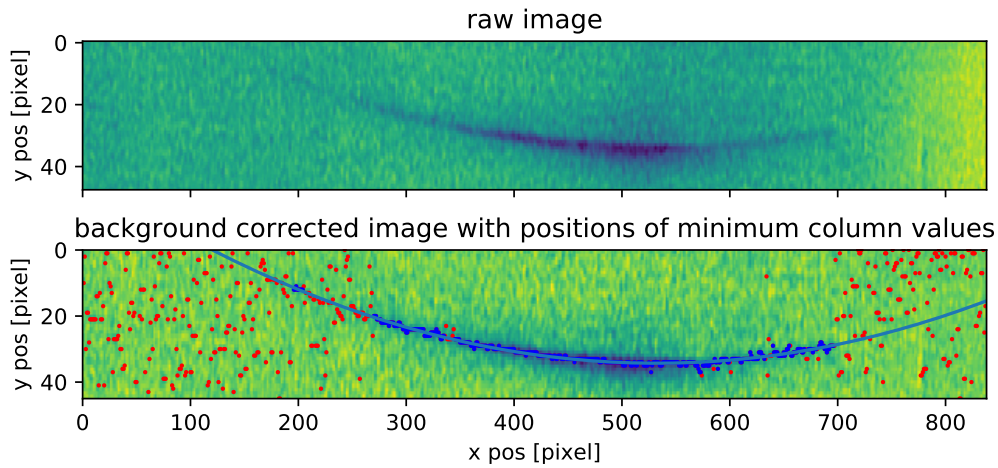


FIGURE 4.4: Example of automated image analysis for characterization of the volume modifications. Note that also interrupted modifications can be detected. Also see appendix B.

Modelling the increase of the modification length in terms of a constant threshold intensity I_{th} applied to the linear propagation, yields $I_{\text{th}} = (8 \pm 3) \times 10^{13} \text{ W/cm}^2$ for $f = 20 \text{ mm}$, see Fig. 4.5. The uncertainty is given as the half width at twice the minimum value of the root mean squared deviation between simulated and measured length. The same approach applied to the modifications written with $f = 10 \text{ mm}$ gives $I_{\text{th}} = (4.6 \pm 1.2) \times 10^{13} \text{ W/cm}^2$, see Fig. 4.6. The fitted bending radius $r = (1.5 \pm 0.4) \text{ mm}$ for $f = 10 \text{ mm}$ is in excellent agreement with the theoretically expected value, see Tab. 3.1. For the image analysis at tight focusing conditions, the modifications written with short pulses ($t_p = 1 \text{ ps}$) were used, as they provided the clearest profiles. Extensive damage was observed for the longer pulse duration with lateral diameters of $20 \mu\text{m}$ and significant birefringence, see Fig. 4.7. An influence of the pitch on the extent of damage can also be seen in this image, indicating overlapping interaction zones for neighbouring modifications.

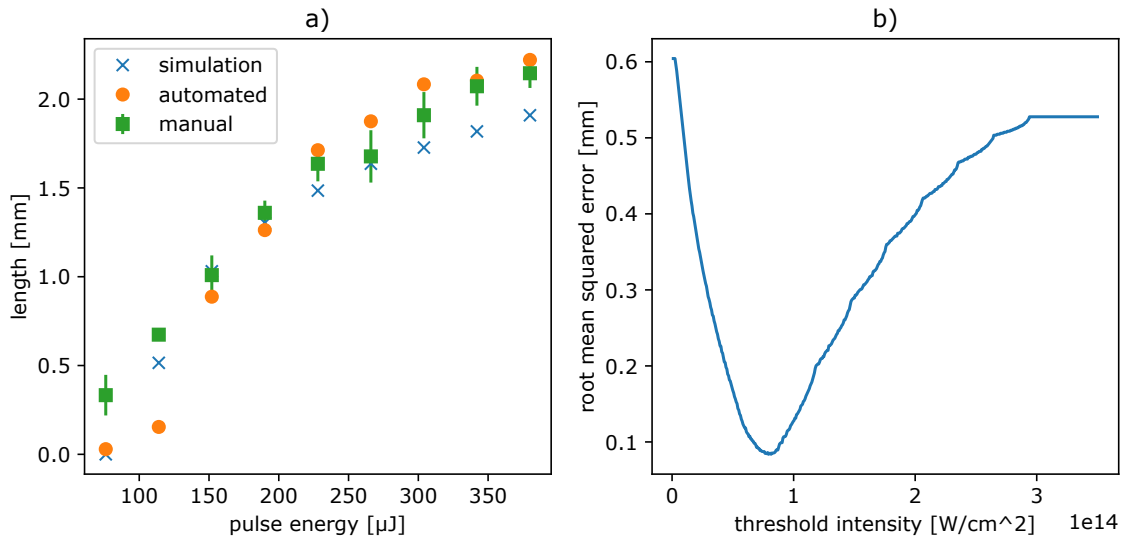


FIGURE 4.5: Length scaling of the Airy Beam for $f = 20 \text{ mm}$ (a), and root mean squared deviation (RMSD) from fitting a constant intensity threshold of the linear propagation to the automated data (b). The minimum RMSD is reached at $I_{\text{th}} = (8 \pm 3) \times 10^{13} \text{ W/cm}^2$. $I_{\text{th}} = (7.0 \pm 1.8) \times 10^{13} \text{ W/cm}^2$, if the manual data is fitted.

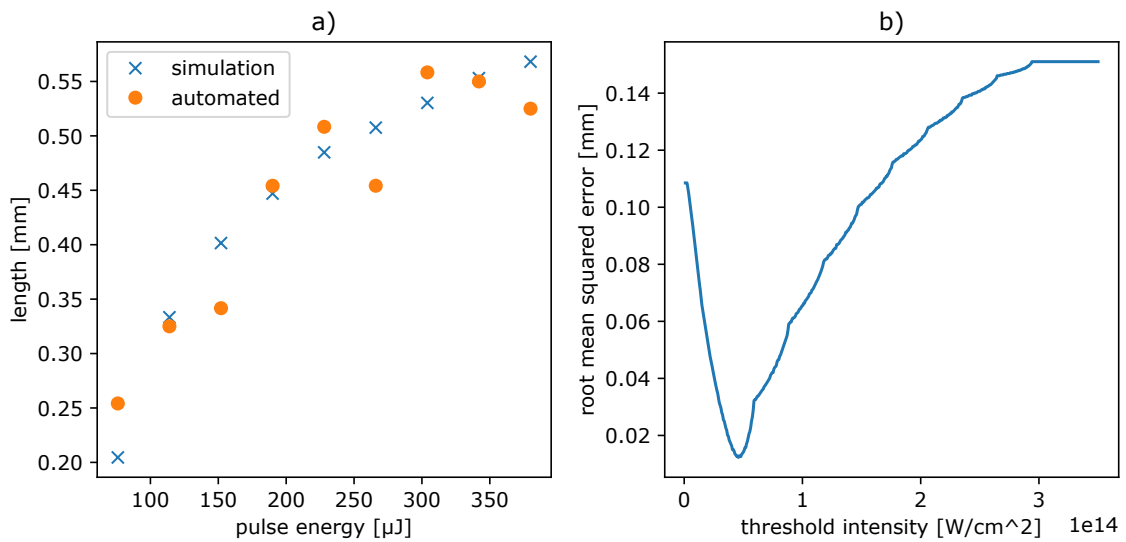


FIGURE 4.6: Length scaling of the Airy Beam for $f = 10 \text{ mm}$, analogous to Fig. 4.5, yielding $I_{\text{th}} = (4.6 \pm 1.2) \times 10^{13} \text{ W/cm}^2$

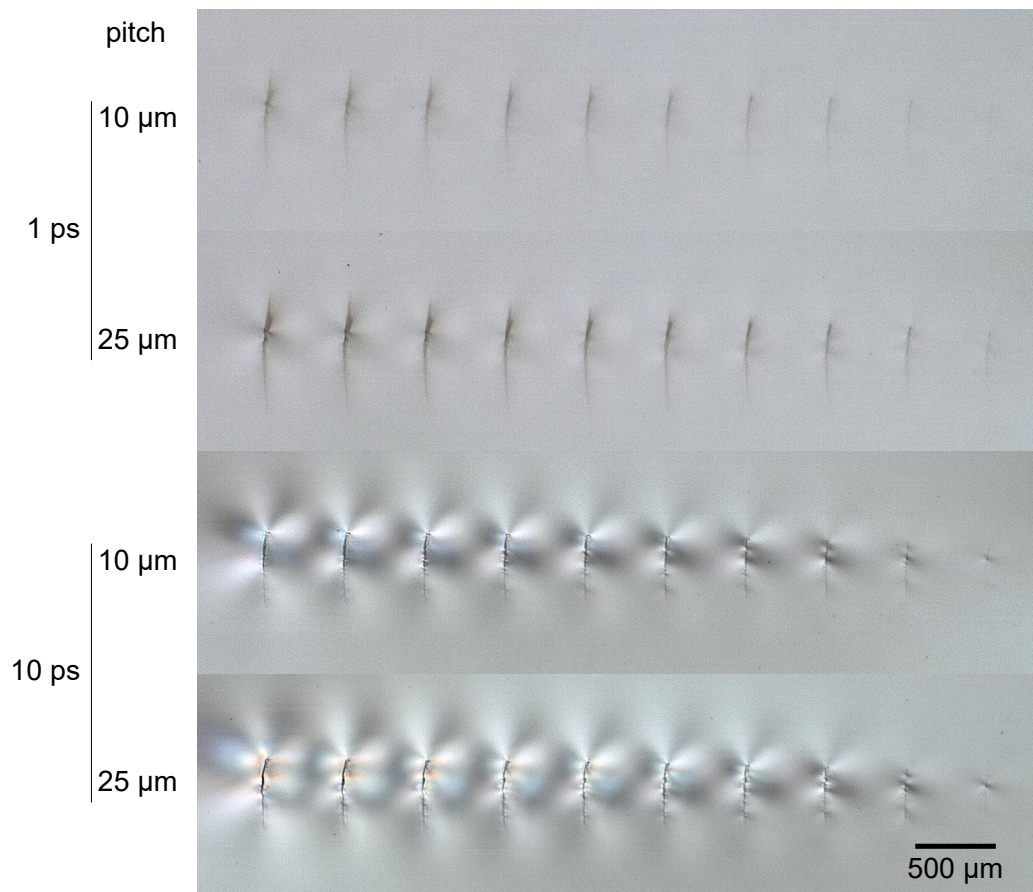


FIGURE 4.7: Microscope cross section of volume modifications for $f = 10$ mm, two values of the pulse duration and pitch p respectively and varying pulse energy, as in Fig. 4.3, from the left starting at $380 \mu\text{J}$ and decreasing in steps of $38 \mu\text{J}$.

4.3 Cracks, surface effects and etching behaviour

In the previous section only bulk modifications were considered and surface modifications were avoided by placing the focus deep within the sample. For micro perforation, however, also the surface damage needs to be taken into account as well as the formation of cracks.

To study the relationship between surface and volume modifications for the Airy beam in more detail, I chose a focus position closer to the surface of the sample ($\Delta z = 200 \mu\text{m}$) and observed the resulting modifications with both reflected and transmitted light microscopy (Zeiss Axio Imager).

The formation of cracks is best observed in transversal section and for isolated modifications. Fig. 4.8 shows that at a low pulse energy the modifications are elongated in the direction perpendicular to the mirror plane of the Airy beam, i.e. in the intended cutting direction. Towards the ends of the volume modification this lateral elongation decreases. Larger cracks form for a burst mode with the same peak intensity and even tend to bend away from the Airy side lobes. As the energy is increased, on the other hand, the modifications extend along direction of the side lobes up to several tens of μm , see Fig. 4.9.

The relative scaling of surface and volume damage is shown in Fig. 4.9 for various pulse configurations with varying peak intensity and constant fluence. There is no visible volume damage for the shortest pulse duration, associated with the highest intensity. Confined damage can be seen for single longer pulses, but the volume immediately beneath the surface tends to be much weaker compared to the damage at the surface and in volume. The burst mode with 2 pulses and $t_p = 5 \text{ ps}$, as shown before in Fig. 4.8 leads to a strong mechanical damage within the volume, even close to the surface. Modifications written with 4 pulse bursts are associated with larger cracks in poorly defined directions.

Using light microscopy to identify the onset of surface ablation in the main lobe and largest three side lobes of the Airy beam for different pulse energies and focus positions, I determined the surface damage threshold intensity for Borofloat[®] 33 as $(1.07 \pm 0.12) \text{ TW}/\text{cm}^2$ for $t_p = 10 \text{ ps}$ for single laser pulses.

Going towards separation tests, I examined top and bottom surface modifications for various combinations of pulse duration, burst mode, pulse energy, focus position, pitch and glass sheet thickness. In a first step the modifications at top and bottom were inspected right after the laser process. In a further step, the glass sheets were etched with potassium hydroxide for a short time, equivalent to $10 \mu\text{m}$ removal at each side of the pristine sheet ("etch radius"). The etching step helps to show weak modifications that would not be visible with the light microscope, see Fig. 4.10. In the ideal case, surface modifications would be identical in extent and lateral position, indicating a setting with both good penetration and a symmetric position within the glass sheet. For symmetric beam positioning, however, the bottom modification was suppressed if at all visible for single pulses. For laser bursts, the bottom modification was stronger, compare S1 and S2 in Fig. 4.10.

As one can also see in Fig. 4.10, the overlap of neighbouring modifications experiences a larger etching rate than the main lobe modification for single long pulses. Burst mode operation, here shown with four pulses in a burst (S2), leads to more localized, enhanced etching.

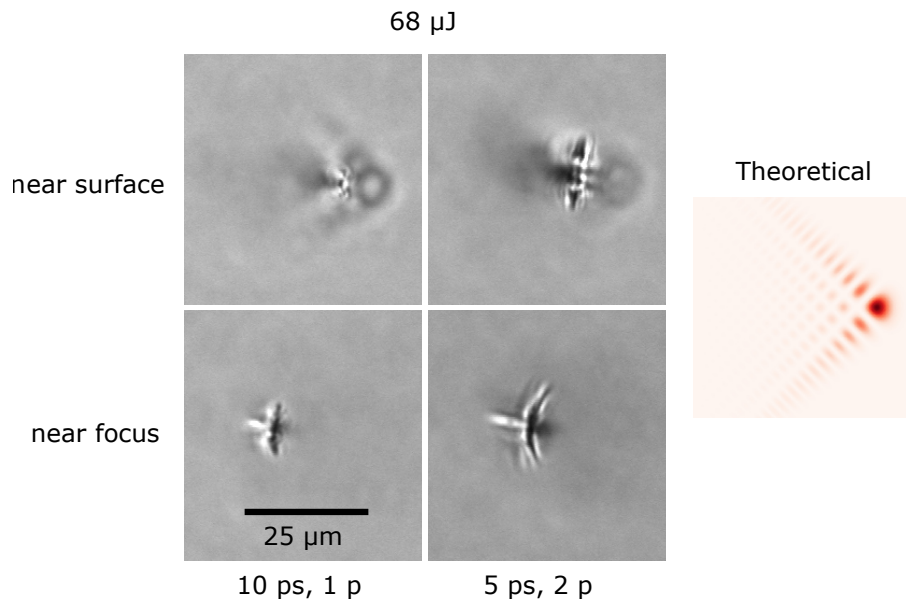


FIGURE 4.8: Light microscopy top view of volume modifications for $f = 10$ mm.

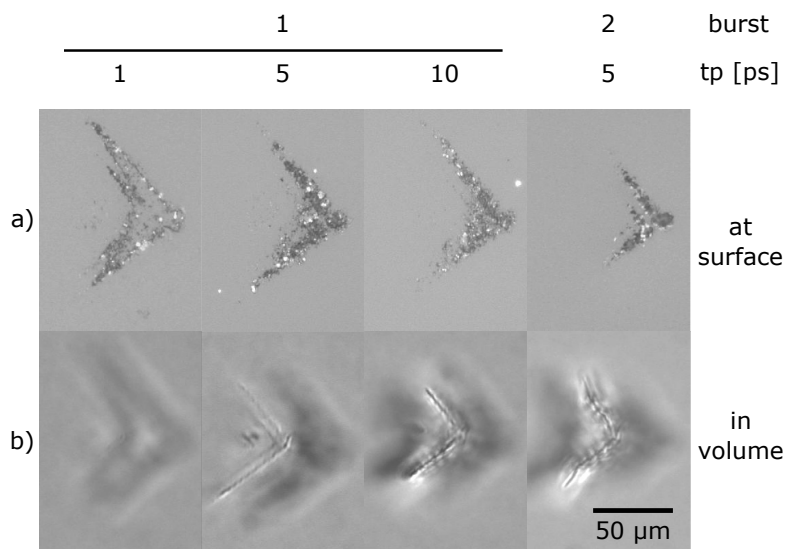


FIGURE 4.9: Light microscopy top views of permanent modifications (a) at the surface and (b) at a depth of $60 \mu\text{m}$ within the volume of the glass with focal length $f = 10$ mm, burst energy $E_{\text{burst}} = 204 \mu\text{J}$ and focus position $\Delta z = 200 \mu\text{m}$ for varying pulse duration t_p and burst configuration. Both reflected (a) and transmitted (b) light microscopy were used for optimal contrast, still the blurred imaged of the surface modification can be seen in (b).

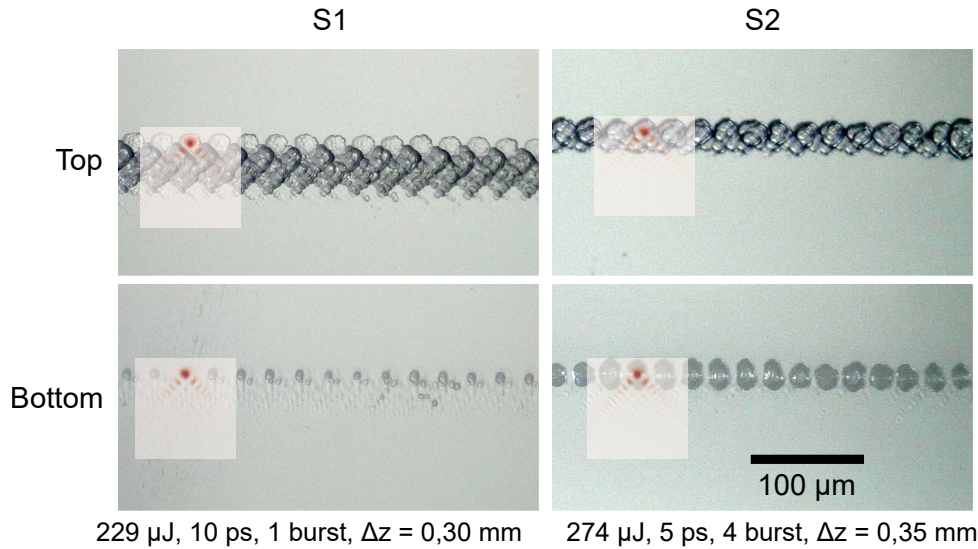


FIGURE 4.10: Surface modifications at top and bottom of a 1 mm thick sheet of borosilicate glass for two sets of processing parameters as given in the columns respectively with $f = 20$ mm. The corresponding intensity profile is shown for comparison. Note the preferred etching of the overlapping zones of side lobes for S1 and the stronger modification at the bottom surface for S2. An effect of etching could also be seen at the centre of the sheet for S2, but not for S1.

4.4 Separation results

For the separation experiments I used glass of $525 \mu\text{m}$ thickness, allowing perforation with $f = 10$ mm. The glass pieces were subsequently separated, if possible, either by mechanical breaking (cleaving) or etching with potassium hydroxide. The resulting profile was recorded using confocal light microscopy in addition to the cross section analysis. Although it was possible to cleave the glass along a line perforated with the Airy beam, the new surface, as shown in Fig. 4.11, follows only partially the perforations created by the laser process: Often the crack "cuts short" and runs trough the convex side, building up as concoidally fractured bits within the concave side of the intended cut. The process then rather resembles laser scribing [NLS13] rather than proper full volume cutting.

In contrast, Fig. 4.12 shows the fully expressed convex side obtained after separation by etching after laser processing with an Airy beam with $f = 10$ mm, using a burst of two pulses with each a width of $t_p = 5$ ps and an energy of $E_{\text{burst}} = 228 \mu\text{J}$, perforating with a pitch of $10 \mu\text{m}$. The convex profile follows a parabola with an effective bending radius $r_{\text{eff}} = (774 \pm 2) \mu\text{m}^2$, which is smaller than the radius of the Airy main lobe trajectory ($r = 1.5$ mm). This stronger curvature and the large top angle $\alpha_{\text{max}} = 18^\circ$ can be understood as an extra taper angle resulting from the etching process adding to the curved Airy profile. Due to the preferential absorption in the upper part of the glass sheet, see Sec. 4.2 and also Sec. 4.5, I had to choose a focus position below the centre of the glass sheet ($\Delta z \approx 220 \mu\text{m}$) in order to be able to perforate the glass sheet completely. The side view in Fig. 4.12 c) corroborates a more extensive damage in the upper part of the glass sheet and a weaker damage in the lower part, as the edge surface below the focus shows a coarser structure. This coarser structure can be explained by a more localized etching process due to less extensive (and more variable) laser damage.

The opposite side of the cut (not shown here) does not exhibit the expected concave profile. Instead, more material is removed on the upper side of the glass sheet, thus resulting in a nearly planar, inclined edge. This finding can be understood in terms of an increased removal rate during etching

²The error is given in terms of the error of the quadratic fit. The real error will be higher due to the error in error in the confocal profile measurement.

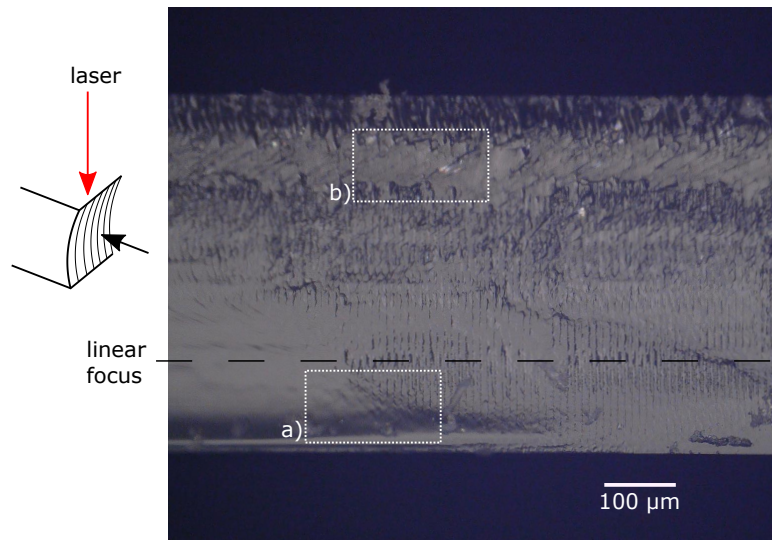


FIGURE 4.11: Side view onto concave side of a glass sheet cleaved mechanically after laser perforation with $E_{\text{burst}} = 428 \mu\text{J}$ from the top as shown on the left. Note that while the laser modifications penetrate the whole thickness of the sheet, large parts are fractured concoidally, leaving glass superimposed on the surface of modifications (a). This means that neither the concave nor the convex side of the cut have a well defined profile. A zone towards the surface shows hardly any laser modification (b). This is interpreted as the shadow of the plasma ignited at the surface during the laser process.

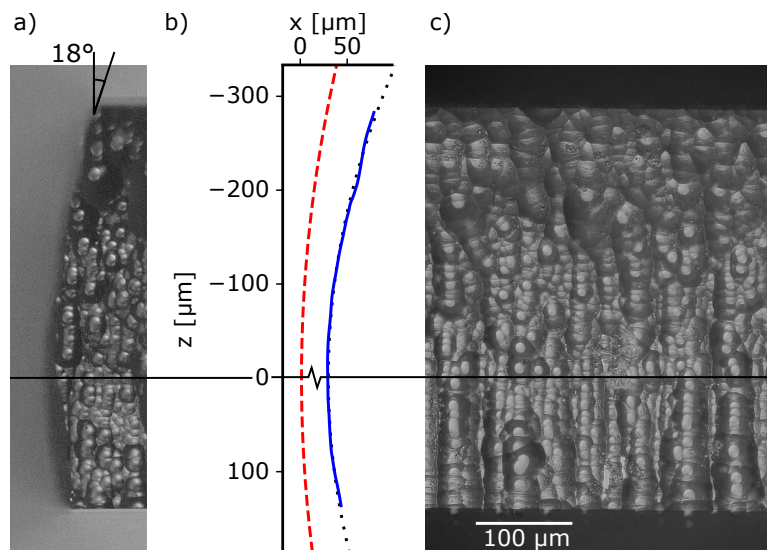


FIGURE 4.12: Result of cutting a $525 \mu\text{m}$ thick glass sheet by perforation with an Airy beam and subsequent etching ($50 \mu\text{m}$ etch radius). A cross section view (a) parallel to the line of laser modifications shows the curved profile of the cut. The average height profile (b) measured by confocal light microscopy (solid blue) and its parabolic fit (dotted black) exhibit a considerably stronger curvature than the Airy profile (dashed red), which can be attributed to the etching process. The side view onto the convex side (c) shows a coarser structure at the bottom, probably due to less extensive damage leading to more localized etching.

in the glass volume modified by interactions with the Airy side lobes in addition to the previously mentioned taper angle.

4.5 Energy deposition during non linear Airy propagation

Simulation of the energy deposition by using an unidirectional pulse propagation model accounting for all relevant non linear propagation effects, in particular the laser-generated conduction electrons [Ber+08; DC+15], also see Sec. 2.4.2, help to understand the observed material damage [STS21c].

Considering the result of the numerical simulations, that are shown in Fig. 4.13, we first note that while the total energy deposition is larger for short pulses with $t_p = 1$ ps respectively, the energy density is much higher for the longer pulses with $t_p = 10$ ps for all pulse energies considered. This is also in agreement with previous observations obtained by pump-probe experiments [Mau+16] with Gaussian focusing. For the short pulses the laser affected zone is much broader. This can be attributed to an effect termed intensity clamping [Liu+02; SS+16], also see Sec. 2.4.4. The result is a high overall absorption, see Fig. 4.14, but a lower energy confinement. This corroborates the experimental observation of more confined and stronger modifications for the 10 ps-pulses in Fig. 4.2 c).

Also the preferential energy deposition in front of the focus observed in the experiments is well captured by the simulations, and can be explained by non linear absorption due to plasma generation in the side lobes of the Airy beam, which is clearly visible for the high energy cases for both pulse durations shown in Fig. 4.13.

Another non linear effect that could potentially cause a shift towards the laser source is the optical Kerr effect, also see Sec. 2.4.3. The peak intensities of the pulse configurations shown in Fig. 4.2 range from $3 P_{cr}$ (using Eq. 2.12 and $\alpha = 3.79$) to $177 P_{cr}$, so that self focussing could generally be expected to be relevant. We performed simulations without the term for self focusing for the four cases shown in Fig. 4.2 d) to test the influence of the Kerr effect on the propagation and the resulting energy density distribution. A direct comparison as shown in Fig. 4.15 indicates that the Kerr effect causes only a slightly increased energy deposition and confinement for the long pulse duration, but the effect is small compared to the non linear propagation effects that arise from the plasma dynamics. This is plausible, because the hard focusing conditions lead to phase curvatures that are large compared those caused by the changes in the refractive index, even for optical powers larger than P_{cr} . The asymmetry and shift towards the laser source in the distribution of deposited energy along the propagation are practically exclusively caused by plasma effects.

Overall, the observations of the volume modifications and the non linear simulations indicates that longer pulses are favourable for cutting applications. As the pulse duration in simulations is increased beyond the range used in experiments, the maximum energy density even continues to increase in an increasingly confined volume, see Fig. 4.16. This indicates that for pure volume modifications longer pulse durations could be favourable. However, an important limitation of the numerical model is that the diffusion of the free electrons is not taken into account. Especially considering that the gradients in electron density increase significantly and the line energy, i.e. the total amount of deposited energy, decreases, plasma diffusion will limit the maximum energy densities that can actually be reached.

Another way to enhance the laser energy deposition in the bulk is to use the laser in burst mode operation [Mis+17], which we considered for the separation experiments, see Sec. 4.3 and Sec. 4.4.

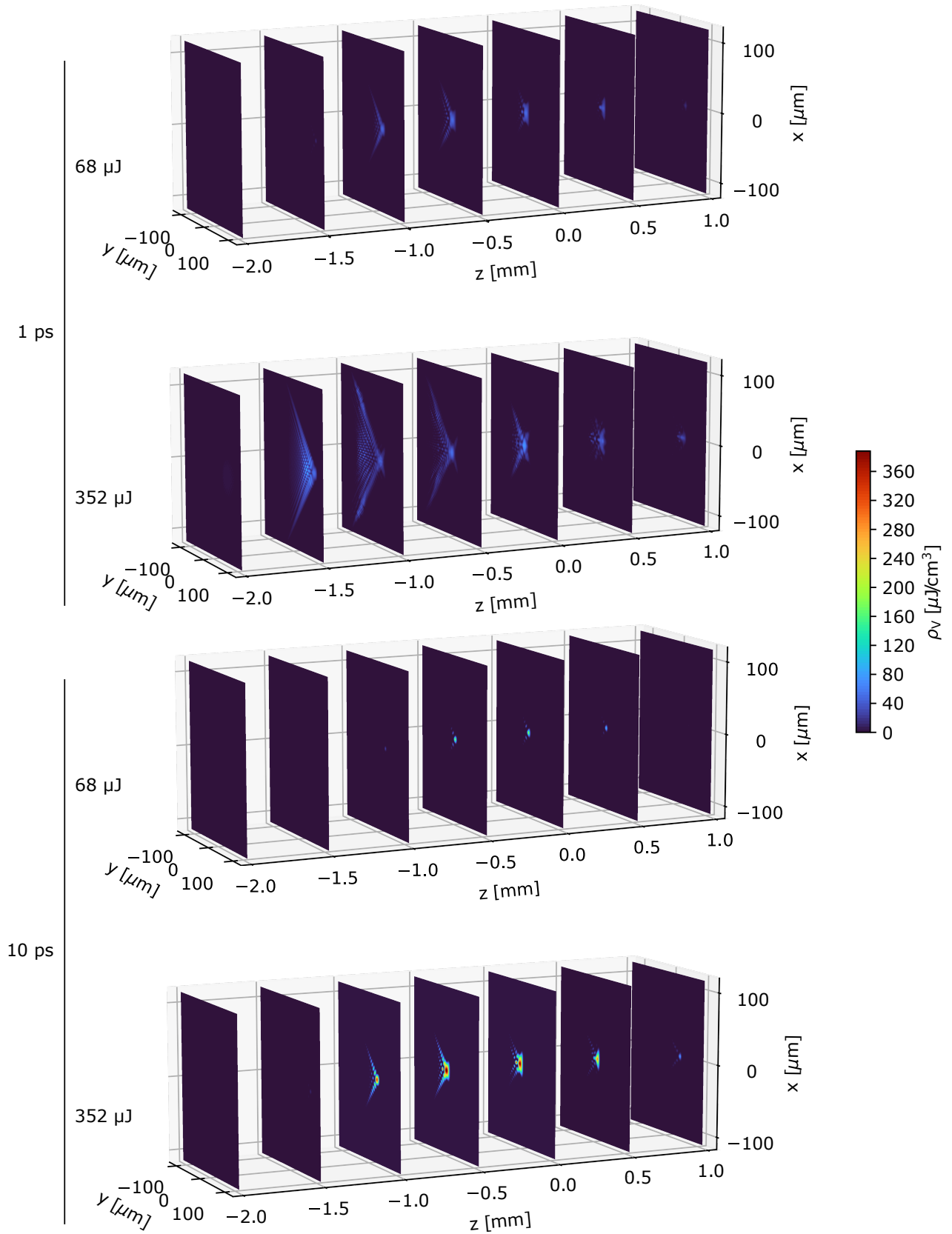


FIGURE 4.13: Transversal sections of the volume density of deposited energy ρ_V for pulsed Airy beams with the same pulse configurations as in Fig. 4.14. The sections at the linear focus position $z = 0$ correspond to those shown in Fig. 4.2. Courtesy of Stefan Skupin.

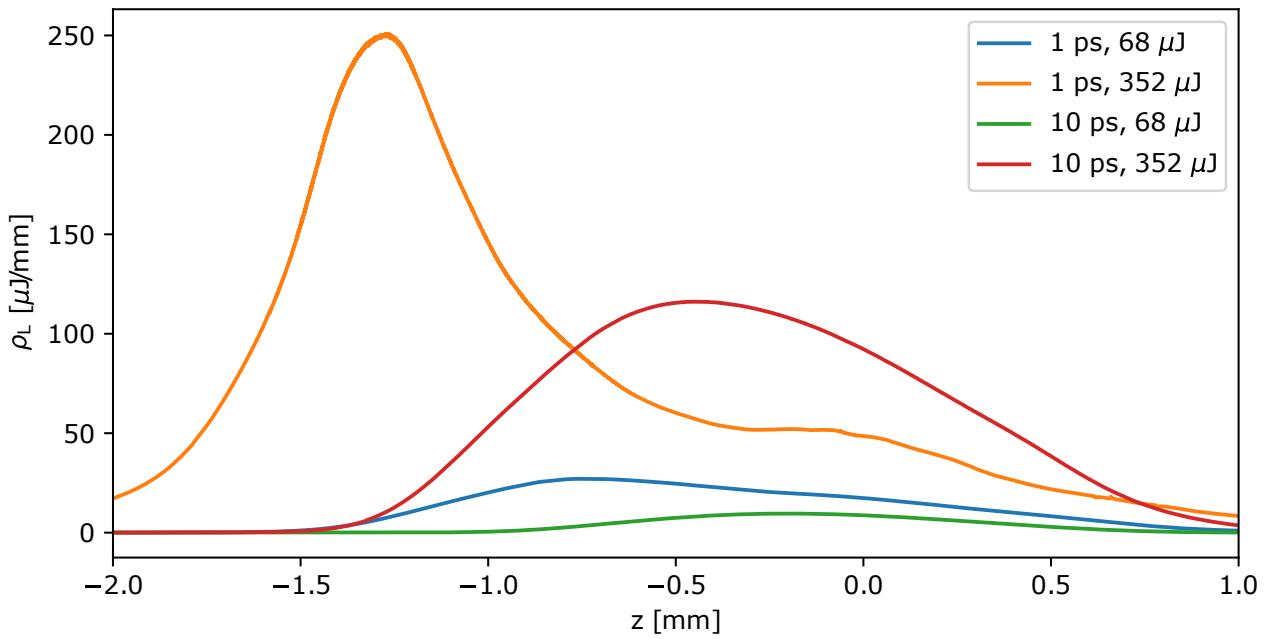


FIGURE 4.14: Line density of deposited energy ρ_L for the two pulse durations and the two pulse energies shown in Fig. 4.2. Note the shift of the distribution towards the laser source with respect to the linear focus position at $z = 0$ with increasing pulse power.

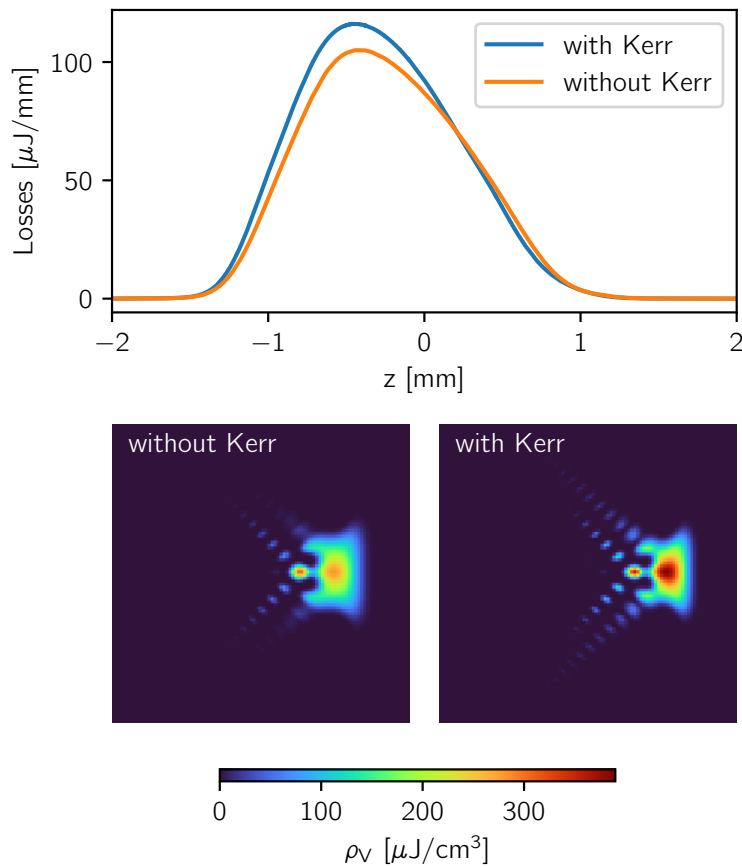


FIGURE 4.15: Simulated line and volume energy densities with and without Kerr term. Courtesy of Stefan Skupin.

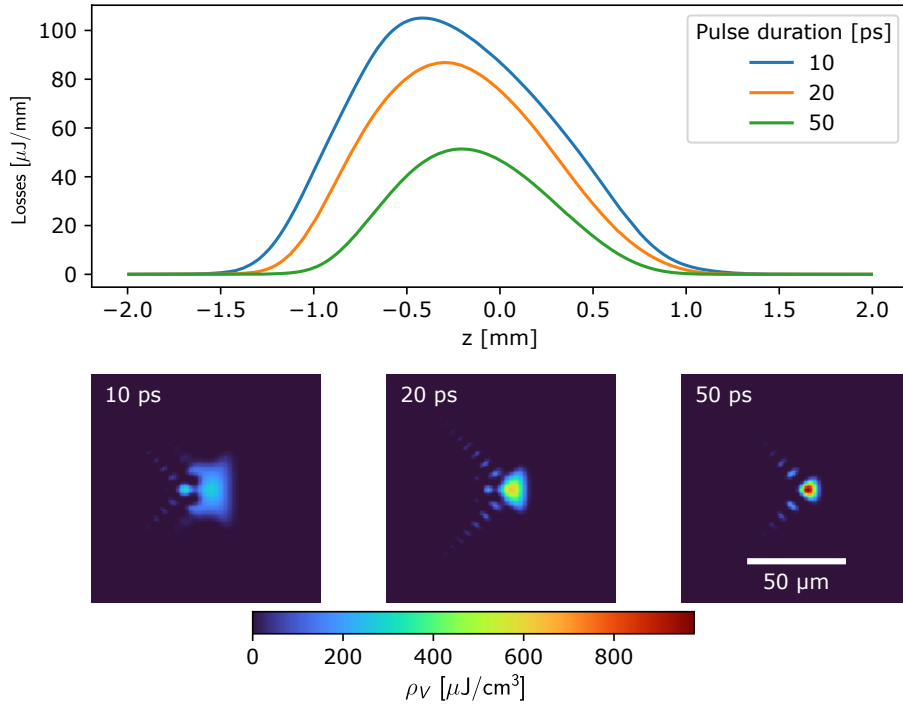


FIGURE 4.16: Simulated line and volume energy densities for longer pulse durations for $E_p = 352$ J. The 10 ps case is also shown in Fig. 4.15 (with Kerr), but drawn with different scaling.

4.6 Discussion

The observation of a higher modelled linear intensity threshold for the larger focal length as shown in Fig. 4.5 in comparison to Fig. 4.6 can be explained in terms of distributed plasma shielding: In tighter focussing conditions, the plasma only effectively defocuses the beam when higher electron densities are reached, which in turn can cause an earlier onset of visible material damage. This is in line with the previous observation of the collapsing modification of the spherical lens, as shown in Fig. 2.16, where the upper part of the modification is formed from higher angle cones, and also for simulations and cutting experiments with Bessel beams with various cone angles [Mis+17].

While the Bessel beam in that study has a focal contrast of about 5 the 2D Airy used here has a focal contrast of about 2. In previous Airy beam micro machining studies this was not an issue, because the side lobes were propagating in air [Mat+12] or lead to an opening of a wider trench [Mat+13a]. When focusing within the glass volume, however, this low focal contrast strongly limits the useable length of the Airy beam and renders the balance between surface and volume damage an important factor. The surface damage threshold of (1.07 ± 0.12) TW/cm² for $t_p = 10$ ps obtained here is similar to previous values for borosilicate glass [Nie+15] and significantly lower than the smallest modelled intensity threshold in volume $((4.6 \pm 1.2) \times 10^{13}$ W/cm²).

The pulse durations in this work lie in the intermediate range where the scaling of the surface damage threshold changes from a more intensity dominated regime for short pulse durations to a more fluence dominated regime for long pulse durations [Stu+96]. It may well be that a different scaling with intensity or fluence between surface and volume damage is the main reason for the observed optimum at intermediate pulse durations and burst.

In particular, avalanche ionization is dominant compared to photo ionization for longer pulses, which leads to a process that is less deterministic and more dependent on material defects. Although previous studies, that report on this transition have looked at much shorter pulse durations [San+10], the difference due to the higher initial free electron density at the surface and at defects will lead to a different scaling behaviour between surface and bulk.

The increased etching rate observed in overlapping region of the side lobes as shown in Fig. 4.10 can also be explained in terms of enhanced avalanche ionization at defects for long pulses.

Microscope inspection indicates that also large numbers of pulses in the burst are not favourable for the process, due to excessive crack formation in the side lobes of the beam. While the dependence of avalanche ionization on pre-existing defects puts a limit on the pulse duration, the same physical process seems to be responsible for an optimum at intermediate pulse numbers. Again, the low focal contrast exacerbates this effect, as volumes that should not be damaged are exposed to relatively high intensities. In the case of separation by mechanical cleaving this can deviate the crack away from the intended cutting line, during etching this can mean that the curvature of the resulting edge is reduced.

4.7 Summary

Volume modifications written with the Airy beam in borosilicate glass follow the theoretically expected curvature up to lengths of more than 2 mm. A range of observations can be attributed to the plasma ignition in the side lobes:

- The asymmetry of the modifications increases with increasing pulse energy, tilting the modification by increasing the upper and suppressing the lower part.
- A more confined damage and higher energy density is observed for longer pulses, the strong absorption for short pulses at 1 ps is broadly distributed and does not lead to visible mechanical damage.
- The modeled linear damage intensity threshold is higher for the longer focal length ($(8 \pm 3) \times 10^{13} \text{ W/cm}^2$ vs. $(4.6 \pm 1.2) \times 10^{13} \text{ W/cm}^2$ for the short focal length).
- The volume damage just beneath the surface is suppressed and a shadow zone is observed beneath the surface in mechanically cleaved samples.

The focal contrast is therefore a crucial limiting factor for the application of the Airy beam in glass cutting.

Longer pulses lead to a more confined volume damage, but tend to increase the shadowing effect of the surface. The energy deposition can be enhanced and the amount of volume damage increased by the use of a burst mode at constant intensity and fluence. A balance for sufficient, but not excessive damage has been found at a pulse duration of 5 ps in a 2 pulse burst.

An edge with a parabolic trajectory with an effective bending radius $r_{\text{eff}} = 774 \mu\text{m}$ has been produced in a $525 \mu\text{m}$ thick glass sheet by the use of Airy beam micro perforation in combination with etching. To achieve a sufficient damage throughout the sheet the focus had to be placed beneath the centre of the glass sheet, thus resulting in an asymmetric, effectively tilted edge.

Chapter 5

Improved glass cutting with a shifted Airy beam

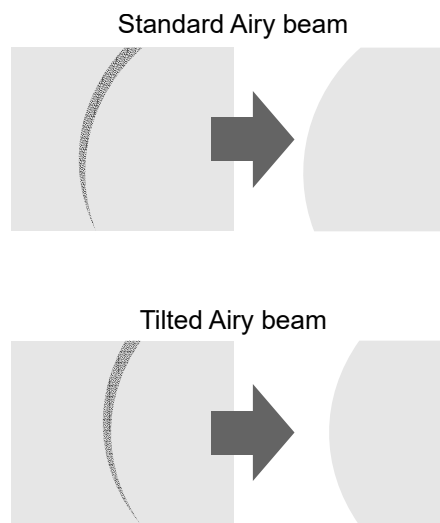


FIGURE 5.1: Schematic representation of processing idea for creating symmetric edge by compensating preferential energy deposition by using a tilted Airy beam.

The preferential energy deposition of the Airy (see Sec. 4.2) that leads to an asymmetric expression of the edge can be compensated by adding a relative tilt between the Airy beam and the work piece, for example by tilting the Airy beam, as shown in Fig. 5.1. This tilt could potentially be achieved by tilting the optical setup or the work piece itself. The Airy beam, however, offers a convenient method for adding the required tilt on the focal line by what has previously been called “ballistic control” [Hu+12]. Hu et al. consider as two degrees of freedom for this control the transversal translation of the Gaussian input beam and the phase mask. The offset of the Gaussian beam input beam shifts the focal intensity distribution along the parabolic trajectory of the Airy beam, see [Hu+12] and Fig. 5.2. Aiming to quantify the amount of tilt that we can expect and to understand the key parameters for this tilt, the effect of an offset on the $2f$ setup is examined in the next section before moving on to the application of the shifted beam in micro machining.

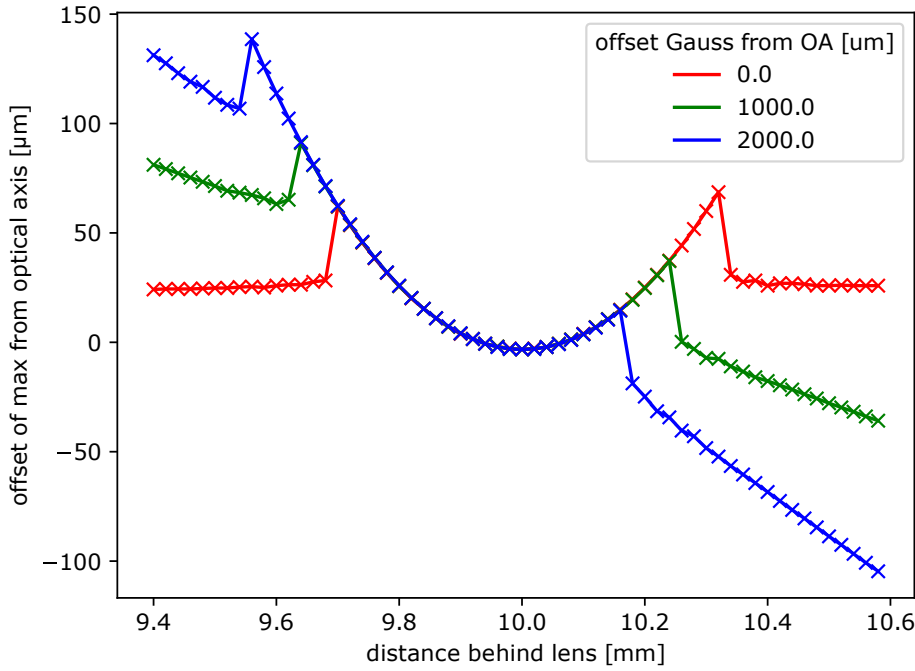


FIGURE 5.2: Simulated main lobe trajectory for different offset of the Gaussian input beam from the optical axis for a lens with $f = 10$ mm. Note that the the parabolic trajectory is limited due to the diffraction of the beam and that the Gaussian beam further away from the focal plane propagates along a linear trajectory, also see Fig. 3.4 b). Numerical simulations were performed in 1D with a FFT propagator as introduced in Sec. 3.2.3.

5.1 Paraxial analysis of offset

Moving a finite beam on an optical element is equivalent to changing to a shifted coordinate system with respect to the optical phase that is imprinted on the beam by the optical element. Let us consider the aberrations that arise in this new coordinate system for a 2D cubic phase mask.

Expanding the 2D cubic phase

$$\phi(x, y) = \frac{\beta^3}{\sqrt{2}} \left(\frac{x^3}{3} + xy^2 \right) \quad \text{with} \quad r^2 = x^2 + y^2 \quad (5.1)$$

for a shifted coordinate system $x = x' + x_{\text{off}}$, i.e. an offset along its symmetry plane, yields

$$\phi(x' + x_{\text{off}}, y) = \phi(x', y) + x' \frac{\beta^3 x_{\text{off}}^2}{\sqrt{2}} + r^2 \frac{x_{\text{off}} \beta}{\sqrt{2}} \quad (5.2)$$

where phase contributions that are constant over the (x', y) plane have been dropped. The linear phase term induces a tilt of

$$\theta = \beta^3 x_{\text{off}}^2 / (\sqrt{2}k) \quad (5.3)$$

behind the phase mask. This is negligible compared to the tilt $\theta_{tl} = x_{\text{off}}/f$ that arises from the same offset on an ideal thin parabolic lens with focal length f when

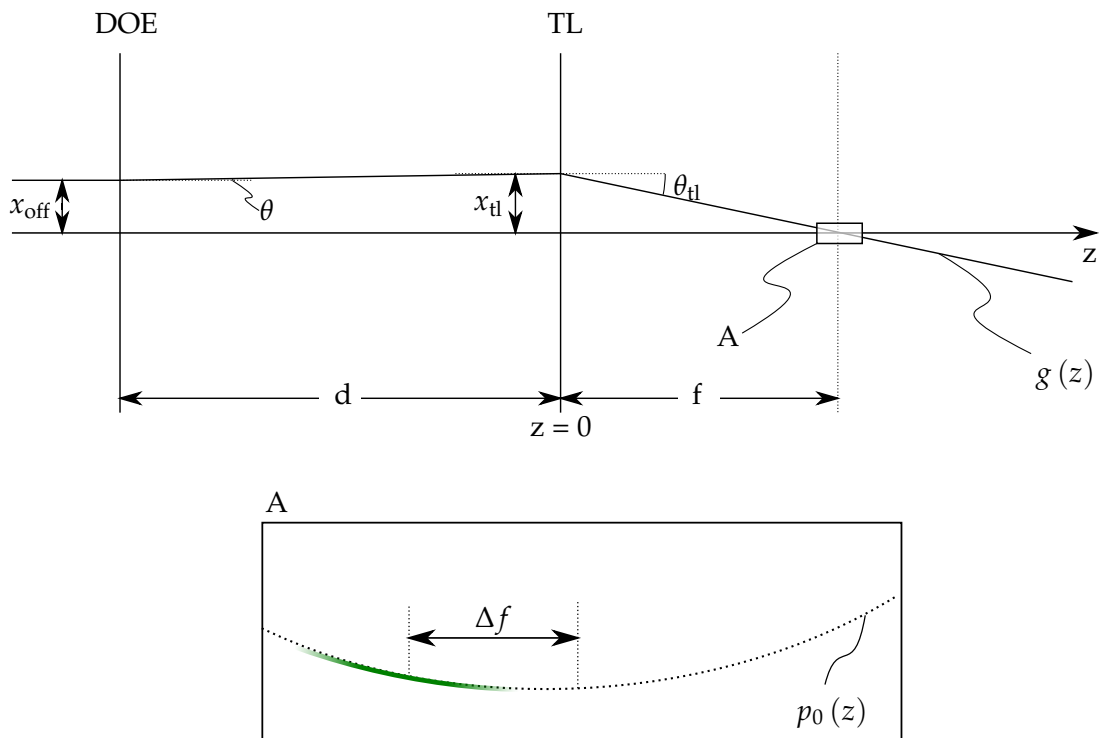


FIGURE 5.3: Schematic optical setup with ray trace that represents the center of mass (CoM) of the Airy beam. The enlarged focus region A shows schematically the positioning of Airy focal line that is defined by the main lobe of the focal intensity distribution and which is shifted along the propagation by the extra quadratic term induced by the offset on the cubic phase mask.

$$x_{\text{off}} \ll \sqrt{2k}/(f\beta^3), \quad (5.4)$$

i.e. for $x_{\text{off}} \ll 28$ cm with $\lambda = 1030$ nm, $f = 10$ mm and $\beta = 3^{1/3}\text{mm}^{-1}$, which is always fulfilled for the optical setups used here.

The r^2 term in Eq. 5.2 leads to defocussing by the phase mask with an effective focal length

$$f_1 = k/(x_{\text{off}}\beta^3\sqrt{2}). \quad (5.5)$$

Simple geometrical combination of the focal powers of phase mask and microscope objective, as introduced in Eq. 3.14, yields a new focal length

$$f' = \left(\frac{1}{f} + \frac{x_{\text{off}}\beta^3\sqrt{2}}{k} \right)^{-1} \approx f \left(1 + \frac{fx_{\text{off}}\beta^3\sqrt{2}}{k} \right) \quad (5.6)$$

which gives a focal shift

$$\Delta f = f' - f \approx \frac{f^2 x_{\text{off}} \beta^3 \sqrt{2}}{k}. \quad (5.7)$$

I checked the validity of the geometrical combination of the two focussing optical elements with the formalism of Gaussian optics, see Eq. 3.15, and found that for the parameters in this work ($d = f$, $w_0 = 2.65$ mm) the results of geometrical and Gaussian optics agree very well and the defocus is indeed adequately described by Eq. 5.7. The slope of the original Airy parabola $p(z)$ as given in Eq. 3.39 at $z = \Delta f$ is

$$\left. \frac{dp}{dz} \right|_{z=\Delta f} = 2q\Delta f = \frac{x_{\text{off}}}{f}, \quad (5.8)$$

which indicates, that the new parabola within the paraxial conditions remains parallel to the original trajectory.

Importantly, for the offset along the 2D Airy symmetry plane there is no astigmatic focus term, meaning that as long as the focal length of the phase mask is weak compared to the microscope objective there is no significant change in the transverse scale x_0 of the focal intensity distribution. The intensity distribution will merely be translated and tilted and keep a constant morphology. An offset along the normal of the symmetry plane on the other hand leads to an astigmatic defocus, which results in different focal planes along the 1D Airy profiles, thus giving a 1D Airy focus that transforms to another, orthogonally oriented 1D Airy focus along the propagation, also see [Hu+12]. This is particularly relevant when the beam diameter is reduced in that dimension and generally should be avoided as it produces cracks that are at an angle to the intended cutting direction, see Sec. 6.1.

5.2 Micromachining methods and results

5.2.1 Optical setup and volume modifications

By tilting one mirror far in front of the setup used in the previous chapter, as shown in Fig. 5.4, a shifted version of the parabolic Airy focal line can be produced due to both tilt and defocus that result from the lateral offset on the optical elements.

The ablation patterns at the surface were used to determine the new focus position and to check the alignment of the offset direction with the phase mask, see Fig. 5.5. Also for the shifted Airy cases the ablation pattern with the largest extent generally occurs in the middle of the z -range in which modifications are visible, i.e. there is no significant distortion.

Fig. 5.6 shows the volume modifications for various values of x_{off} . Piezo electric adjusters were used

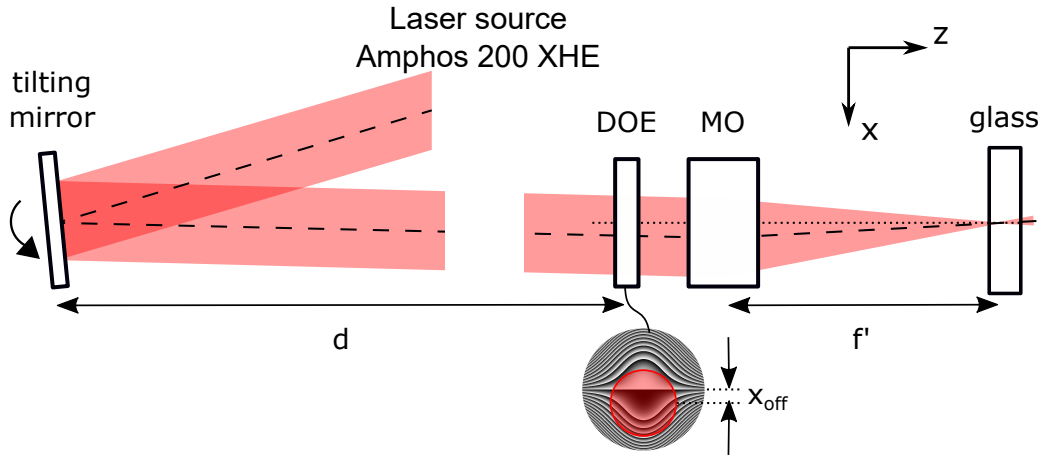


FIGURE 5.4: Optical setup from Fig. 4.1 with an additional degree of freedom to create a shifted Airy-Gauss beam. A small tilt early in the optical path ($d \approx 3$ m) effectively introduces a lateral offset x_{off} of the Gaussian input beam with respect to the diffractive optical element (DOE) and microscope objective (MO). Note that the offset beam is still centred on the mirror plane of the cubic phase mask.

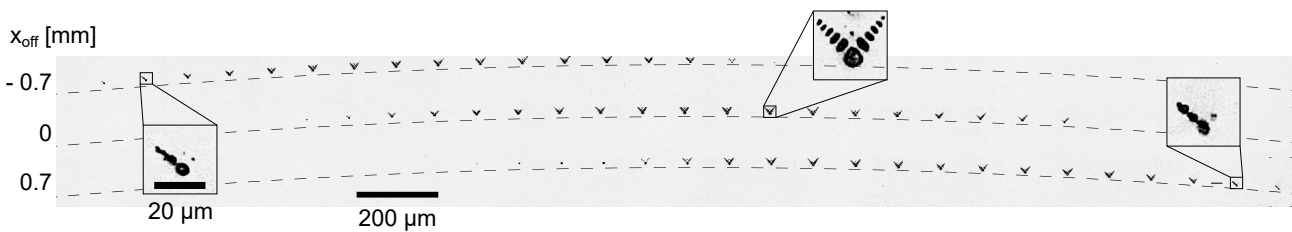


FIGURE 5.5: Surface modifications for three z-Scans with different values of x_{off} . The focus position Δz is changed in steps of $10 \mu\text{m}$ from left to right respectively, so that the intensity distribution of the Airy beam is sampled at different propagation distances, also see Fig. 4.1. The dashed lines show the same parabolic trajectory as guidance. A slight astigmatism can be seen for the shifted cases, as one Airy "leg" is longer at the far end of the propagation respectively.

for the active mirror, which resulted in low repeatability and a poorly defined initial state (Fig. 5.6 a), but additional recording of the beam position with an inline beam camera enabled an position accuracy ca. $\pm 10\%$ for all further data.

The defocus and tilt can clearly be seen and agree very well with the theoretically expected values, see Tab. 5.1. The length of the modifications remains nearly constant, as would be expected. However, we observe more evenly distributed damage for large x_{off} . This change in morphology can not be explained in terms of tilt and defocus, but can be reasonably be explained by spherical aberration, see Sec. 3.7.1 for more details.

5.2.2 Mechanical cleaving on a stepped roll

Using the tilt as additional degree of freedom, the modifications in glass sheets could be adjusted, so that at the same time the full thickness of the sheet was modified and the vertex of the modification was positioned at the centre of the glass sheet. For $300 \mu\text{m}$ thick sheets of BF33, mechanical separation could be achieved with a 2 pulse burst, a pulse duration $\tau_p = 5$ ps, a focal length $f = 10$ mm, a pitch $p = 15 \mu\text{m}$, a focus position $\Delta z = 100 \mu\text{m}$, and a burst energy $E_{\text{burst}} = 120 \mu\text{J}$. As before, however, the resulting edge did not show the expected curvature and a significant part of the edge fractured concoidally.

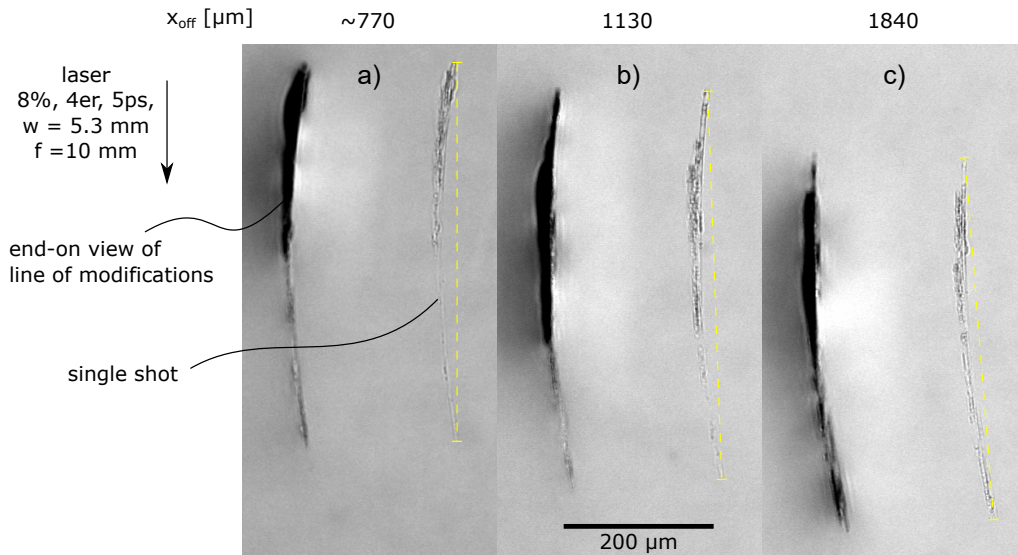


FIGURE 5.6: Longitudinal cross section of volume modifications for varying offset x_{off} of the Gaussian input beam on the cubic phase mask. The dashed yellow lines connect the measured endpoints of each modifications. Note that the value for x_{off} in a) is a rough estimate due to a poorly defined initial state. A 4 pulse burst is chosen (in contrast to the 2 pulse burst used for the separation experiments) to increase the visibility of the volume modifications in the light microscopy image.

	Defocus [μm]	Angle [$^\circ$]
Theoretical	72	2.8
Measured	71	2.5

TABLE 5.1: Relative defocus and angles of shifted Airy volume modifications shown in Fig. 5.6. The measurements are made using modifications b) and c) due to uncertainty in the x_{off} value for modification a). Relative error of theoretical values $\pm 10\%$ due to the limited accuracy of adjusting x_{off} .

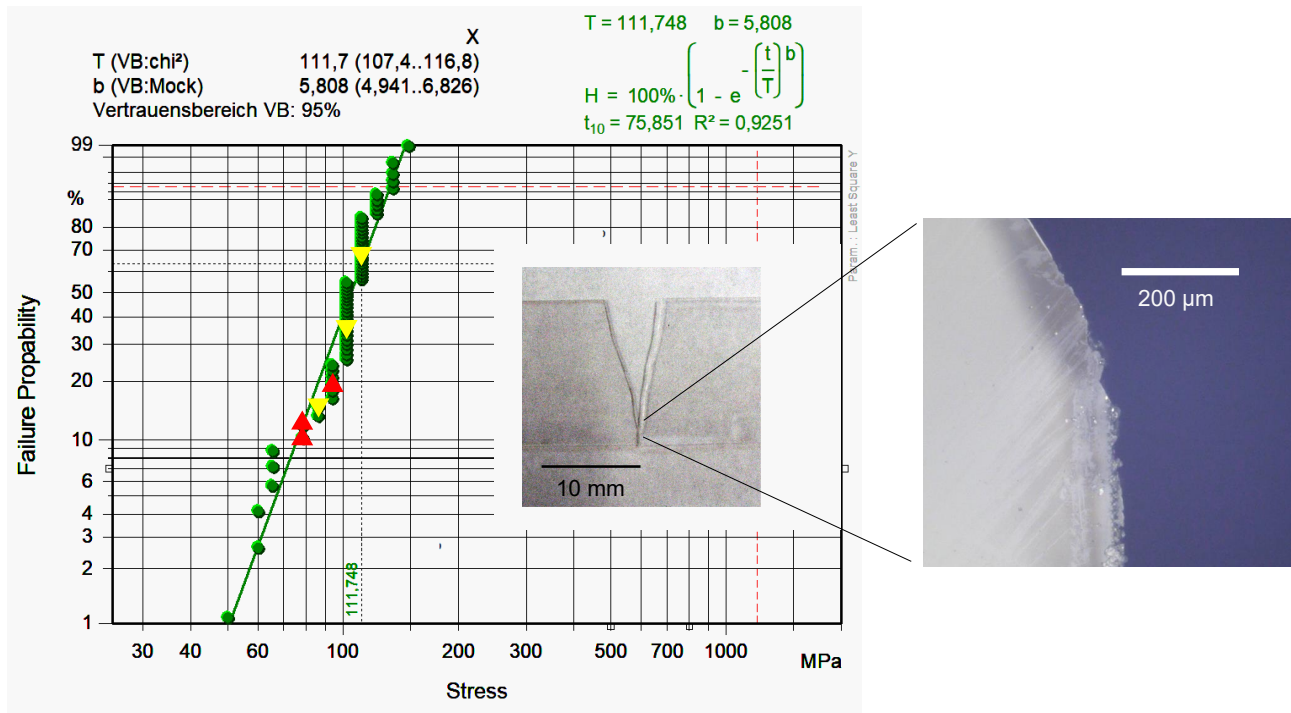


FIGURE 5.7: Weibull plot of cleaving trials on a stepped roll. The triangles mark the samples that broke along the Airy perforation line with upper side (red) or the lower side (yellow) in extension. All other samples did not fracture along the perforation line, although the crack may initiate at the end of the line, as shown in the insert.

To achieve more reproducible conditions for the mechanical cleaving process and potentially a better cleaving result, I also tested the separability of the perforation line on a stepped roll [JSR18]. This consists of a series of cylinders with varying diameter. Starting at the largest diameters and going to smaller diameters, the structured sample is placed on each cylinder and bent until it is in full contact with the cylinder surface. This way a well defined bending stress can be induced in the work piece, if the influence of other forces can be neglected. In the trials specific care was taken to reduce frictional forces by placing the sample beneath a strip of paper, which was used to bend the sample. Half of the samples were flipped upside down after the laser process, to test extension of both top and bottom surface.

The large majority of samples did not fracture along the intended cutting line, but in many cases a V-shaped fracture pattern was observed, see Fig. 5.7. The tip of the V often coincided with the perforation line. The few samples that were separated along the perforation line do not show a significant deviation from the total data set, which can be well fitted with a two parameter Weibull distribution [Dud+20], yielding a scale parameter $T = (112 \pm 5)$ MPa and a shape parameter $b = 5.8 \pm 0.9$ respectively. Even where the separation contour follows the perforation line, the fracture in many places deviated in depth from the intended cutting surface, see Fig. 5.8. Even for samples for which the periodic laser modifications were seen throughout nearly the entire thickness of the sheet, the profile measured with confocal microscopy did not show an overall curvature.

5.2.3 Adapted processing strategy for etching

To increase the uniformity of the intensity distribution along the propagation I used an additional x2 beam expander to fully illuminate the DOE (9 mm clear aperture diameter) with a 10 mm diameter Gaussian input beam. The burst energy is increased to 300 μ J compared to the previous successful separation experiments with the standard 2D Airy-Gauss beam in Sec. 4.4 to achieve sufficiently strong modifications while the other laser parameters remain the same. For this set of parameters I

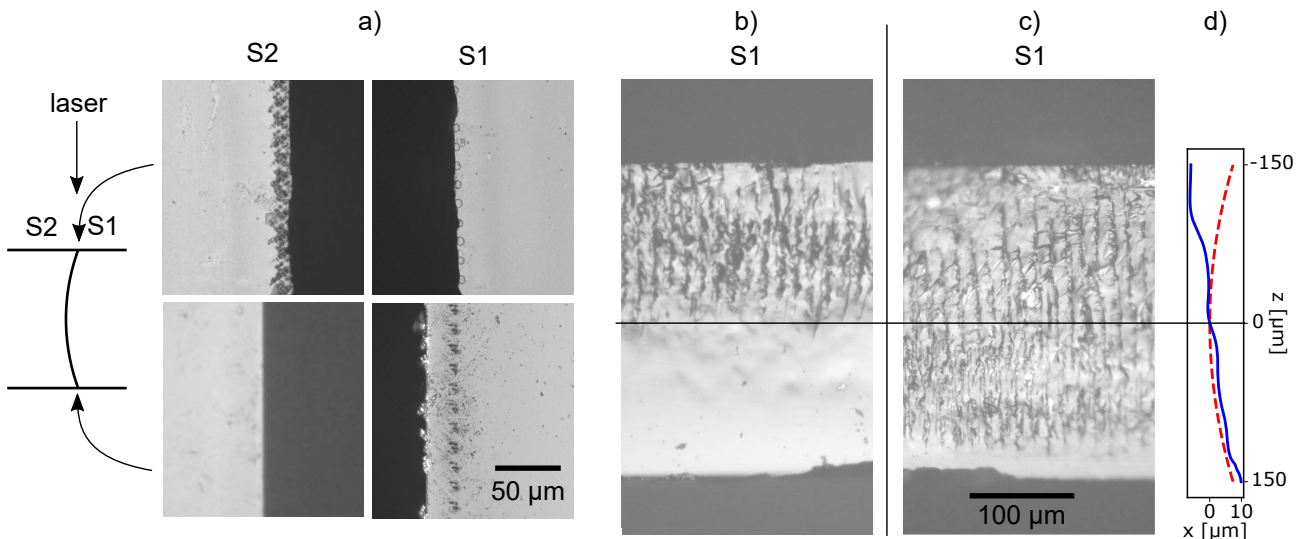


FIGURE 5.8: Top and bottom view (a) of either side of a sample that has cleaved along the perforation line on the stepped roll at a bending stress of 78 MPa with the top side in extension. At the top surface of S2 the overlapping Airy side lobes can be seen and at the bottom surface of S1 there is an offset between the perforation line and the actual cleavage. The concoidal fracture seen in the corresponding cross section (b) therefore runs into the concave side. For a sample with the bottom in extension, cleaved at 86 MPa laser modifications are seen over a broader depth range (c), but the measured height profile (d, solid blue line) does not follow the expected theoretical profile (red dashed line).

find that a lateral offset x_{off} of 770 μm compensates the asymmetric energy deposition. Such an offset corresponds to a tilt of the Airy beam by 3° in glass.

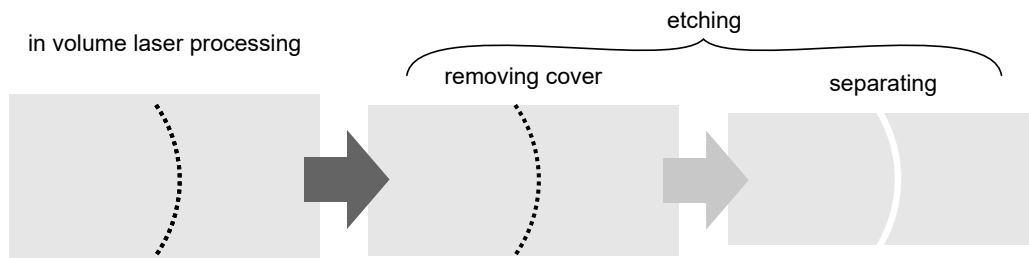


FIGURE 5.9: Schematic representation of processing method to avoid detrimental surface effects.

I place the resulting modifications, that have a length of ca. 800 μm , at the centre of a sheet of borosilicate glass that is 920 μm thick. This way I avoid complications due to the lower damage threshold at the surface, see also Fig. 5.9. Additionally, I choose a pitch that is sufficiently large to avoid overlap between neighbouring modifications, see Fig. 5.10.

In a subsequent etching step, uniform removal of the unmodified covers at both surfaces occurs before the increased etching rate of the laser modified glass leads to a separation when the etching radius exceeds the modification pitch at each depth within the sample.

5.2.4 Result after etching

Fig. 5.11 shows the symmetric edge that is produced with this revised processing strategy and the shifted focal line. The vertex of the curved height profile is positioned at the centre of the glass sheet within the accuracy of the linearly determined focus position ($\pm 50 \mu\text{m}$). The large pitch and etching

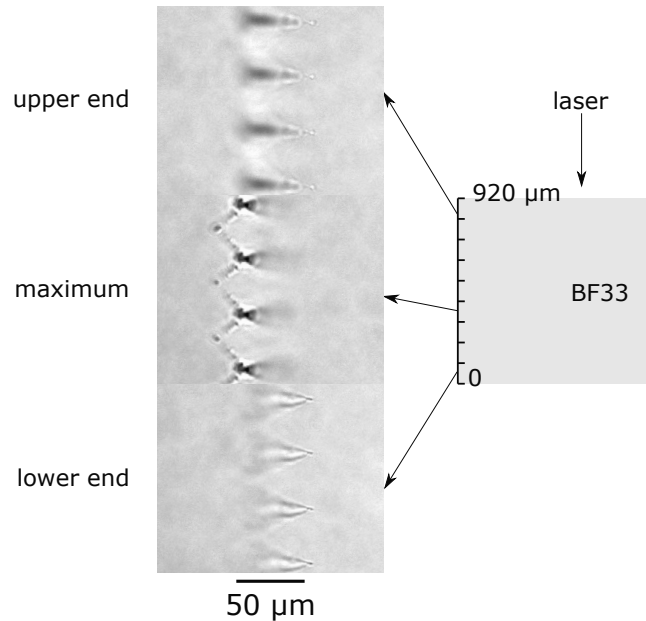


FIGURE 5.10: Lateral cross sections of the permanent modifications as used for glass cutting at three different depths within the glass. Positions of the cross sections within the glass are indicated on the left.

radius leads to pronounced height modulations with an amplitude of up to $10\ \mu\text{m}$ in horizontal cross section, which can be seen as periodic pattern in side view, see Fig. 5.11 c). The resulting edge has an effective bending radius $r_{\text{eff}} = (727 \pm 5)\ \mu\text{m}^1$, close to the previous value ($774\ \mu\text{m}$) in Sec. 4.4 and again smaller than the theoretical Airy radius ($r = 1.5\ \text{mm}$).

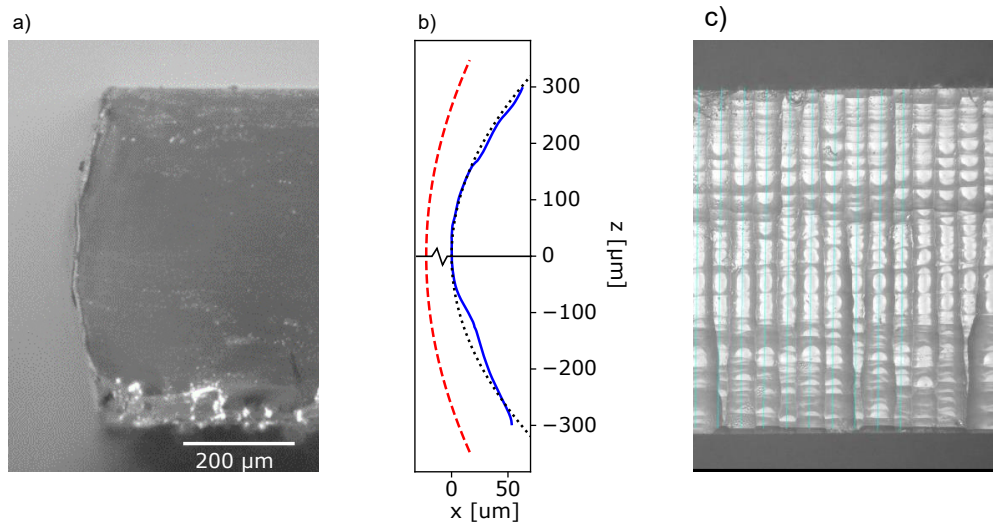


FIGURE 5.11: Convex edge (a) resulting from the etching of in volume modifications with an Airy beam using a 10 mm diameter Gaussian input beam offset by $x_{\text{off}} = 770\ \mu\text{m}$, $f = 10\ \text{mm}$, 2 pulse burst, $300\ \mu\text{J}$ burst energy, 5 ps pulse duration. The average height profile (b, solid blue) measured by confocal light microscopy in side view of the convex edge (c) shows a stronger curvature than the theoretical Airy profile (dashed red) due to etching, similar to previous results, see Fig. 4.12.

¹As in Sec. 4.4, the actual error will be larger due to the error in the confocal measurement.

5.3 Discussion

The slight homogenization of the shifted modifications as shown in Fig. 5.6 in combination with the linear simulations as shown in Fig. 3.14 indicate that a moderate spherical aberration may be favourable for a cutting process. Indeed, combining spherical aberration and coma to produce a curved focal line has previously been suggested for glass cutting applications [AH17; AH18]. The cubic phase, that is used to produce the Airy beam, in fact is simply a strong coma, so that the suggested beam corresponds to a spherically aberrated Airy beam. Our preliminary experimental results using aspheres, however, show that significant side maxima will be produced for stronger aberrated beams. In particular these are aligned in the mirror plane of the Airy beam and thus hinder the separation along the intended cutting line. There is thus a trade-off between the desirable decrease of longitudinal contrast and the undesirable increase of detrimental side lobes, when spherical aberration is added to the Airy beam. A more straightforward way of homogenizing the longitudinal intensity profile is given by using a flat top beam.

Another concept for avoiding plasma shielding and improving the energy deposition can be based on the continuous shift of the Airy focal line along a parabola, that remains fixed, as shown in Sec. 5.1: A single, continuous long modification could be constructed from several laser shots with varying offset of the Gaussian input pulse, starting at the lower part of the work piece. This could be done by fast scanning, or, going further even within a single laser pulse by introducing a strong pulse front tilt. A reduced lateral growth of the plasma and improved focal contrast could then potentially lead to a reduced shielding: At any given lateral plane above a given point at the focal line, the pulse will move from the broad, low intensity areas, that feed lower parts of the focal line, to the higher intensity region close to the main lobe at the given point. Due to the short longitudinal extent, the focal contrast can be high, also see Fig. 3.7. The experiments and simulations that will be required to show if this technique can actually lead to significant improvements goes beyond the scope of this work.

The mechanical cleaving tests on the stepped roll demonstrate that the mechanical damage along the intended curved surface is insufficient to replace other critical damage mechanisms, in particular the damage caused by the side lobes. The orientation at angles to the cutting line can cause the lateral deviation from the perforation line as seen in Fig. 5.7. Straight crack geometries originating from the region of extension can qualitatively explain the different distributions of conoidal fracture that are observed for the stepped roll trials and the manual cleaving, see Fig. 5.12.

The bending strength of the cleaved samples of 112 MPa lies close to the edge strength previously determined for edges produced by micro perforation with a Bessel beam (127 MPa [Dud+20]), but much higher than the separation stress required for a micro perforated line itself (< 30 MPa [Wer+20]).

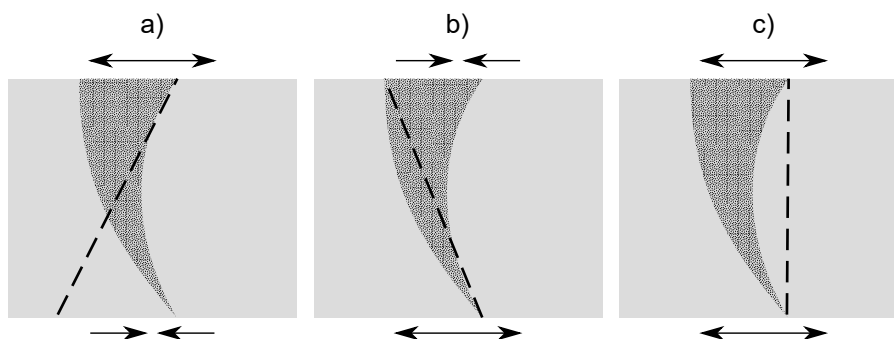


FIGURE 5.12: Schematic cross section showing how straight crack orientations (dashed lines) can be used to explain the distribution of conoidal fracture for top (a) and bottom (b) extension in the bending trials on the stepped roll, see Fig. 5.8 and for manual cleaving (c), see Fig. 4.11. The lateral scale is strongly exaggerated.

As the samples have been cut to size with a laser perforation process, this means that the Airy perforation line was not significantly weaker than an existing laser perforated edge.

The similar bending radius of the edge obtained after etching for a pure in volume modification indicates, that the extra taper angle, that has been attributed to the etching process, does not depend on surface effects, but the extent of volume damage.

5.4 Summary

The Airy focal intensity distribution can be shifted along its parabolic trajectory by lateral translation of the Gaussian input beam, resulting in a tilt

$$\theta_{\text{tl}} \approx x_0/f \quad (5.9)$$

and a defocus

$$\Delta f \approx \frac{f^2 x_{\text{off}} \beta^3 \sqrt{2}}{k}. \quad (5.10)$$

This effect has been confirmed in surface and volume modifications. Additionally, a homogenization of the damage distribution has been observed in volume modifications, which may be due to spherical aberration.

Separation tests on a stepped roll indicate, that the Airy perforation line is not weaker than the edge produced by a micro perforation process.

The symmetric positioning of a curved volume modification that can be achieved with a shifted Airy beam in a thick glass sheet can be used to produce a symmetric edge after etching.

Chapter 6

Perspectives in glass cutting

In addition to the standard 2D Airy-Gauss beam there is a whole bouquet of beam shaping concepts, that can be potentially used for laser cutting along curved trajectories. The trend towards more versatile beam shaping and custom line focus geometries has been subject of reviews already some years ago [CSC16; Efr+19], but it is only recently that glass cutting along curved trajectories has been demonstrated [STS21c; UL21; Fla+22], also see appendix D. Among those, the Airy beam, though limited by its low focal contrast, advantageously features a continuous focal line in contrast to the multi spot approach¹ [Fla+22] and reaches higher curvatures compared to an accelerated Bessel beam in the same focusing conditions [UL21], see Fig. 6.1.

Various beam shaping concepts have been proposed for modified Airy beams to improve specific aspects of the propagation behaviour. For example attenuation compensating Airy beams have been suggested [MKM14], but these are not useful for cutting glass because they have a lower focal contrast, which is particularly important for the non linear confinement, also see Sec. 2.4.1.

Attenuation and blocking of parts of the beam profile can lead to an increased contrast near the linear focus [CF10], however the contrast further along the propagation is decreased and the useable length of the Airy beam shrinks significantly.

A particularly useful Airy based beam shape has been put forward and applied for glass cutting by Ungaro and Liu [UL21]. With the “oblong” Airy beam they demonstrate a mechanically cleaved edge with a well defined parabolic height profile, see Fig. 6.1. Similarly to the Bessel beam concepts with a unique direction this beam enhances the preferential crack orientation along the intended cutting line, that is observed only at low energies for the standard 2D Airy Gauss beam, see Fig. 4.8.

The concept of a laterally elongated focus can be extended to a focal light sheet instead of a focal line. Considering the continuing increase of available pulse energies, increasingly large segments of a cutting contour can be perforated with a single shot, if appropriate beam shapes are available.

This chapter deals with the transition of a 2D Airy Gauss line focus to a 1D Airy light sheet. In the second part of this chapter the creation of in volume sheet modifications by single shots is demonstrated with a Bessel based beam shaping concept.

6.1 Oblong Airy

The oblong Airy beam is achieved, when the input beam is changed to an elliptical Gaussian beam [UL21] with an amplitude

$$E(x, y) = A_0 \exp \left[-\frac{x^2}{w_x^2} - \frac{y^2}{w_y^2} \right]. \quad (6.1)$$

where the longer beam axis is along the symmetry plane of the Airy beam, i.e. $w_y < w_x$ for the cubic phase as given in Eq. 3.37. Similarly to the Bessel beam concepts with a unique direction this

¹The elongation of the single Gaussian spots in the multi spot approach will locally lead to a preferential crack direction into the convex edge, thus impeding mechanical cleaving and weakening the edge. Separation has thus far been achieved by etching.

leads to a preferential crack orientation along the intended cutting line, which can be attributed to the deformed main lobe, but also due to the connected side lobes, which run increasingly parallel to the cutting direction with increasing ellipticity. Ungaro and Liu find that an ellipticity of $w_x/w_y = 3$ is sufficient for the preferential crack orientation. Additionally this adaptation increases the focal contrast from 1.6 to 3.6.

A flatter intensity distribution along the propagation compared to the elliptical Gaussian can be obtained when the elliptical Gaussian input beam is replaced with a rectangular input beam. With these modifications the laser processed surface could be separated by mechanical cleaving and significantly higher curvatures could be reached compared to an accelerated Bessel beam with similar focussing conditions, see Fig. 6.1.

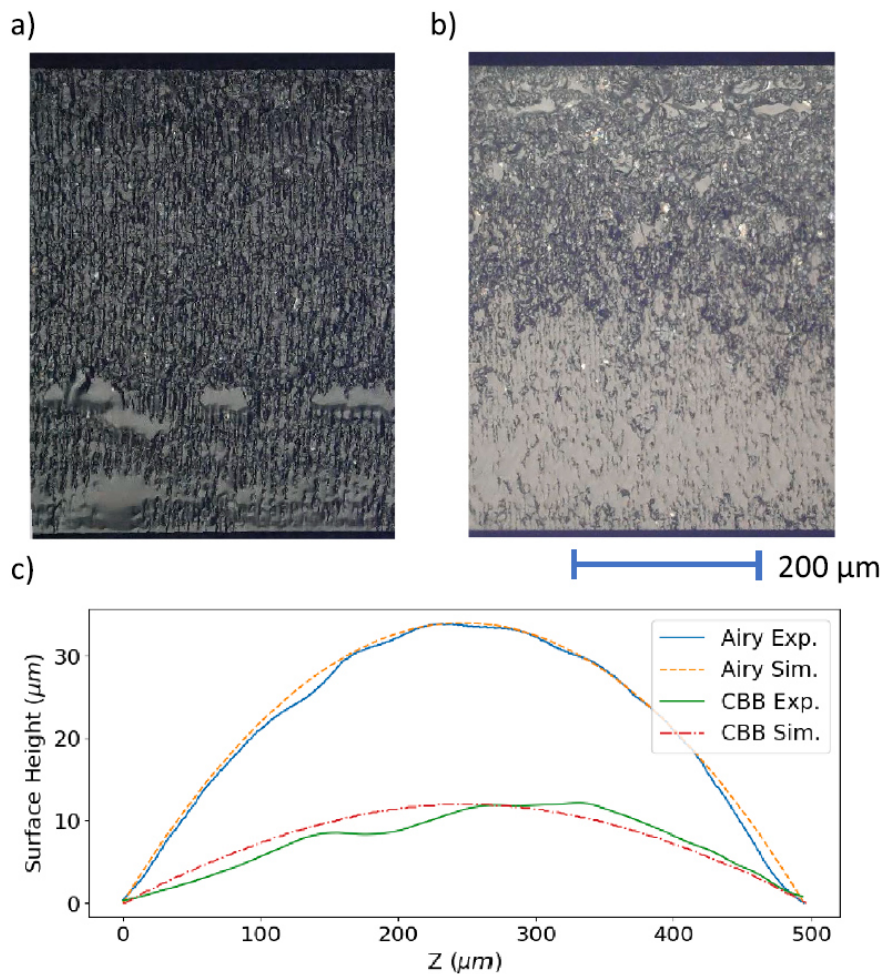


FIGURE 6.1: Side views of edges obtained by mechanical cleaving after laser processing with (oblong) Airy beam (a) and curved Bessel beam (CBB, b) respectively along with the measured height profiles (c) [UL21].

The oblong Airy seems to be a very promising candidate for glass cutting: On the one hand it improves the focal contrast that was a crucial limiting factor for the 2D Airy-Gauss beam. On the other hand, both the shape of the main lobe and the orientation of the side lobes are conveniently aligned along the intended cutting direction. I tested this beam shape in our industrial laser processing setup and found that while I could principally reproduce the preferential crack orientation, the beam turns out to be very alignment sensitive. Therefore I used an additional laboratory setup to examine the linear propagation of the focused beam in air and use the same configuration for glass modification. These experimental methods and results will be presented in the next section. Here, I examine in

more detail how the choice of the beam diameters of the elliptical Airy beam affects the beam profile during linear propagation.

6.1.1 Experimental methods and results

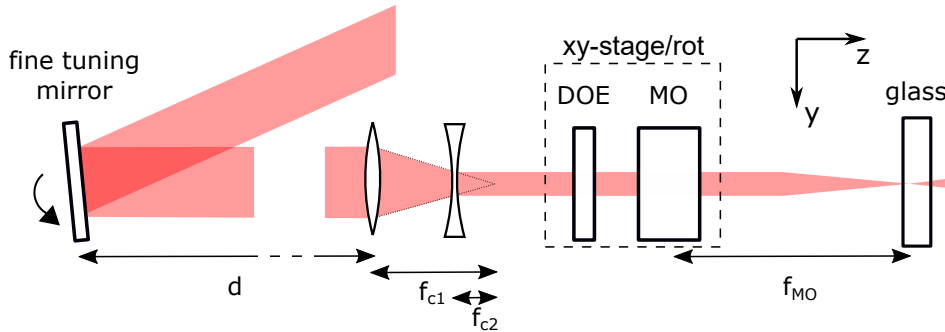


FIGURE 6.2: Optical setup used at industrial laser machine for creating

Industrial laser machine In a first attempt to use the oblong Airy for glass cutting we inserted a 3:1 cylindrical telescope, composed of a cylindrical plano-convex (Thorlabs LJ1558RM-B) and a cylindrical plano-concave (Thorlabs LK1743RM-B) lens with focal lengths 300 mm and 100 mm respectively, in the industrial laser machine that was used for previous cutting experiments, see Sec. 4.1. This way the radius of the input beam was reduced in one dimension and the radius in the other dimension was not intentionally changed, see also Fig. 6.2. However, on characterizing the beam of the Amphos laser using a Beamage-4M-FOCUS camera before the new set of experiments I found that it had increased in size and adapted a slightly triangular shape. I chose the orientation of the cylindrical telescope such that the resulting elliptical beam was as symmetric as possible and the resulting beam had beam radii were $w_x = 1.28$ mm and $w_y = 3.43$ mm. I then adjusted the orientation and positioning of the DOE by inspecting the beam profile without MO at single plane more than 1 m distance behind the DOE, sufficiently far to get a far field image of the Airy pattern, which is otherwise observed in the focal plane. Imaging of the focused beam was not possible in the industrial laser machine setup.

When considering the ablation pattern on glass, however, I found that with this adjustment the focussed beam had an astigmatic character, i.e. each of the legs was dominating on either side of the most extensive ablation pattern, which will further be referred to as focus position. Using the piezo controlled mirror as in Sec. 5.2.1, but moving principally perpendicularly to the mirror plane of the cubic phase mask, I found a setting for which the ablation patterns are symmetric on either side of the focus, but this at the same time resulted in an asymmetric distribution near the focus, see Fig. 6.3 a). At lower pulse energies and below to the focus this produces cracks in the intended direction, but at higher pulse energies and above the focus in all cases cracks were observed that run at least partially along the direction of one of the legs, see Fig. 6.3 b) and c).

Laboratory setup and results Fig. 6.4 shows the optical setup that is used to create the oblong Airy beam. The laser used here is the same as used for the imaging experiments mentioned in Sec. 4.1, an Amplitude Tangor 50, see Tab. 3.3 for the corresponding parameters. The cylinder telescope demagnifies the beam in one direction, as for the setup in the industrial laser machine. The linear intensity propagation was recorded for various combinations of the ellipticity p (i.e. the cylindrical demagnification) and the beam expansion. The Trumpf TopCleave objective with $f = 20$ mm was used as focusing optics and the Nikon N40X-PF objective for the imaging microscope.

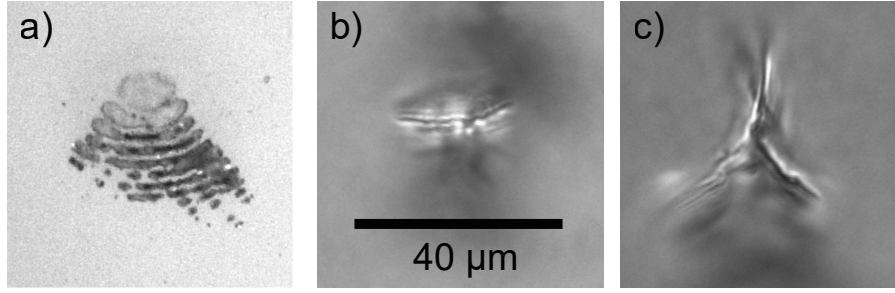


FIGURE 6.3: Surface (a) and volume modifications (b,c) produced by the an oblong Airy beam with $f = 10$ mm, with a 2 pulse burst, $t_p = 5$ ps and $E_{\text{burst}} = 98$ μJ (b) and $E_{\text{burst}} = 195$ μJ (a,c) respectively. The orientation of the Airy beam is the same for all images.

As one can see in Fig. 6.5, the morphology of the beam focus changes with the scaling of the input beam, while the ellipticity remains fixed. One can see the astigmatic character² of the elliptical beam in particular for the smaller input beam width, as the main and side lobes are broadened perpendicularly to the mirror plane in focus and evolve to a distribution that is elongated in perpendicular direction during propagation. The longitudinal contrast of the Airy beam increases as the beam diameter is reduced, as is expected for the Airy Gauss beam.

6.1.2 Linear simulation results

Numerical simulations of the focal contrast, that is given as the intensity of the largest side lobe relative to the main lobe intensity as before changes with the smaller beam radius w_y , are shown in Fig. 6.6. The contrast reaches an optimum value at an intermediate value of w_y and approaches a contrast that corresponds to the value expected for an 1D Airy Gauss beam with a cubic scaling factor β that is reduced by a factor of $\sqrt{2}$ compared to the original beam as w_y is further reduced. Note that the value of the smaller beam radius w_y at which the optimal contrast is reached does not change significantly with the extent of the long axis w_x .

6.1.3 Discussion

The crack length in the preferred orientation, that could be produced with the oblong Airy beam as seen in Fig. 6.3 is significantly larger than for the standard 2D Airy Gauss beam, before cracks start to form in different directions, also see Fig. 4.8. This finding is in line with an improved behaviour during glass cutting found in previous studies [UL21; Mis+16].

The value of the focal contrast for large ellipticities, i.e. when the Gaussian beam is reduced to the mirror plane of the 2D Airy beam, can be understood in terms of the phase of the 2D Airy-Gauss beam, as given in Eq. 3.37, on this plane

$$\phi(x, y = 0) = \frac{(\beta x)^3}{3\sqrt{2}}. \quad (6.2)$$

This corresponds to the 1D Airy phase with a reduced scaling factor. The broadening in the perpendicular direction can be understood in terms of Gaussian optics: The narrower input beam leads to a wider beam waist behind a lens. The occurrence of the optimum contrast at an intermediate value of w_y can be understood in terms of the evolution of the side lobes: Starting at the standard 2D Airy Gauss beam with $w_x = w_y$, the side lobes broaden and loose intensity more rapidly than the main

²This astigmatism does not break the mirror plane symmetry of the Airy beam in contrast to astigmatism due to an offset with respect to the mirror plane, as for example seen in Fig. 5.5.

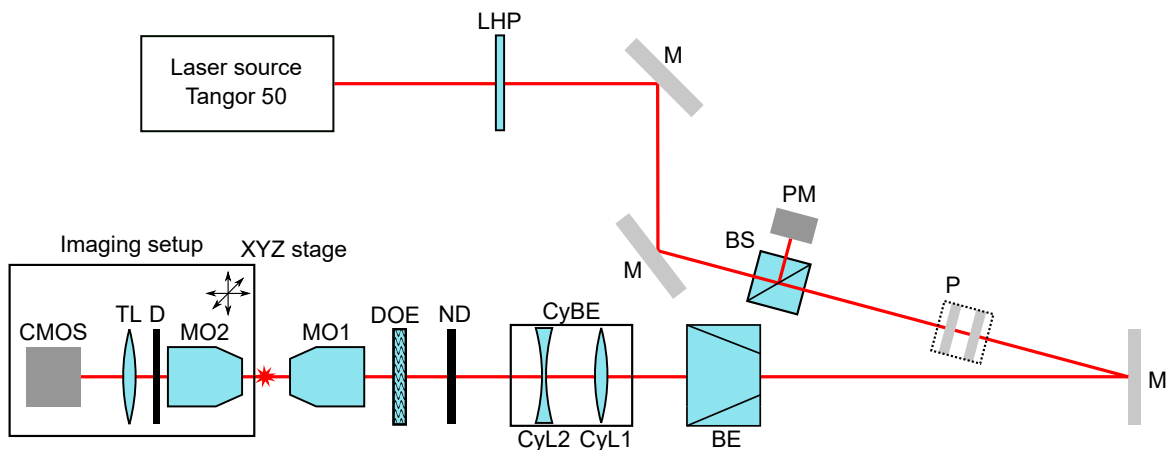


FIGURE 6.4: Optical setup for imaging the oblong Airy in air using a diffractive optical element (DOE) as phase mask. A $\lambda/2$ plate (LHP) is used in combination with a polarizing beam splitter (BS) to reduce the pulse energy of the laser pulses in the main optical path. The deflected light is sent unto a powermeter (PM) to monitor the laser power. A cylindrical telescope setup (CyBE) and an integrated beam expander (BE) are used to create an elliptical Gaussian beam with varying ellipticity and size. Neutral density filters (ND) reduce the pulse energy further, before the beam receives an extra cubic phase by the DOE and is focussed by a microscope objective (MO). The imaging setup used to record the resulting focus is comprised of a microscope objective (MO), a diaphragm (D), a tube lens (TL) and a camera (CMOS) as in Fig. 3.10. Further components of the optical setup are dielectric mirror (M) and a periscope (P).

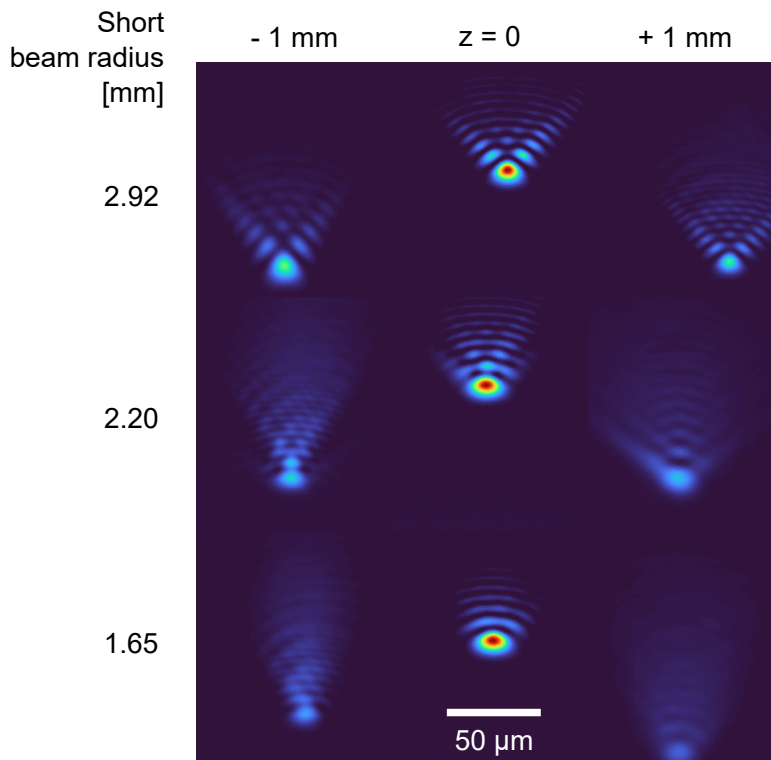


FIGURE 6.5: Intensity profiles of the oblong Airy beam measured in air around the focus position at $z = 0$ with constant ellipticity $p = 3$ and different beam expansions.

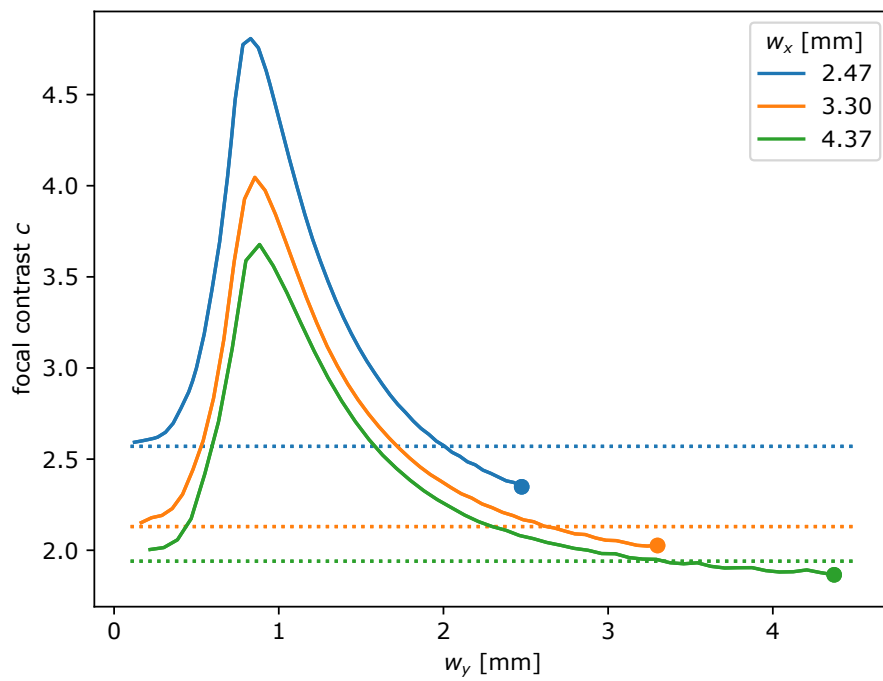


FIGURE 6.6: Simulated focal contrast for oblong Airy beams in terms of the short axis w_y for three different values of the long axis w_x , showing ellipticities w_x/w_y of 1 (marked) to 20 respectively. The dotted lines represent the contrast for an 1D Airy Gauss beam with $\beta^3 = \beta_0^3/\sqrt{2}$ respectively.

lobe as w_y is reduced and eventually join, forming a quarter of an elliptical contour. As w_y is further decreased, the side lobes merge into one side lobe, that increases in length along y and is increasingly flat.

The optimum contrast is reached when the side lobes join but are not yet merged. This is corroborated by the observation that the focal waist diameter $w_f = 15.4 \mu\text{m}$ of a Gaussian beam with $w_0 = 0.85 \text{ mm}$, i.e. the value of the smaller beam diameter for optimal contrast in Fig. 6.6, is very close to the distance $d_{sl} \approx 1.6\sqrt{2}x_0 = 15.1 \mu\text{m}$ between the side lobes in the Airy beam. Bearing in mind that only the relative intensity of the side lobes but not their lateral position is affected by the beam diameter, one would indeed expect that the optimum contrast depends only on the small axis, as long as w_x sufficiently large.

Overall the oblong Airy can thus be understood as a transitional beam shape between a 2D Airy focal line and a 1D Airy light sheet.

6.2 Light blade glass cutting

The light sheet is, in fact, a particularly interesting beam shape for glass cutting: We are generally aiming to create a weakened surface in glass along which we want to separate the sample. Instead of using line foci, that are placed next to each other, we could create a micro explosion along a surface if sufficient pulse energy is available. For this, a high confinement, i.e. a low thickness, is required in one spatial dimension, to achieve the necessary energy density without affecting the surrounding material, while the other two dimensions, the width and length of the light sheet, would conceptually only be limited by the pulse energy.

The Airy beam as well as other caustic beam shapes are well suited for creating a light sheet, as they provide a non diffracting beam with a localized main lobe even in 1D. For example, 1D Airy light sheets have been demonstrated in previous work by the use of cylinder lenses [Yan+14] thus introducing a cubic phase or by using the direct space shaping of the Airy beam, see [Fro+11] and Sec. 3.5. In each case however, the low focal contrast would pose a significant limitation for glass processing.

An alternative way to construct construct light sheets is based on the Bessel beam [Zan+20]. This section deals with this Bessel based beam shaping concept and its application to glass cutting.

6.2.1 Beam shaping concept

Zannotti et al. [Zan+20] use the Bessel beam as a "pen" to draw arbitrary lateral contours, which are extended along the propagation due the non-diffracting character of the Bessel contributions, that constitute the phase. They calculate the phase for this Bessel pen line in Fourier space, as the integral of the spectral components for Bessel contributions along the line. The same concept can be transferred to direct space beam shaping, so that the total phase

$$\phi_{\text{total}}(\rho) = \frac{1}{s} \sum_i^n a_i |(\rho - \rho_i)| \quad (6.3)$$

is obtained by adding n conical contributions, the Bessel beamlets, positioned at $\rho_i = (x_i, y_i)$ respectively [Ort+22b]. For a linear geometry for example

$$\rho_i = \rho_{\text{start}} + \frac{i}{n}(\rho_{\text{end}} - \rho_{\text{start}}) \quad (6.4)$$

as shown in Fig. 6.7.

Weighting factors can be used to achieve a favourable intensity distribution along the line, and they are given as a function of position ρ_i , for example $a_i(\rho_i) = c |\rho_i|$ with constant c for a linear correction.

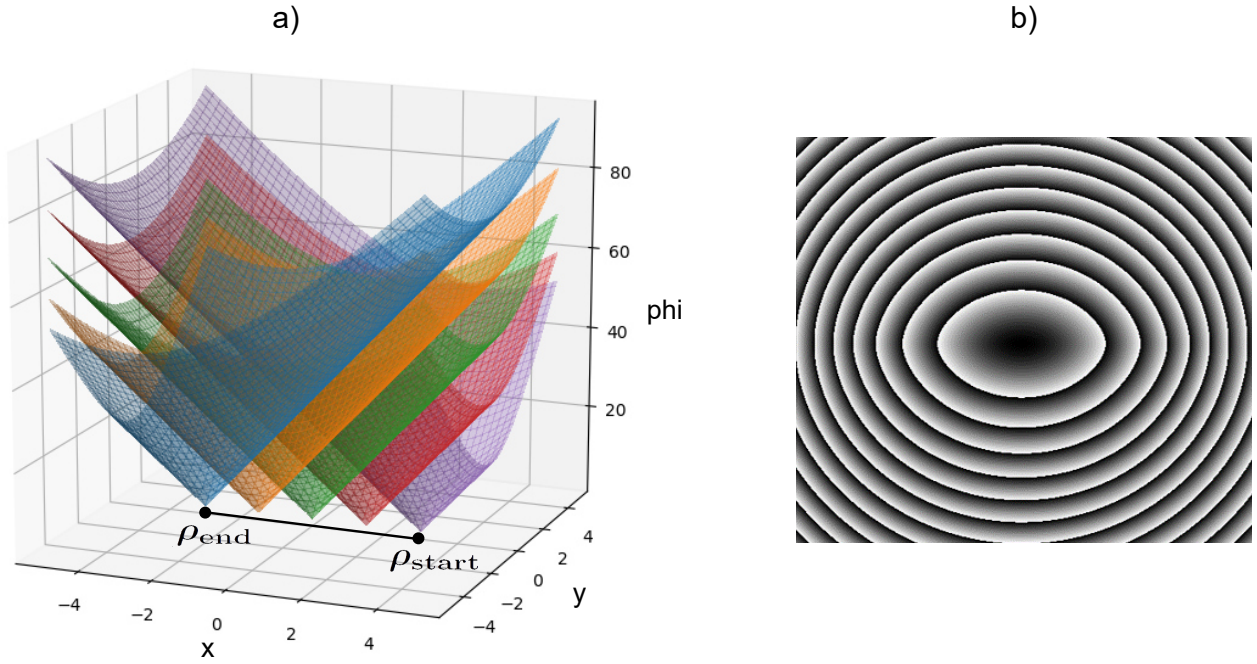


FIGURE 6.7: Schematic representation of conical phases (a) that are added along a line to obtain the overall phase (b) for creating a planar light sheet.

The overall scaling factor s is used to normalize the sum of the conical contributions, for example an effective Bessel cone angle θ_B is obtained by

$$s = \frac{2\pi}{\lambda} \tan(\theta_B) \sum_i^n a_i. \quad (6.5)$$

6.2.2 Experimental setup and results

Fig. 6.8 shows the 4f setup that I used to create the Bessel light sheet for glass structuring. The beam diameter is expanded to $2w_0 = 6.6$ mm to achieve a good filling of the SLM with which a phase as shown in Fig. 6.7 b) is added to the beam. The length of the line $|\rho_{\text{end}} - \rho_{\text{start}}| = 1.6$ mm and the resulting effective cone angle of the Bessel beam in glass is 12.4° , which is produced by a Bessel cone angle in air of 0.38° that is demagnified by a 50:1 telescope. The telescope consists of a spherical lens L1 (Thorlabs LA1908-B) with $f_1 = 500$ mm and a microscope objective (Mitutoyo MY10X-823) with $f = 10$ mm.

I placed a sheet of 1 mm thick borosilicate glass at the focus and characterised the beam by a scan along the propagation direction as shown in Fig. 4.1. Fig. 6.9 shows the ablation patterns at different relative focal positions. One can see that the useable length of the focal line is limited to roughly $40 \mu\text{m}$, before it broadens and quickly reaches a conjugate point of the astigmatic beam propagation, where the lateral aspect ratio is roughly equal before it evolves into an elongated shape in the orthogonal lateral direction further along the propagation.

For a cross section view of the modifications and to examine the light sheet volume modifications without the influence of the astigmatic evolution of the beam profile, a thin section of the glass sheet was produced and subsequently cleaved along the laser modified line. In Fig. 6.10 one can see that the focal sheet is associated with cracks, that extend beyond the extent seen at the surface, especially if a burst mode is used. One can, however, also see that there is a distinct zone in cross section, that directly corresponds in position and width with the laser sheet observed at the surface. This

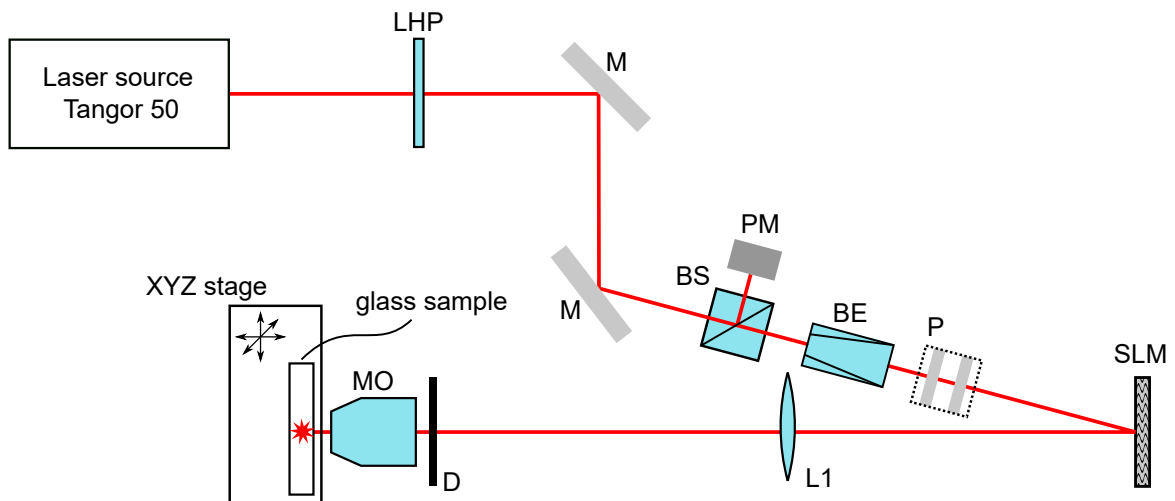


FIGURE 6.8: Optical setup for light sheet glass processing using a spatial light modulator (SLM) as phase mask. The beam width is increased before the SLM with a beam expander (BE) to achieve a high filling of the phase mask. The beam is then demagnified by a 4f setup by the lens L1 and the microscope objective (MO) and imaged onto the glass sample, that is mounted on an XYZ stage. Other optical components as above in Fig. 6.4.



FIGURE 6.9: Ablation pattern along the propagation of the Bessel pen line with $dz = 20 \mu\text{m}$ for single pulses and a pulse duration of 411 fs.

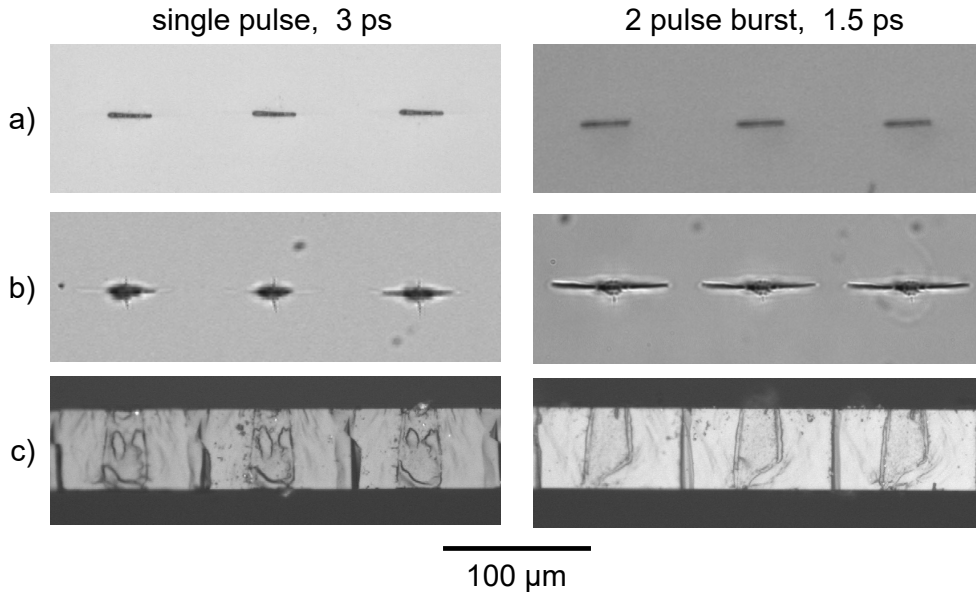


FIGURE 6.10: Corresponding top views of the surface (a) and volume (b) damage and cross section (c) of glass modifications produced with a Bessel light sheet with $E_{\text{burst}} = 36 \mu\text{J}$, $f = 10 \text{ mm}$ and $\theta_B = 12.4^\circ$.

is therefore the volume that was directly affected by the laser focus and is the 2D equivalent of the voids, that can be seen in perforation lines as in Fig. 2.2.

6.3 Summary

The oblong Airy beam can be used to create cracks in the intended cutting direction for larger pulse energies compared to the standard 2D Airy Gauss beam.

The smaller beam axis has to be sufficiently small for a given cubic phase and focusing lens to provoke the elongation, which makes it more sensitive to astigmatic distortion, that leads to cracks that are unfavourably oriented. An optimum value for the contrast is reached at specific values of the extent of the shorter beam axis. As this width is reduced further, the contrast approaches the value expected for a 1D Airy for the cubic phase along the mirror plane of the Airy beam. The focal distributions evolves towards a 1D Airy light sheet.

A straight light sheet can be created as the superposition of Bessel lines. The resulting volume modification consists of a distinct laser modified surface and cracks that run parallel to this surface.

Chapter 7

Conclusions

Motivated by the wide spread need of glass sheets with a c-shaped edge and the availability of increasingly cheap and powerful industrial sources of ultra short laser pulses, this work sets out to augment the range of focal intensity distributions that are used for the cutting of glass sheets by laser micro perforation to curved geometries [OST20]. This way, additional mechanical grinding steps that are nowadays still required for edge shaping even for glasses that have been cut to shape with a laser beam, can be replaced or at least reduced.

As the main result of this study, shown in Fig. 5.11, a 600 μm thick glass sheet with a symmetric, parabolic edge has been produced by single pass laser structuring of a 920 μm thick glass sheet with an Airy beam and subsequent etching [STS22a].

This result has been obtained by adjustments of the Airy beam after the world first demonstration of micro perforation glass cutting with an Airy beam [STS21c] of a 525 μm thick glass sheet, see Sec. 4.4.

Both edges exhibit the same curvature, which is larger than the theoretically expected value for the Airy beam that has been used. Volume modifications observed right after the laser process on the other hand follow the parabolic trajectory that is expected from the linear propagation of the Airy beam, see Sec. 4.2. The extra curvature can therefore be attributed to the etching step.

In chapter 3, the linear scaling of the focal line produced with an Airy beam is discussed in detail with respect to the crucial parameters that determine the maximum thickness and curvature that can be achieved for optics that in many cases are limited by the available numerical aperture. The trade-offs between achievable length, curvature and focal contrast of the Airy beam are presented in terms of previously derived analytical expressions of the paraxial propagation of the Airy beam.

As an alternative way for calculating the linear propagation of the Airy beam a Fast Fourier Transform (FFT) based algorithm has been used in this study. In the case of an aberration free 2D Airy Gauss and in paraxial conditions this can be done particularly fast, as the 2D Airy Gauss beam itself is obtained as the product of two orthogonal 1D solutions, which can be propagated independently. A full 2D FFT propagator can be used to examine the effect of variations of the Airy beam, that are not readily expressed in terms of analytical expressions, for example spherical aberration and elliptical input beams. While later simulations of the elliptical beam were performed on super-computer to provide sufficient memory for a full resolution of the experimental beams, simulations of the spherical aberrated and the shifted Airy beam were been performed on local machines with Python based propagation routines that were written in the course of this project.

The linear propagation of the Airy beam has also been characterized experimentally in a laboratory setup, which has been newly assembled in this project and which enables fast switching between a microscope setup for imaging of a focused beam and a setup for micro structuring of glass.

While the volume modifications very well follow the expected curvature and their increase in length up to more than 2 mm can be reasonably described in terms of the linear propagation and a constant intensity threshold for given focusing conditions, see Fig. 4.5 and Fig. 4.6, the influence of non linear propagation effects can clearly be seen in volume modifications, see Fig. 4.2. Most notably, for the parameter range considered here with pulse durations of up to 10 ps, volume modifications are more distinct for longer pulses compared to broad and weak modifications observed at 1 ps and,

with increasing pulse energy, the modification morphology deviates from the longitudinal distribution that is expected to be symmetric around the linear focus: The lower part of the modification is suppressed, while the extent of material damage in the upper part increases. Both asymmetry and weak modifications at short pulses can be understood in terms of the non linear propagation dynamics, which govern the energy transfer from the laser pulse to the glass. For a better understanding of these dynamics, a pre-existing unidirectional pulse propagation model has been employed that accounts for the relevant non linear effects, in particular the generation of conduction band electrons. The results shown in Sec. 4.5 indicate that the low confinement for short pulses and the asymmetry can be explained in terms of the creation of a plasma in the side lobes of the Airy beam. The resulting absorption and defocusing of the incoming light by the plasma lead to a preferential energy deposition in the upper part of the glass and an impeded light propagation to the lower parts of the focal line.

The resulting tilt of the Airy beam has led to an asymmetry in the first Airy cut edge. Compensation of this non linear tilt is possible by shifting the Gaussian input beam with respect to phase mask and microscope objective, see chapter 5. Here, a straightforward geometrical concept is presented for calculating the tilt and defocus based on the low order aberrations within the shifted coordinate system and confirmed in experimental observations. With this adaptation, a symmetric positioning of the Airy in the volume of the glass sheet is possible and a symmetric edge could be achieved without requiring a tilt of the mechanical axes.

This study further deals with details of the non linear absorption of laser light in borosilicate glass. By making use of the low focal contrast of the Airy beam, that causes the otherwise unfavourable absorption in the side lobes, the effective electron collision time is estimated here as 20 fs by comparison between simulation and experiments, see appendix C. Absorption measurements in borosilicate glass that have been performed as a masters project within the framework of this study [Sch21], see Fig. 2.12, may be further used to constrain the non linear propagation properties of borosilicate glass.

Tighter focusing conditions are associated with a lower intensity threshold for volume damage, see Sec. 4.2. This is in agreement with significant distributed plasma shielding, which is observed in non linear simulation results. As already pointed out in previous studies this can be reduced by the use of a burst mode. The non linear model also predicts that longer pulse duration are more favourable for an efficient, confined energy deposition. An experimental finding in this study is, however, that for an effective NA of 0.27 an intermediate pulse duration (5 ps) and intermediate number of pulses in a burst (2) is favourable to obtain a full perforation of borosilicate sheets for thicknesses between 0.3 mm and 1 mm and burst energies of up to 300 μ J, see Sec. 4.3.

The upper limit on the number of pulses in a burst is given by the extent of cracks that in particular are created in the side lobes of the Airy beam and point away from the intended cutting surface, also see Sec. 4.3. In particular this limits the application of the standard Airy Gauss beam to mechanical cleaving.

The alignment of mechanical cracks along the intended cutting direction has recently been demonstrated with a variation of the Airy beam that is created by using an elliptical input beam. In this study, the impact of the relative scaling of the Gaussian input beam and the beam shaping phase is examined in more detail and the "oblong" Airy is identified as a transitional beam shape between a 2D Airy focal line and a 1D Airy focal light sheet, see Sec. 6.1.

Micro perforation cutting processes rely on the creation of a weakened surface within the volume of the sample, along which it is subsequently separated. Current beam shaping concepts use a series of channels, that overall define a surface. In a completely new approach conceived in this project, the application of light sheets for glass cutting is demonstrated [Ort+22b], directly creating a 2D surface with a single laser shot, see Sec. 6.2. In the context of increasing laser power and, at the same time, increased interest in thin glass sheets, light sheet cutting has a great potential for enabling automated, high throughput processes. The adaptation of caustic beam shapes and other light sheets therefore provides material for a wide range of further research.

Bibliography

- [AB15] Christos-Edward Athanasiou and Yves Bellouard. “A Monolithic Micro-Tensile Tester for Investigating Silicon Dioxide Polymorph Micromechanics, Fabricated and Operated Using a Femtosecond Laser”. In: *Micromachines* 6.9 (2015), pp. 1365–1386. ISSN: 2072-666X. DOI: [10.3390/mi6091365](https://doi.org/10.3390/mi6091365).
- [ACP87] Robert Adair, L. L. Chase, and Stephen A. Payne. “Nonlinear refractive-index measurements of glasses using three-wave frequency mixing”. In: *Journal of the Optical Society of America B* 4.6 (1987), p. 875. ISSN: 0740-3224. DOI: [10.1364/JOSAB.4.000875](https://doi.org/10.1364/JOSAB.4.000875).
- [AER18] A. Horn, E. W. Kreutz, and R. Poprawe. “Time-resolved-photography and transient absorption spectroscopy of excited dielectrics by infrared ultrashort laser radiation”. In: *Pacific International Conference on Applications of Lasers and Optics* 2004.1 (2018), p. M505. DOI: [10.2351/1.5056160](https://doi.org/10.2351/1.5056160).
- [AH17] S. Abbas Hosseini. *Method and apparatus for performing laser curved filamentation within transparent materials*. US Patent 9757815 B2. 2017.
- [AH18] S. Abbas Hosseini. *Method and apparatus for performing laser curved filamentation within transparent materials*. US Patent 10010971 B1. 2018.
- [Ala+19] Sabri Alamri et al. “On the interplay of DLIP and LIPSS upon ultra-short laser pulse irradiation”. In: *Materials* 12.7 (2019), p. 1018. DOI: [10.3390/ma12071018](https://doi.org/10.3390/ma12071018).
- [BB79] M. V. Berry and N. L. Balazs. “Nonspreading wave packets”. In: *American Journal of Physics* 47.3 (1979), pp. 264–267. ISSN: 0002-9505. DOI: [10.1119/1.11855](https://doi.org/10.1119/1.11855).
- [BCD73] N. L. Boling, M. D. Crisp, and G. Dubé. “Laser Induced Surface Damage”. In: *Applied Optics* 12.4 (Apr. 1973), p. 650. DOI: [10.1364/ao.12.000650](https://doi.org/10.1364/ao.12.000650).
- [Bec+01] A. Becker et al. “Intensity clamping and re-focusing of intense femtosecond laser pulses in nitrogen molecular gas”. In: *Applied Physics B* 73.3 (2001), pp. 287–290. ISSN: 1432-0649. DOI: [10.1007/s003400100637](https://doi.org/10.1007/s003400100637).
- [Bel+21] Valeria V Belloni et al. “Generation of extremely high cone angle Bessel beam”. In: *Laser Science*. Optica Publishing Group. 2021, JTU1A–27. DOI: [10.1364/FIO.2021.JTU1A.27](https://doi.org/10.1364/FIO.2021.JTU1A.27).
- [Ber+08] L. Bergé et al. “Ultrashort filaments of light in weakly ionized, optically transparent media”. In: *Reports on Progress in Physics* 71.10 (2008), p. 109801. ISSN: 0034-4885. DOI: [10.1088/0034-4885/71/10/109801](https://doi.org/10.1088/0034-4885/71/10/109801).
- [Ber+18a] K. Bergner et al. “Spatio-temporal analysis of glass volume processing using ultrashort laser pulses”. In: *Applied Optics* 57.16 (2018), pp. 4618–4632. DOI: [10.1364/AO.57.004618](https://doi.org/10.1364/AO.57.004618).
- [Ber+18b] Klaus Bergner et al. “Scaling ultrashort laser pulse induced glass modifications for cleaving applications”. In: *Applied Optics* 57.21 (2018), pp. 5941–5947. DOI: [10.1364/AO.57.005941](https://doi.org/10.1364/AO.57.005941).
- [Beu+17] Romain Beuton et al. “Thermo-elasto-plastic simulations of femtosecond laser-induced structural modifications: Application to cavity formation in fused silica”. In: *Journal of Applied Physics* 122.20 (2017), p. 203104. ISSN: 0021-8979. DOI: [10.1063/1.4993707](https://doi.org/10.1063/1.4993707).

- [Beu+18] R. Beuton et al. "Thermo-elasto-plastic simulations of femtosecond laser-induced multiple-cavity in fused silica". In: *Applied Physics A* 124.4 (2018), p. 1729. ISSN: 0947-8396. DOI: [10.1007/s00339-018-1743-x](https://doi.org/10.1007/s00339-018-1743-x).
- [Beu19] Romain Beuton. "Modélisation de la structuration d'un matériau diélectrique irradié par une impulsion laser femtoseconde". PhD thesis. Université de Bordeaux, 2019.
- [BGO78] N. Boling, A. Glass, and A. Owyong. "Empirical relationships for predicting nonlinear refractive index changes in optical solids". In: *IEEE Journal of Quantum Electronics* 14.8 (1978), pp. 601–608. ISSN: 0018-9197. DOI: [10.1109/JQE.1978.1069847](https://doi.org/10.1109/JQE.1978.1069847).
- [Bhu+14] M. K. Bhuyan et al. "Single-shot high aspect ratio bulk nanostructuring of fused silica using chirp-controlled ultrafast laser Bessel beams". In: *Applied Physics Letters* 104.2 (2014), p. 021107. ISSN: 0003-6951. DOI: [10.1063/1.4861899](https://doi.org/10.1063/1.4861899).
- [BKM21] David Bischof, Michael Kahl, and Markus Michler. "Laser-assisted etching of borosilicate glass in potassium hydroxide". In: *Optical Materials Express* 11.4 (2021), p. 1185. DOI: [10.1364/OME.417871](https://doi.org/10.1364/OME.417871).
- [Blo73] N. Bloembergen. "Role of Cracks, Pores, and Absorbing Inclusions on Laser Induced Damage Threshold at Surfaces of Transparent Dielectrics". In: *Applied Optics* 12.4 (1973), pp. 661–664. DOI: [10.1364/AO.12.000661](https://doi.org/10.1364/AO.12.000661).
- [Boy08] Robert W. Boyd. *Nonlinear optics*. 3rd ed. Burlington, MA: Academic Press, 2008. ISBN: 9780080569598. URL: <https://learning.oreilly.com/library/view/-/9780123694706/?ar>.
- [Bro+08] John Broky et al. "Self-healing properties of optical Airy beams". In: *Optics Express* 16.17 (2008), pp. 12880–12891. DOI: [10.1364/oe.16.012880](https://doi.org/10.1364/oe.16.012880).
- [BS07] Ioannis M. Besieris and Amr M. Shaarawi. "A note on an accelerating finite energy Airy beam". In: *Optics Letters* 32.16 (2007), pp. 2447–2449. DOI: [10.1364/ol.32.002447](https://doi.org/10.1364/ol.32.002447).
- [BSL60] Robert Byron Bird, Warren E. Stewart, and Edwin N. Lightfoot. *Transport phenomena*. New York: Wiley, 1960. ISBN: 047107392X.
- [Bul+15] Nadezhda M. Bulgakova et al. "Modification of transparent materials with ultrashort laser pulses: What is energetically and mechanically meaningful?" In: *Journal of Applied Physics* 118.23 (2015), p. 233108. ISSN: 0021-8979. DOI: [10.1063/1.4937896](https://doi.org/10.1063/1.4937896).
- [But+21] Agnè Butkutė et al. "Optimization of selective laser etching (SLE) for glass micromechanical structure fabrication". In: *Optics Express* 29.15 (2021), pp. 23487–23499. DOI: [10.1364/OE.430623](https://doi.org/10.1364/OE.430623).
- [Can+11] J Canning et al. "Anatomy of a femtosecond laser processed silica waveguide". In: *Optical Materials Express* 1.5 (2011), pp. 998–1008. DOI: [10.1364/OME.1.000998](https://doi.org/10.1364/OME.1.000998).
- [CDH09] Don M. Cottrell, Jeffrey A. Davis, and Thomas M. Hazard. "Direct generation of accelerating Airy beams using a 3/2 phase-only pattern". In: *Optics Letters* 34.17 (2009), pp. 2634–2636. DOI: [10.1364/OL.34.002634](https://doi.org/10.1364/OL.34.002634).
- [CE13] I. D. Chremmos and N. K. Efremidis. "Nonparaxial accelerating Bessel-like beams". In: *Physical Review A* 88.6 (2013). ISSN: 1094-1622. DOI: [10.1103/physreva.88.063816](https://doi.org/10.1103/physreva.88.063816).
- [CF10] M. I. Carvalho and M. Facão. "Propagation of Airy-related beams". In: *Optics Express* 18.21 (2010), pp. 21938–21949. DOI: [10.1364/OE.18.021938](https://doi.org/10.1364/OE.18.021938).
- [CGT64] Raymond Y Chiao, E Garmire, and Charles H Townes. "Self-trapping of optical beams". In: *Physical review letters* 13.15 (1964), p. 479.
- [Cho+13] Dawoon Choi et al. "Generation of finite power Airy beams via initial field modulation". In: *Optics Express* 21.16 (2013), pp. 18797–18804. DOI: [10.1364/OE.21.018797](https://doi.org/10.1364/OE.21.018797).

- [Chr+12] Ioannis D. Chremmos et al. "Bessel-like optical beams with arbitrary trajectories". In: *Optics Letters* 37.23 (2012), pp. 5003–5005. DOI: [10.1364/OL.37.005003](https://doi.org/10.1364/OL.37.005003).
- [CM07] A. Couairon and A. Mysyrowicz. "Femtosecond filamentation in transparent media". In: *Physics Reports* 441.2 (2007), pp. 47–189. ISSN: 0370-1573. DOI: [10.1016/j.physrep.2006.12.005](https://doi.org/10.1016/j.physrep.2006.12.005).
- [Coh18] Coherent. *New Lasers Improve Glass Cutting Methods*. 2018. URL: https://content.coherent.com/legacy-assets/pdf/Coherent-new-lasers-improve-glass-cutting-methods_wp.pdf (visited on 04/06/2022).
- [CSC16] F. Courvoisier, R. Stoian, and A. Couairon. "[INVITED] Ultrafast laser micro- and nano-processing with nondiffracting and curved beams". In: *Optics & Laser Technology* 80 (2016), pp. 125–137. ISSN: 00303992. DOI: [10.1016/j.optlastec.2015.11.026](https://doi.org/10.1016/j.optlastec.2015.11.026).
- [Dar+06] C. A. Dartora et al. "A general theory for the Frozen Waves and their realization through finite apertures". In: *Optics Communications* 265.2 (2006), pp. 481–487. ISSN: 00304018. DOI: [10.1016/j.optcom.2006.03.057](https://doi.org/10.1016/j.optcom.2006.03.057).
- [DC+15] O Dematteo Caulier et al. "Femtosecond laser pulse train interaction with dielectric materials". In: *Applied Physics Letters* 107.18 (2015), p. 181110. DOI: [10.1063/1.4935119](https://doi.org/10.1063/1.4935119).
- [DGR16] Juozas Dudutis, Paulius Gečys, and Gediminas Račiukaitis. "Non-ideal axicon-generated Bessel beam application for intra-volume glass modification". In: *Optics Express* 24.25 (2016), pp. 28433–28443. DOI: [10.1364/OE.24.028433](https://doi.org/10.1364/OE.24.028433).
- [DJ20] David Kinsella and Johan Lindström. "Using a Hierarchical Weibull model to Predict Failure Strength of Different Glass Edge Profiles". In: *International journal of structural glass and advanced materials research* 4 (2020), pp. 130–148. ISSN: 2616-4507. DOI: [10.3844/sgamrsp.2020.130.148](https://doi.org/10.3844/sgamrsp.2020.130.148).
- [DME87] Durnin, Miceli, and Eberly. "Diffraction-free beams". In: *Physical Review Letters* 58.15 (1987), pp. 1499–1501. DOI: [10.1103/PhysRevLett.58.1499](https://doi.org/10.1103/PhysRevLett.58.1499).
- [Dud+18] Juozas Dudutis et al. "Bessel beam asymmetry control for glass dicing applications". In: *Procedia CIRP* 74 (2018), pp. 333–338. DOI: [10.1016/j.procir.2018.08.127](https://doi.org/10.1016/j.procir.2018.08.127).
- [Dud+19] Juozas Dudutis et al. "Glass dicing with elliptical Bessel beam". In: *Optics & Laser Technology* 111 (2019), pp. 331–337. ISSN: 00303992. DOI: [10.1016/j.optlastec.2018.10.007](https://doi.org/10.1016/j.optlastec.2018.10.007).
- [Dud+20] Juozas Dudutis et al. "In-depth comparison of conventional glass cutting technologies with laser-based methods by volumetric scribing using Bessel beam and rear-side machining". In: *Optics Express* 28.21 (2020), pp. 32133–32151. DOI: [10.1364/OE.402567](https://doi.org/10.1364/OE.402567).
- [Eat+05] Shane Eaton et al. "Heat accumulation effects in femtosecond laser-written waveguides with variable repetition rate". In: *Optics Express* 13.12 (2005), pp. 4708–4716. DOI: [10.1364/opex.13.004708](https://doi.org/10.1364/opex.13.004708).
- [Eat+08] Shane M Eaton et al. "Transition from thermal diffusion to heat accumulation in high repetition rate femtosecond laser writing of buried optical waveguides". In: *Optics Express* 16.13 (2008), pp. 9443–9458. DOI: [10.1364/OE.16.009443](https://doi.org/10.1364/OE.16.009443).
- [Efr+19] N. K. Efremidis et al. "Airy beams and accelerating waves: an overview of recent advances". In: *Optica* 6.5 (2019), p. 686. DOI: [10.1364/OPTICA.6.000686](https://doi.org/10.1364/OPTICA.6.000686).
- [Eng+08] L. Englert et al. "Material processing of dielectrics with temporally asymmetric shaped femtosecond laser pulses on the nanometer scale". In: *Applied Physics A* 92.4 (2008), pp. 749–753. ISSN: 0947-8396. DOI: [10.1007/s00339-008-4584-1](https://doi.org/10.1007/s00339-008-4584-1).

- [Epp+12] U. Eppelt et al. "Diagnostic and simulation of ps-laser glass cutting". In: *International Congress on Applications of Lasers & Electro-Optics*. Vol. 2012. 1. Laser Institute of America. 2012, pp. 835–844. URL: <https://www.iop.rwth-aachen.de/go/id/gpia/file/124619>.
- [Feu+19] A. Feuer et al. "Single-pass laser separation of 8 mm thick glass with a millijoule picosecond pulsed Gaussian–Bessel beam". In: *Applied Physics A* 125.5 (2019), pp. 1–6. ISSN: 0947-8396. DOI: [10.1007/s00339-019-2624-7](https://doi.org/10.1007/s00339-019-2624-7).
- [Fla+15] D Flamm et al. "Tuning the energy deposition of ultrashort pulses inside transparent materials for laser cutting applications". In: *Proc. LiM* 253 (2015).
- [Fla+19] Daniel Flamm et al. "Beam shaping for ultrafast materials processing". In: *Laser Resonators, Microresonators, and Beam Control XXI*. Ed. by Alexis V. Kudryashov, Alan H. Paxton, and Vladimir S. Ilchenko. SPIE, 2019. DOI: [10.1117/12.2511516](https://doi.org/10.1117/12.2511516).
- [Fla+22] Daniel Flamm et al. "Protecting the edge: Ultrafast laser modified C-shaped glass edges". In: *Journal of Laser Applications* 34.1 (2022), p. 012014. ISSN: 1042-346X. DOI: [10.2351/7.0000592](https://doi.org/10.2351/7.0000592).
- [Fro+11] L. Froehly et al. "Arbitrary accelerating micron-scale caustic beams in two and three dimensions". In: *Optics Express* 19.17 (2011), pp. 16455–16465. DOI: [10.1364/OE.19.016455](https://doi.org/10.1364/OE.19.016455).
- [Gam+07] Eugene Gamaly et al. "Laser-matter interaction in the bulk of transparent dielectrics: Confined micro-explosion". In: *Journal of Physics: Conference Series* 59 (2007), pp. 5–10. ISSN: 1742-6588. DOI: [10.1088/1742-6596/59/1/002](https://doi.org/10.1088/1742-6596/59/1/002).
- [Gam11] Eugene G. Gamaly. "The physics of ultra-short laser interaction with solids at non-relativistic intensities". In: *Physics Reports* 508.4-5 (2011), pp. 91–243. ISSN: 0370-1573. DOI: [10.1016/j.physrep.2011.07.002](https://doi.org/10.1016/j.physrep.2011.07.002).
- [GGP87] F Gori, G Guattari, and C Padovani. "Bessel-gauss beams". In: *Optics communications* 64.6 (1987), pp. 491–495.
- [Giu72] Concetto R. Giuliano. "Laser-induced damage in transparent dielectrics: ion beam polishing as a means of increasing surface damage thresholds". In: *Applied Physics Letters* 21.1 (1972), pp. 39–41. ISSN: 0003-6951. DOI: [10.1063/1.1654211](https://doi.org/10.1063/1.1654211).
- [Gle+96] EN Glezer et al. "Three-dimensional optical storage inside transparent materials". In: *Optics letters* 21.24 (1996), pp. 2023–2025. DOI: [10.1364/OL.21.002023](https://doi.org/10.1364/OL.21.002023).
- [GM08] Rafael R. Gattass and Eric Mazur. "Femtosecond laser micromachining in transparent materials". In: *Nature Photonics* 2.4 (2008), pp. 219–225. ISSN: 1749-4893. DOI: [10.1038/nphoton.2008.47](https://doi.org/10.1038/nphoton.2008.47).
- [GM98] E. N. Glezer and E. Mazur. "Ultrafast-laser driven micro-explosions in transparent materials". In: *Applied Physics Letters* 71.7 (1998), p. 882. ISSN: 0003-6951. DOI: [10.1063/1.119677](https://doi.org/10.1063/1.119677).
- [Gom22] Henry Gomersall. *PyFFTW*. 2022. URL: <https://github.com/pyFFTW/pyFFTW> (visited on 04/20/2022).
- [Goo17] Joseph W. Goodman. *Introduction to Fourier optics*. Fourth edition. New York: W.H. Freeman Macmillan Learning, 2017. ISBN: 1319119166.
- [Got13] J. Gottmann. "Microcutting and Hollow 3D Microstructures in Glasses by In-volume Selective Laser-induced Etching (ISLE)". In: *Journal of Laser Micro/Nanoengineering* 8.1 (2013), pp. 15–18. DOI: [10.2961/jlmm.2013.01.0004](https://doi.org/10.2961/jlmm.2013.01.0004).
- [Gri21] A. A. Griffith. "The Phenomena of Rupture and Flow in Solids". In: *Philosophical Transactions of the Royal Society A: Mathematical, Physical and Engineering Sciences* (1921). DOI: [10.1098/rsta.1921.0006](https://doi.org/10.1098/rsta.1921.0006).

- [Hen+16] F. Hendricks et al. "Time-resolved study of femtosecond laser induced micro-modifications inside transparent brittle materials". In: *Frontiers in Ultrafast Optics: Biomedical, Scientific, and Industrial Applications XVI*. Ed. by Alexander Heisterkamp et al. SPIE Proceedings. SPIE, 2016, 97401A. DOI: [10.1117/12.2214081](https://doi.org/10.1117/12.2214081).
- [HH12] S.A. Hosseini and P.R. Herman. *Method of material processing by laser filamentation*. Patent WO 2012/006736 A2. 2012.
- [HJM07] Tomohiro Hashimoto, Saulius Juodkazis, and Hiroaki Misawa. "Void formation in glasses". In: *New Journal of Physics* 9.8 (2007), p. 253. DOI: [10.1088/1367-2630/9/8/253](https://doi.org/10.1088/1367-2630/9/8/253).
- [Hna+06] C. Hnatovsky et al. "Fabrication of microchannels in glass using focused femtosecond laser radiation and selective chemical etching". In: *Applied Physics A* 84.1 (2006), pp. 47–61. ISSN: 0947-8396. DOI: [10.1007/s00339-006-3590-4](https://doi.org/10.1007/s00339-006-3590-4).
- [HOL22] HOLOEYE. *Spatial Light Modulators*. 2022. URL: <https://holoeye.com/spatial-light-modulators/> (visited on 04/20/2022).
- [HSS05] Jamie Harriman, Steve Serati, and Jay Stockley. "Comparison of transmissive and reflective spatial light modulators for optical manipulation applications". In: *Optical Trapping and Optical Micromanipulation II*. Ed. by Kishan Dholakia and Gabriel C. Spalding. SPIE Proceedings. SPIE, 2005, p. 59302D. DOI: [10.1117/12.619283](https://doi.org/10.1117/12.619283).
- [Hu+12] Y. Hu et al. "Self-accelerating Airy Beams: Generation, Control, and Applications". In: *Nonlinear Photonics and Novel Optical Phenomena*. Ed. by Zhigang Chen and Roberto Morandotti. Vol. 170. Springer Series in Optical Sciences. New York, NY: Springer New York, 2012, pp. 1–46. ISBN: 978-1-4614-3537-2. DOI: [10.1007/978-1-4614-3538-9_{_}1](https://doi.org/10.1007/978-1-4614-3538-9_{_}1).
- [IKM18] Isamu Miyamoto, Kristian Cvecek, and Michael Schmidt. "Nonlinear absorption dynamics simulated in internal modification of glass at 532nm and 1064nm by ultrashort laser pulses". In: *Procedia CIRP* 74 (2018), pp. 344–348. ISSN: 2212-8271. DOI: [10.1016/j.procir.2018.08.129](https://doi.org/10.1016/j.procir.2018.08.129).
- [Ito+06] Kazuyoshi Itoh et al. "Ultrafast processes for bulk modification of transparent materials". In: *MRS bulletin* 31.8 (2006), pp. 620–625. DOI: [10.1557/mrs2006.159](https://doi.org/10.1557/mrs2006.159).
- [Jen+20] M. Jenne et al. "Facilitated glass separation by asymmetric Bessel-like beams". In: *Optics Express* 28.5 (2020), pp. 6552–6564. DOI: [10.1364/OE.387545](https://doi.org/10.1364/OE.387545).
- [JSR18] Matthias Jotz, Jens Schneider, and Edda Raedlein. *Introducing the "Cylinder Fit Test", a simplified edge strength measurement method for Ultra Thin Glass in Engineered transparency 2018: Glass in architecture and structural engineering*. Ed. by Jens Schneider and Bernhard Weller. Berlin: Ernst & Sohn, 2018. ISBN: 3433032696. URL: <http://www.wiley-vch.de/publish/dt/books/ISBN978-3-433-03269-5/>.
- [Juo+06] Saulius Juodkazis et al. "Laser-induced microexplosion confined in a bulk of silica: Formation of nanovoids". In: *Applied Physics Letters* 88.20 (2006), p. 201909. ISSN: 0003-6951. DOI: [10.1063/1.2204847](https://doi.org/10.1063/1.2204847).
- [JW17] Yuhui Jin and Matthew Evan Wilhelm. *Glass-based substrate with vias and process of forming the same*. US Patent App. 15/286,803. 2017.
- [Kar+18] Thomas Karr et al. "Engineering equations for characterizing non-linear laser intensity propagation in air with loss". In: *Optics Express* 26.4 (2018), pp. 3974–3987. DOI: [10.1364/OE.26.003974](https://doi.org/10.1364/OE.26.003974).
- [Kaz+07] Peter G. Kazansky et al. "'Quill' writing with ultrashort light pulses in transparent materials". In: *Applied Physics Letters* 90.15 (2007), p. 151120. ISSN: 0003-6951. DOI: [10.1063/1.2722240](https://doi.org/10.1063/1.2722240).

- [Kel65] L. V. Keldysh. "Ionization in the field of a strong electromagnetic wave". In: *Sov. Phys. JETP* 20.5 (1965), pp. 1307–1314. URL: https://www.osapublishing.org/DirectPDFAccess/06FAACC3-F42B-4D3A-B2693ED00484CF7F_427695/oe-28-5-6552.pdf?da=1&id=427695&seq=0&mobile=no.
- [Ken95] P. K. Kennedy. "A first-order model for computation of laser-induced breakdown thresholds in ocular and aqueous media. I. Theory". In: *IEEE Journal of Quantum Electronics* 31.12 (1995), pp. 2241–2249. ISSN: 0018-9197. DOI: [10.1109/3.477753](https://doi.org/10.1109/3.477753).
- [Kiy+09] Satoshi Kiyama et al. "Examination of Etching Agent and Etching Mechanism on Femtosecond Laser Microfabrication of Channels Inside Vitreous Silica Substrates". In: *The Journal of Physical Chemistry C* 113.27 (2009), pp. 11560–11566. ISSN: 1932-7447. DOI: [10.1021/jp900915r](https://doi.org/10.1021/jp900915r).
- [Kum+07] Masayoshi Kumagai et al. "Advanced dicing technology for semiconductor wafer—stealth dicing". In: *IEEE Transactions on Semiconductor Manufacturing* 20.3 (2007), pp. 259–265. DOI: [10.1109/TSM.2007.901849](https://doi.org/10.1109/TSM.2007.901849).
- [Kum+14] M Kumkar et al. "Comparison of different processes for separation of glass and crystals using ultrashort pulsed lasers". In: *Proceedings of SPIE - The International Society for Optical Engineering* 8972 (2014). ISSN: 0277-786X. DOI: [10.1117/12.2044187](https://doi.org/10.1117/12.2044187).
- [Kun18] C. Kunisch. *FEM-Berechnung der plastischen Dehnung als Indikator für Risse, Internal report RDS-2018-018c*. 2018.
- [Kur+16] Satoru Kuramochi et al. "Glass interposer for advanced packaging solution". In: *2016 6th Electronic System-Integration Technology Conference (ESTC)*. IEEE. 2016, pp. 1–6. DOI: [10.1109/ESTC.2016.7764697](https://doi.org/10.1109/ESTC.2016.7764697).
- [LAS22] LASIT. *Picosecond laser: why it achieves what other lasers don't*. 2022. URL: <https://www.lasitlaser.com/laser-marking-picosecond/> (visited on 06/19/2022).
- [LAW11] D. J. Little, M. Ams, and M. J. Withford. "Influence of bandgap and polarization on photo-ionization: guidelines for ultrafast laser inscription [Invited]". In: *Optical Materials Express* 1.4 (2011), p. 670. DOI: [10.1364/OME.1.000670](https://doi.org/10.1364/OME.1.000670).
- [Liu+02] W. Liu et al. "Intensity clamping of a femtosecond laser pulse in condensed matter". In: *Optics Communications* 202.1 (2002), pp. 189–197. ISSN: 0030-4018. DOI: [https://doi.org/10.1016/S0030-4018\(01\)01698-4](https://doi.org/10.1016/S0030-4018(01)01698-4).
- [Liu+18] Xin Liu et al. "Front-surface fabrication of moderate aspect ratio micro-channels in fused silica by single picosecond Gaussian–Bessel laser pulse". In: *Applied Physics A* 124.2 (2018). ISSN: 0947-8396. DOI: [10.1007/s00339-018-1634-1](https://doi.org/10.1007/s00339-018-1634-1).
- [Lon+03] J. B. Lonzaga et al. "Color center formation in soda-lime glass with femtosecond laser pulses". In: *Journal of Applied Physics* 94.7 (2003), pp. 4332–4340. ISSN: 0021-8979. DOI: [10.1063/1.1603962](https://doi.org/10.1063/1.1603962).
- [Lop+t] John Lopez et al. "Glass cutting using ultrashort pulsed bessel beams". In: *ICALEO 2015: 34th International Congress on Laser Materials Processing, Laser Microprocessing and Nanomanufacturing*. Ed. by Silke Pflüger. Journal of laser applications ICALEO. Orlando, FL: Laser Institute of America, Oct. 1, 2015, pp. 60–69. ISBN: 978-1-940168-05-0. DOI: [10.2351/1.5063208](https://doi.org/10.2351/1.5063208).
- [Mar+01] A. Marcinkevičius et al. "Application of Bessel Beams for Microfabrication of Dielectrics by Femtosecond Laser". In: *Japanese Journal of Applied Physics* 40.Part 2, No. 11A (2001), pp. L1197–L1199. ISSN: 00214922. DOI: [10.1143/JJAP.40.L1197](https://doi.org/10.1143/JJAP.40.L1197).
- [Mat+09] Shigeki Matsuo et al. "Femtosecond laser-assisted etching of Pyrex glass with aqueous solution of KOH". In: *Applied surface science* 255.24 (2009), pp. 9758–9760.

- [Mat+12] A. Mathis et al. "Micromachining along a curve: Femtosecond laser micromachining of curved profiles in diamond and silicon using accelerating beams". In: *Applied Physics Letters* 101.7 (2012), p. 071110. ISSN: 0003-6951. DOI: [10.1063/1.4745925](https://doi.org/10.1063/1.4745925).
- [Mat+13a] A. Mathis et al. "Arbitrary nonparaxial accelerating periodic beams and spherical shaping of light". In: *Optics Letters* 38.13 (2013), pp. 2218–2220. DOI: [10.1364/OL.38.002218](https://doi.org/10.1364/OL.38.002218).
- [Mat+13b] Amaury Mathis et al. "Direct machining of curved trenches in silicon with femtosecond accelerating beams". In: *Journal of the European Optical Society-Rapid publications* 8 (2013). DOI: [10.2971/jeos.2013.13019](https://doi.org/10.2971/jeos.2013.13019).
- [Mau+16] C. Mauclair et al. "Excitation and relaxation dynamics in ultrafast laser irradiated optical glasses". In: *High Power Laser Science and Engineering* 4 (2016), p. 1065. ISSN: 2095-4719. DOI: [10.1017/hpl.2016.45](https://doi.org/10.1017/hpl.2016.45).
- [MB+08] A. Mermillod-Blondin et al. "Flipping the sign of refractive index changes in ultrafast and temporally shaped laser-irradiated borosilicate crown optical glass at high repetition rates". In: *Physical Review B* 77.10 (2008), p. 332. DOI: [10.1103/PhysRevB.77.104205](https://doi.org/10.1103/PhysRevB.77.104205).
- [MCS11] Isamu Miyamoto, Kristian Cvecek, and Michael Schmidt. "Evaluation of nonlinear absorptivity in internal modification of bulk glass by ultrashort laser pulses". In: *Optics Express* 19.11 (2011), pp. 10714–10727. DOI: [10.1364/OE.19.010714](https://doi.org/10.1364/OE.19.010714).
- [MD05] D. McGloin and K. Dholakia. "Bessel beams: Diffraction in a new light". In: *Contemporary Physics* 46.1 (2005), pp. 15–28. ISSN: 0010-7514. DOI: [10.1080/0010751042000275259](https://doi.org/10.1080/0010751042000275259).
- [Mey+17a] R. Meyer et al. "Submicron-quality cleaving of glass with elliptical ultrafast Bessel beams". In: *Applied Physics Letters* 111.23 (2017), p. 231108. ISSN: 0003-6951. DOI: [10.1063/1.5008921](https://doi.org/10.1063/1.5008921).
- [Mey+17b] Rémi Meyer et al. "Single-shot ultrafast laser processing of high-aspect-ratio nanochannels using elliptical Bessel beams". In: *Optics Letters* 42.21 (2017), pp. 4307–4310. DOI: [10.1364/OL.42.004307](https://doi.org/10.1364/OL.42.004307).
- [Mey+19] R. Meyer et al. "Extremely high-aspect-ratio ultrafast Bessel beam generation and stealth dicing of multi-millimeter thick glass". In: *Applied Physics Letters* 114.20 (2019), p. 201105. ISSN: 0003-6951. DOI: [10.1063/1.5096868](https://doi.org/10.1063/1.5096868).
- [Mic22] Microsoft. *Research background: Storage*. 2022. URL: <https://www.microsoft.com/en-us/research/group/optics-for-the-cloud/storage/> (visited on 06/19/2022).
- [Mil74] Ed Milton. *Abramowitz, Handbook of Mathematical Functions*. 1974.
- [Mis+16] Konstantin Mishchik et al. "Dash line glass- and sapphire-cutting with high power USP laser". In: *Frontiers in Ultrafast Optics: Biomedical, Scientific, and Industrial Applications XVI*. Ed. by Alexander Heisterkamp et al. SPIE Proceedings. SPIE, 2016, 97400W. DOI: [10.1117/12.2209274](https://doi.org/10.1117/12.2209274).
- [Mis+17] K. Mishchik et al. "Improved laser glass cutting by spatio-temporal control of energy deposition using bursts of femtosecond pulses". In: *Optics Express* 25.26 (2017), p. 33271. DOI: [10.1364/OE.25.033271](https://doi.org/10.1364/OE.25.033271).
- [Miu+98] K. Miura et al. "Optical waveguides induced in inorganic glasses by a femtosecond laser". In: *Nuclear Instruments and Methods in Physics Research Section B: Beam Interactions with Materials and Atoms* 141.1-4 (1998), pp. 726–732. ISSN: 0168583X. DOI: [10.1016/S0168-583X\(98\)00197-9](https://doi.org/10.1016/S0168-583X(98)00197-9).
- [MJ04] M. Kolesik and J. V. Moloney. "Nonlinear optical pulse propagation simulation: From Maxwell's to unidirectional equations". In: *Physical Review E* 70.3 (2004), p. 036604. DOI: [10.1103/PhysRevE.70.036604](https://doi.org/10.1103/PhysRevE.70.036604).

- [MJF14] Martin Hermans, Jens Gottmann, and Frank Riedel. "Selective, Laser-Induced Etching of Fused Silica at High Scan-Speeds Using KOH". In: *Journal of Laser Micro / Nanoengineering* 9.2 (2014). ISSN: 1880-0688. DOI: [10.2961/jlmn.2014.02.0009](https://doi.org/10.2961/jlmn.2014.02.0009).
- [MKM14] Miguel A. Preciado, Kishan Dholakia, and Michael Mazilu. "Generation of attenuation-compensating Airy beams". In: *Optics Letters* 39.16 (2014), pp. 4950–4953. ISSN: 1539-4794. DOI: [10.1364/OL.39.004950](https://doi.org/10.1364/OL.39.004950).
- [Nie+15] D. Nieto et al. "Single-pulse laser ablation threshold of borosilicate, fused silica, sapphire, and soda-lime glass for pulse widths of 500 fs, 10 ps, 20 ns". In: *Applied Optics* 54.29 (2015), pp. 8596–8601. DOI: [10.1364/AO.54.008596](https://doi.org/10.1364/AO.54.008596).
- [NLS13] S. Nisar, L. Li, and M. A. Sheikh. "Laser glass cutting techniques—A review". In: *Journal of Laser Applications* 25.4 (2013), p. 042010. ISSN: 1042-346X. DOI: [10.2351/1.4807895](https://doi.org/10.2351/1.4807895).
- [OI+16] Ismail Ouadghiri-Idrissi et al. "Arbitrary shaping of on-axis amplitude of femtosecond Bessel beams with a single phase-only spatial light modulator". In: *Optics Express* 24.11 (2016), pp. 11495–11504. DOI: [10.1364/OE.24.011495](https://doi.org/10.1364/OE.24.011495).
- [Ort+18a] Andreas Ortner et al. *Structured plate-like glass element and process for the production thereof*. US Patent App. 15/882,187. 2018.
- [Ort+18b] Andreas Ortner et al. *Strukturiertes plattenförmiges Glaselement und Verfahren zu dessen Herstellung*. German Patent DE 10 2018 100 299 A1. 2018.
- [Osi+10] Vladimir Osipov et al. "Realization of binary radial diffractive optical elements by two-photon polymerization technique". In: *Optics Express* 18.25 (2010), pp. 25808–25814. DOI: [10.1364/OE.18.025808](https://doi.org/10.1364/OE.18.025808).
- [Pan+13] P. Panagiotopoulos et al. "Sharply autofocused ring-Airy beams transforming into non-linear intense light bullets". In: *Nature Communications* 4 (2013), p. 2622. DOI: [10.1038/ncomms3622](https://doi.org/10.1038/ncomms3622).
- [Pap+10] D. G. Papazoglou et al. "Tunable intense Airy beams and tailored femtosecond laser filaments". In: *Physical Review A* 81.6 (2010), p. 061807. DOI: [10.1103/PhysRevA.81.061807](https://doi.org/10.1103/PhysRevA.81.061807).
- [PEG12] Martin Persson, David Engström, and Mattias Goksör. "Reducing the effect of pixel crosstalk in phase only spatial light modulators". In: *Optics Express* 20.20 (2012), pp. 22334–22343. DOI: [10.1364/OE.20.022334](https://doi.org/10.1364/OE.20.022334).
- [PN87] K. K. Phani and S. K. Niyogi. "Young's modulus of porous brittle solids". In: *Journal of Materials Science* 22.1 (1987), pp. 257–263. ISSN: 1573-4803. DOI: [10.1007/BF01160581](https://doi.org/10.1007/BF01160581).
- [Pol+09] P. Polynkin et al. "Curved plasma channel generation using ultraintense Airy beams". In: *Science* 324.5924 (2009), pp. 229–232. DOI: [10.1126/science.1169544](https://doi.org/10.1126/science.1169544).
- [Pol22] Mikhail Polyanskiy. *Refractive index database*. 2022. URL: <https://refractiveindex.info/?shelf=glass&book=SCHOTT-multipurpose&page=BOROFLOAT33> (visited on 04/04/2022).
- [Pre+07] William H. Press et al. *Numerical Recipes 3rd Edition: The Art of Scientific Computing*. Cambridge University Press, 2007. ISBN: 9780521880688.
- [Qua+06] Sun Quan et al. "Relaxation of dense electron plasma induced by femtosecond laser in dielectric materials". In: *Chinese Physics Letters* 23.1 (2006), p. 189. DOI: [10.1088/0256-307X/23/1/055](https://doi.org/10.1088/0256-307X/23/1/055).
- [RAG18] Raghvinder S. Grewal, Anirban Ghosh, and G. K. Samanta. "Simultaneous generation of high-power, ultrafast 1D and 2D Airy beams and their frequency-doubling characteristics". In: *Optics Letters* 43.16 (2018), pp. 3957–3960. ISSN: 1539-4794. DOI: [10.1364/OL.43.003957](https://doi.org/10.1364/OL.43.003957).

- [Rao+18] S. Lakshmi Srinivasa Rao et al. "Optical properties of alkaline earth borate glasses". In: *International Journal of Engineering, Science and Technology* 4.4 (2018), pp. 25–35. ISSN: 2141-2820. DOI: [10.4314/ijest.v4i4.3](https://doi.org/10.4314/ijest.v4i4.3).
- [Ret+17] Baerbel Rethfeld et al. "Modelling ultrafast laser ablation". In: *Journal of Physics D: Applied Physics* 50.19 (2017), p. 193001. ISSN: 0022-3727. DOI: [10.1088/1361-6463/50/19/193001](https://doi.org/10.1088/1361-6463/50/19/193001).
- [Ret04] Baerbel Rethfeld. "Unified Model for the Free-Electron Avalanche in Laser-Irradiated Dielectrics". In: *Physical Review Letters* 92.18 (2004), p. 187401. ISSN: 0031-9007. DOI: [10.1103/PhysRevLett.92.187401](https://doi.org/10.1103/PhysRevLett.92.187401).
- [Ret06] Baerbel Rethfeld. "Free-electron generation in laser-irradiated dielectrics". In: *Physical Review B* 73.3 (2006), p. 035101. DOI: [10.1103/PhysRevB.73.035101](https://doi.org/10.1103/PhysRevB.73.035101).
- [RHD13] James D. Ring, Christopher J. Howls, and Mark R. Dennis. "Incomplete Airy beams: finite energy from a sharp spectral cutoff". In: *Optics Letters* 38.10 (2013), pp. 1639–1641. DOI: [10.1364/OL.38.001639](https://doi.org/10.1364/OL.38.001639).
- [RNT12] Sören Richter, Stefan Nolte, and Andreas Tünnermann. "Ultrashort pulse laser welding—a new approach for high-stability bonding of different glasses". In: *Physics Procedia* 39 (2012), pp. 556–562. DOI: [10.1016/j.phpro.2012.10.073](https://doi.org/10.1016/j.phpro.2012.10.073).
- [Sak+11] Masaaki Sakakura et al. "Observation of laser-induced stress waves and mechanism of structural changes inside rock-salt crystals". In: *Optics Express* 19.18 (2011), pp. 17780–17789. DOI: [10.1364/OE.19.017780](https://doi.org/10.1364/OE.19.017780).
- [San+10] N. Sanner et al. "Toward determinism in surface damaging of dielectrics using few-cycle laser pulses". In: *Applied Physics Letters* 96.7 (2010), p. 071111. ISSN: 0003-6951. DOI: [10.1063/1.3309700](https://doi.org/10.1063/1.3309700).
- [Sar+19] Clara J Saraceno et al. "The amazing progress of high-power ultrafast thin-disk lasers". In: *Journal of the European Optical Society-Rapid Publications* 15.1 (2019), pp. 1–7.
- [SC07] Georgios A. Siviloglou and Demetrios N. Christodoulides. "Accelerating finite energy Airy beams". In: *Optics Letters* 32.8 (2007), pp. 979–981. DOI: [10.1364/ol.32.000979](https://doi.org/10.1364/ol.32.000979).
- [Sch17] Jonas Schatz. "Structural Changes of Laser Processed Glass". MA thesis. Friedrich-Alexander-Universität Erlangen-Nürnberg, 2017.
- [Sch21] Wiebke Schöttler. "Absorption von UKP-Laserstrahlung in Borosilikatglas in Abhängigkeit von Pulsdauer und Strahlform". MA thesis. Hochschule für angewandte Wissenschaft und Kunst Hildesheim/ Holzminden/ Göttingen, 2021.
- [Sei+14] A. Seidl et al. *Trennen von Glas mittels Pikosekunden-Laserstrahlung, Teil I: Modellierung und Simulation, Internal report 2014/019*. 2014.
- [Shi+03] Yasuhiko Shimotsuma et al. "Self-organized nanogratings in glass irradiated by ultrashort light pulses". In: *Physical review letters* 91.24 (2003), p. 247405. DOI: [10.1103/PhysRevLett.91.247405](https://doi.org/10.1103/PhysRevLett.91.247405).
- [Siv+07] G. A. Siviloglou et al. "Observation of accelerating Airy beams". In: *Physical Review Letters* 99.21 (2007), p. 213901. DOI: [10.1103/PhysRevLett.99.213901](https://doi.org/10.1103/PhysRevLett.99.213901).
- [Sku05] Stefan Skupin. *Nonlinear Dynamics of Trapped Beams (PhD thesis)*. 2005.
- [SM02] S. K. Sundaram and E. Mazur. "Inducing and probing non-thermal transitions in semiconductors using femtosecond laser pulses". In: *Nature Materials* 1.4 (2002), pp. 217–224. ISSN: 1476-4660. DOI: [10.1038/nmat767](https://doi.org/10.1038/nmat767).
- [Soc+92] J. Sochacki et al. "Nonparaxial design of generalized axicons". In: *Applied Optics* 31.25 (1992), pp. 5326–5330. DOI: [10.1364/AO.31.005326](https://doi.org/10.1364/AO.31.005326).

- [SS+16] Andreas Schmitt-Sody et al. "Picosecond laser filamentation in air". In: *New Journal of Physics* 18.9 (2016), p. 093005. DOI: [10.1088/1367-2630/18/9/093005](https://doi.org/10.1088/1367-2630/18/9/093005).
- [SS09] Dariush Souri and Kobra Shomalian. "Band gap determination by absorption spectrum fitting method (ASF) and structural properties of different compositions of (60-x) V₂O₅-40TeO₂-xSb₂O₃ glasses". In: *Journal of Non-Crystalline Solids* 355.31-33 (2009), pp. 1597-1601. ISSN: 00223093. DOI: [10.1016/j.jnoncrysol.2009.06.003](https://doi.org/10.1016/j.jnoncrysol.2009.06.003).
- [ST01] Bahaa E. A. Saleh and Malvin Carl Teich. *Fundamentals of photonics*. Wiley Series in Pure and Applied Optics. Hoboken, NJ: Wiley-Interscience, 2001. ISBN: 0471213748. DOI: [10.1002/0471213748](https://doi.org/10.1002/0471213748).
- [Stu+96] B. C. Stuart et al. "Nanosecond-to-femtosecond laser-induced breakdown in dielectrics". In: *Physical Review B* 53.4 (1996), pp. 1749-1761. DOI: [10.1103/PhysRevB.53.1749](https://doi.org/10.1103/PhysRevB.53.1749).
- [Sud+02] L. (1) Sudrie et al. "Femtosecond Laser-Induced Damage and Filamentary Propagation in Fused Silica." In: *Physical Review Letters* 89.18 (2002). ISSN: 10797114. DOI: [10.1103/PhysRevLett.89.186601](https://doi.org/10.1103/PhysRevLett.89.186601).
- [Sud+99] L. Sudrie et al. "Writing of permanent birefringent microlayers in bulk fused silica with femtosecond laser pulses". In: *Optics Communications* 171.4 (1999), pp. 279-284. ISSN: 00304018. DOI: [10.1016/S0030-4018\(99\)00562-3](https://doi.org/10.1016/S0030-4018(99)00562-3).
- [Sun+12] Mingying Sun et al. "Laser ablation mechanism of transparent dielectrics with picosecond laser pulses". In: *Laser-Induced Damage in Optical Materials: 2012*. Ed. by Gregory J. Exarhos et al. SPIE Proceedings. SPIE, 2012, p. 853007. DOI: [10.1117/12.976062](https://doi.org/10.1117/12.976062).
- [Sun+13a] Mingying Sun et al. "Numerical analysis of laser ablation and damage in glass with multiple picosecond laser pulses". In: *Optics Express* 21.7 (2013), pp. 7858-7867. DOI: [10.1364/OE.21.007858](https://doi.org/10.1364/OE.21.007858).
- [Sun+13b] Mingying Sun et al. "Role of thermal ionization in internal modification of bulk borosilicate glass with picosecond laser pulses at high repetition rates". In: *Optical Materials Express* 3.10 (2013), p. 1716. DOI: [10.1364/OME.3.001716](https://doi.org/10.1364/OME.3.001716).
- [TGV66] J. Tauc, R. Grigorovici, and A. Vancu. "Optical Properties and Electronic Structure of Amorphous Germanium". In: *physica status solidi (b)* 15.2 (1966), pp. 627-637. ISSN: 03701972. DOI: [10.1002/pssb.19660150224](https://doi.org/10.1002/pssb.19660150224).
- [UL21] Craig Ungaro and Anping Liu. "Single-pass cutting of glass with a curved edge using ultrafast curving bessel beams and oblong airy beams". In: *Optics & Laser Technology* 144 (2021), p. 107398. ISSN: 00303992. DOI: [10.1016/j.optlastec.2021.107398](https://doi.org/10.1016/j.optlastec.2021.107398).
- [Vel+16] P. K. Velpula et al. "Spatio-temporal dynamics in nondiffractive Bessel ultrafast laser nanoscale volume structuring". In: *Laser & Photonics Reviews* 10.2 (2016), pp. 230-244. ISSN: 18638880. DOI: [10.1002/lpor.201500112](https://doi.org/10.1002/lpor.201500112).
- [Wer+20] Ferdinand Werr et al. "Surface Probing of Ultra-Short-Pulse Laser Filament Cut Window Glass and the Impact on the Separation Behavior". In: *Advanced Engineering Materials* 22.9 (2020), p. 2000471. ISSN: 1527-2648. DOI: [10.1002/adem.202000471](https://doi.org/10.1002/adem.202000471).
- [Yan+14] Z. Yang et al. "A compact Airy beam light sheet microscope with a tilted cylindrical lens". In: *Biomedical Optics Express* 5.10 (2014), pp. 3434-3442. ISSN: 2156-7085. DOI: [10.1364/BOE.5.003434](https://doi.org/10.1364/BOE.5.003434).
- [Zan+20] Alessandro Zannotti et al. "Shaping caustics into propagation-invariant light". In: *Nature Communications* 11.1 (2020), pp. 1-7. ISSN: 2041-1723. DOI: [10.1038/s41467-020-17439-3](https://doi.org/10.1038/s41467-020-17439-3).
- [Zha+13] J. Zhao et al. "Observation of self-accelerating Bessel-like optical beams along arbitrary trajectories". In: *Optics Letters* 38.4 (2013), pp. 498-500. DOI: [10.1364/OL.38.000498](https://doi.org/10.1364/OL.38.000498).

- [Zha+18] Yong Zha et al. "Elliptical airy beam". In: *Applied Optics* 57.23 (2018), pp. 6717–6720.
- [ZR04] Michel Zamboni-Rached. "Stationary optical wave fields with arbitrary longitudinal shape by superposing equal frequency Bessel beams: Frozen Waves". In: *Optics Express* 12.17 (2004), pp. 4001–4006. DOI: [10.1364/opex.12.004001](https://doi.org/10.1364/opex.12.004001).
- [ZZW14] Chunyang Zhao, Hongzhi Zhang, and Yang Wang. "Semiconductor laser asymmetry cutting glass with laser induced thermal-crack propagation". In: *Optics and Lasers in Engineering* 63 (2014), pp. 43–52. ISSN: 01438166. DOI: [10.1016/j.optlaseng.2014.06.008](https://doi.org/10.1016/j.optlaseng.2014.06.008).
- [3D] 3D Micromac AG. *FSLATM – Flow Supported Laser Ablation*.
- [LPK21] LPKF Vitron. *Micromachining of Glass by Laser Induced Deep Etching (LIDE) - LPKF Vitron® 5000*. 2021. URL: https://jp.lpkf.com/_mediafiles/3763-lpkf-vitron-5000-en.pdf (visited on 04/14/2021).
- [Lig21] LightFab. *SLE-Prozess with LightFab 3D printer*. 2021. URL: https://lightfab.de/files/Downloads/LightFab_DS_SLE.pdf (visited on 04/14/2021).
- [Nip22] Nippon Electric Glass. *G-LeafTM (Ultra-thin Glass)*. 2022. URL: <https://www.neg.co.jp/en/product/dp/g-leaf> (visited on 06/19/2022).
- [SCH22a] SCHOTT AG. *AMIRAN®*. 2022. URL: <https://www.schott.com/en-gb/products/amiran-p1000309/technical-details> (visited on 06/19/2022).
- [SCH22b] SCHOTT AG. *BOROFLOAT® 33 – Mechanical Data*. 2022. URL: https://www.schott.com/en-sk/products/borofloat/-/media/project/onex/products/b/borofloat/downloads/borofloat33_mech_eng_web.pdf?rev=cc822d289e1941ae9de8bf5e72f667de (visited on 05/08/2022).
- [SCH22c] SCHOTT AG. *BOROFLOAT® 33 – Optical Properties*. 2022. URL: <https://media.schott.com/api/public/content/cda43a92330145c9b34db0373098ec32?v=5f61fa28&download=false> (visited on 03/28/2022).
- [SCH22d] SCHOTT AG. *BOROFLOAT® 33 – Thermal Data*. 2022. URL: https://www.schott.com/en-cz/products/borofloat/-/media/project/onex/products/b/borofloat/downloads/borofloat33_therm_eng_web.pdf?rev=210bf6d3f9824bf1a90e85c5a5115c46e (visited on 03/28/2022).
- [SCH22e] SCHOTT AG. *D 263® - Technical Details*. 2022. URL: <https://www.schott.com/de-de/products/d-263-p1000318/technical-details> (visited on 06/19/2022).
- [SCH22f] SCHOTT AG. *FLEXINITY®*. 2022. URL: <https://www.schott.com/en-gb/products/flexinity-p1000320> (visited on 06/19/2022).
- [SCH22g] SCHOTT AG. *Glass Micro Bonding by SCHOTT Primoceler*. 2022. URL: <https://www.schott.com/en-gb/products/glass-micro-bonding-by-schott-primoceler-p1000278> (visited on 06/19/2022).
- [SCH22h] SCHOTT AG. *SCHOTT UTG® for foldable displays*. 2022. URL: <https://www.schott.com/en-gb/applications/schott-utg-for-foldable-displays> (visited on 06/19/2022).
- [Swi17] Swift Glass. *5 Common Glass Edge Types*. 2017. URL: <https://www.swiftglass.com/blog/glass-edge-types/> (visited on 06/19/2022).

Patent applications submitted during this project

- [Kog+20] Andreas Koglbauer et al. *Waveguide And Method For Producing A Waveguide*. Patent Application WO21259926 A1. 2020.

- [Ort+20] Andreas Ortner et al. *Glass element with structured wall and method for the production thereof*. German Patent Application DE102020126856. 2020.
- [Ort+22a] Andreas Ortner et al. *Method of structuring a glass element and structured glass element produced thereby*. US Patent Application 2022/0176494 A1. 2022.
- [Ort+22b] Andreas Ortner et al. *Verfahren und Vorrichtung zum Bearbeiten von Werkstücken*. German Patent Application DE102022115711.3. 2022.
- [OST20] Andreas Ortner, David Sohr, and Jens Ulrich Thomas. *Substrate Body And Method For Structuring The Surface Of A Substrate Body*. European Patent Application EP3964323 A1. 2020.
- [SKN20] David Sohr, Clemens Kunisch, and Kurt Nattermann. *Method Of Separating A Glass Element And Partial Glass Element*. European Patent Application EP3872041 A1. 2020.
- [SWO20] David Sohr, Fabian Wagner, and Andreas Ortner. *Substrate Element And Method For Preparing And / Or Performing The Separation Of A Substrate Element*. European Patent Application EP3875436 A1. 2020.

Peer reviewed publications

- [STS21c] David Sohr, Jens Ulrich Thomas, and Stefan Skupin. "Shaping convex edges in borosilicate glass by single pass perforation with an Airy beam". In: *Optics Letters* 46.10 (2021), pp. 2529–2532. DOI: [10.1364/OL.423788](https://doi.org/10.1364/OL.423788).
- [STS22a] David Sohr, Jens Ulrich Thomas, and Stefan Skupin. "All-Round: Novel approaches for combining laser cutting and edge shaping of glass". In: *Eur. Phys. J. Spec. Top "Ultrafast Phenomena from attosecond to picosecond timescales: theory and experiments"* (2022). Accepted for publication.

Conference contributions

- [Soh+21] David Sohr et al. "Combining glass cutting and edge shaping by using optical Airy beams". In: *Laser Applications Conference*. Washington, D.C.: OSA, 2021, LW3B.1. DOI: [10.1364/LAC.2021.LW3B.1](https://doi.org/10.1364/LAC.2021.LW3B.1).
- [STS21a] David Sohr, Jens Ulrich Thomas, and Stefan Skupin. "Airy beam enables single pass curved in-volume modifications and cutting of borosilicate glass". In: *2021 Conference on Lasers and Electro-Optics Europe & European Quantum Electronics Conference (CLEO/Europe-EQEC)*. IEEE, 2021. DOI: [10.1109/cleo/europe-eqec52157.2021.9542323](https://doi.org/10.1109/cleo/europe-eqec52157.2021.9542323).
- [STS21b] David Sohr, Jens Ulrich Thomas, and Stefan Skupin. *Cutting of glass with an Airy Beam [Invited]*. 28th International Conference on Advanced Laser Technologies. 2021.
- [STS22b] David Sohr, Jens Ulrich Thomas, and Stefan Skupin. *Rounded glass edges produced with an optical Airy beam*. 26th International Congress on Glass, DGG. 2022.
- [STS22c] David Sohr, Jens Ulrich Thomas, and Stefan Skupin. "Using airy beams for combined glass cutting and edge shaping". In: *Laser-based Micro- and Nanoprocessing XVI*. Ed. by Rainer Kling and Akira Watanabe. SPIE, 2022. DOI: [10.1117/12.2609576](https://doi.org/10.1117/12.2609576).
- [TSS22] Jens Ulrich Thomas, David Sohr, and Stefan Skupin. *Optimized Airy-Beams for round glass edge cutting [Invited]*. Stuttgarter Lasertage. 2022.

Appendix A

Preliminary results with aspheres

In the experiments that were the first to be conducted, we used aspheres (Thorlabs AL1210, AL2018, AL1225) to focus the laser beam instead of microscope objectives. In this section we will discuss these first results because they demonstrate the impact of aberrations on the Airy beam. Note that the laser used for micro machining results shown in this section is a Coherent HyperRapid, different to the results presented in the main text. Note also that many experimental results in this section were produced with minimal distance between DOE and lens and not in $2f$ configuration.

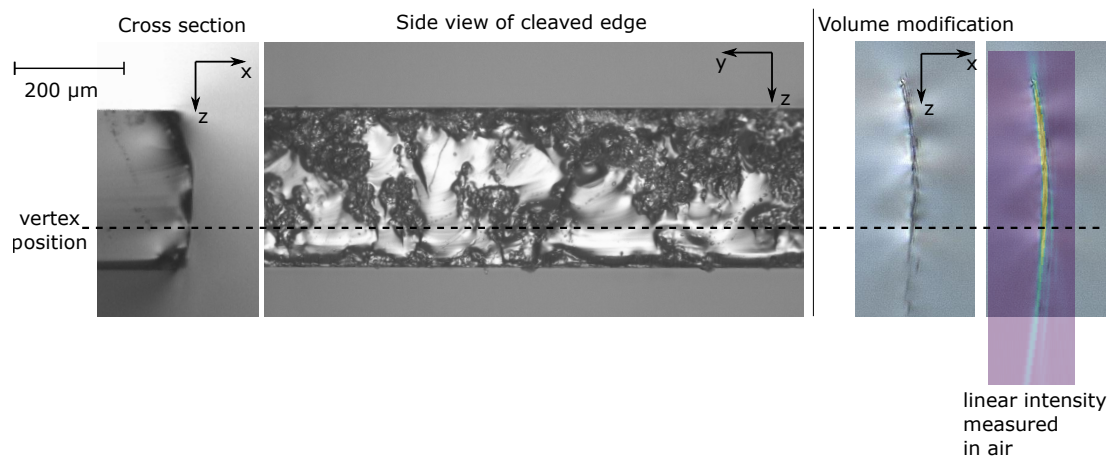


FIGURE A.1: Mechanical cleaving result after laser structuring with asphere (Thorlabs AL1210) as focusing optics together with the corresponding volume modifications and the linear intensity profile measured in air. Note the strong concoidal fracture and the fragmented volume modification, in particular beneath the parabolic vertex. See text and Fig. A.2 for more details.

Although we were able to separate a $300\ \mu\text{m}$ thick Borofloat glass sheet using AL1210 with $f = 10\ \text{mm}$, see Fig. A.1), the edge was very rough and showed extensive concoidal fracture surfaces. This corresponds to a fragmented glass modification observed in cross section and a linear intensity profile in air with strong side lobes. The morphology of volume modifications at different focal depths within the glass sheet is invariant nearly up to the surface, see Fig. A.2. This means non linear effects along the propagation in front of the modification (e.g. the Kerr effect) are negligible at the scale that can be resolved for these focusing conditions. This finding has later been confirmed by numerical simulations, see Fig. 4.15.

For the lens AL2018 we did observe a split of the modification into two larger segments, as demonstrated in Fig. A.3. As this was observed also for the surface ablation pattern this has to be a feature of the linear propagation.

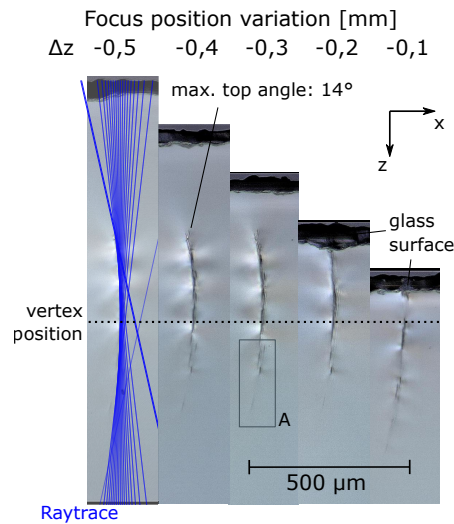


FIGURE A.2: Cross section views in light microscopy of Airy modifications in BF33 for varying focal position. The Airy beam was focussed with an asphere (Thorlabs AL1210) with $f = 10 \text{ mm}$, $w_0 = \text{mm}$, 4 pulse burst with $t_p = 10 \text{ ps}$ and $E_{\text{burst}} = 135 \mu\text{J}$. Beneath the vertex of the Airy parabola, the modification is strongly fragmented (A).

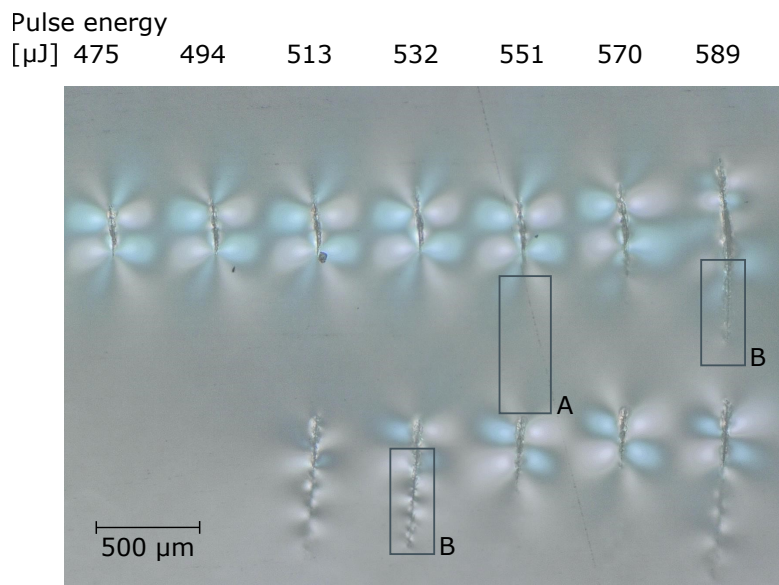


FIGURE A.3: Cross section views in light microscopy of Airy modifications in BF33 for varying pulse energy with focal length = 18 mm , beam diameter = 8.75 mm , 4 pulse burst, pulse duration = 10 ps and $\Delta z = -2.5 \text{ mm}$. Instead of a continuous parabolic trajectory, there are two consistent focal segments separated by a gap around the expected vertex (A). Occasional, apparently randomly distributed extensions occur in both upper and lower modification segments (B).

Appendix B

Image Analysis

The workflow of the image analysis algorithm used for detection of volume modifications is shown in Fig. B.1 and the corresponding parameters used in this work are given in Tab. B.1. For strong modifications also the minimum pixel value may be used for the line selection instead of the position of the minimum value, also see Fig. B.2, but this proved to be less reliable, especially for the weaker modifications at lower energies. For the weakest modifications that could be picked out by eye also the spatial selection algorithm failed, see Fig. B.3.

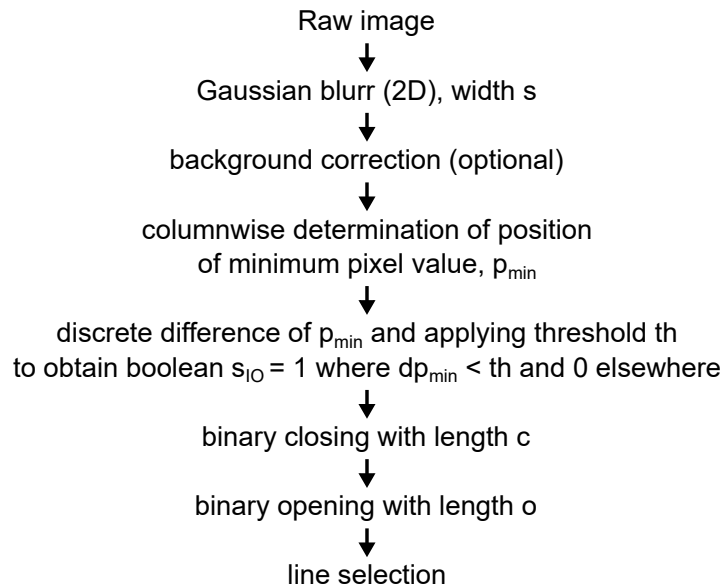


FIGURE B.1: Workflow of image analysis algorithm used for detection of volume modifications.

Parameter	value	unit
Gaussian blurr width s	1	px
threshold th	5	px value
opening length o	24	px
closing length c	8	px

TABLE B.1: Parameters used for image analysis workflow as shown in Fig. B.1.

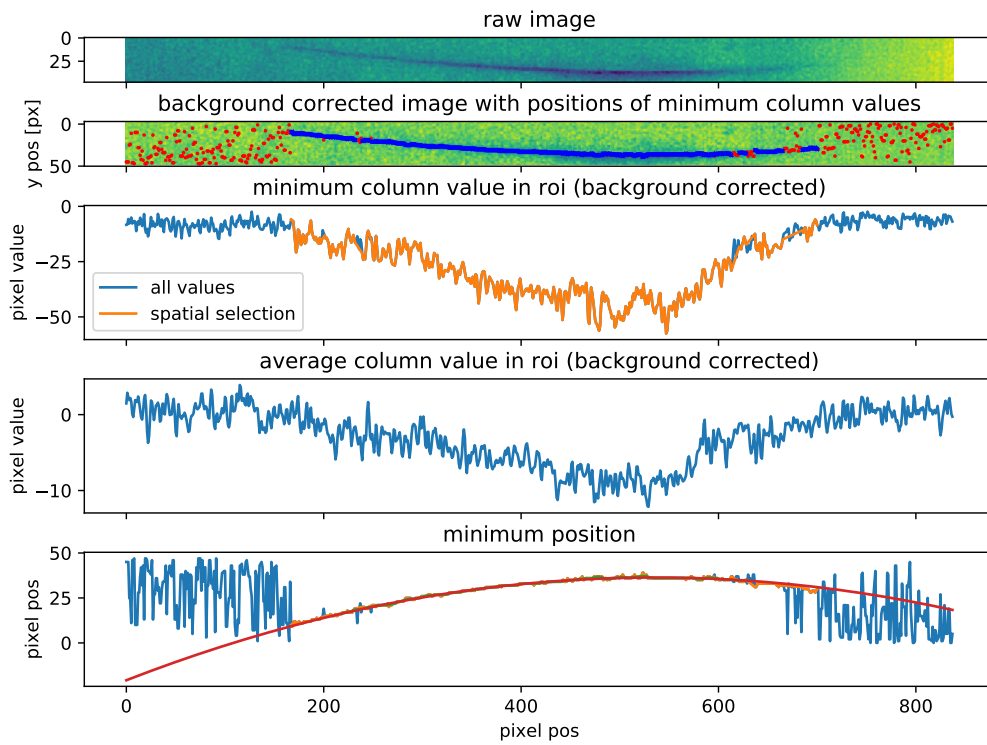


FIGURE B.2: Image analysis for Airy modification with $E_p = 380 \mu\text{J}$.

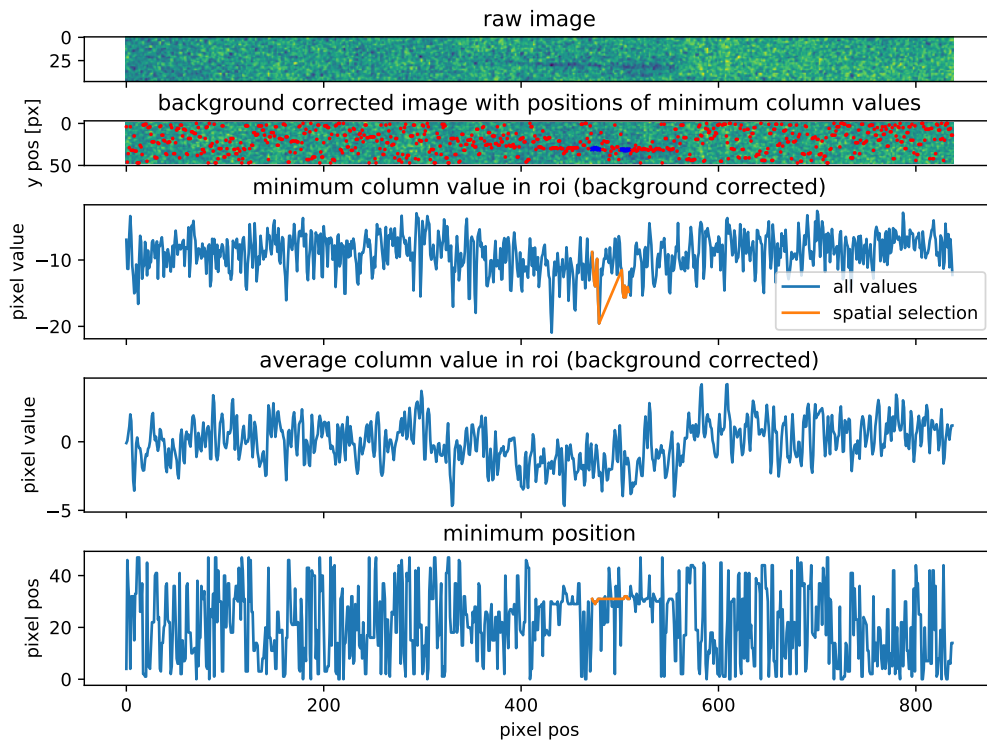


FIGURE B.3: Image analysis for Airy modification with $E_p = 114 \mu\text{J}$.

Appendix C

Calibrating the effective electron collision time

We find that an asymmetry in the simulated energy losses of the laser pulse during propagation that qualitatively corresponds to the asymmetry that we see in experimental results. The energy losses of the pulse versus propagation distance correspond to the energy per volume that is deposited within the material, integrated over each transversal slice respectively, giving thus a line density of deposited energy. The asymmetry seen for this line energy density distribution strongly depends on the choice of the effective electron collision time τ_c , as shown in Fig. C.1 (b). This is in line with previous statement that the asymmetry is principally caused by plasma effects. Typical literature values of the electron collision time are in the low fs regime, ranging from 0.1 to 23 fs in glasses with a rather large uncertainty [Sun+12; Epp+12; Sud+02]. In fact, already assuming a constant electron collision time is a rather crude approximation, also see Sec. 2.4.1. Nevertheless, the sensitivity of the deposited energy density on the collision time τ_c in our model can be used to constrain this parameter. Assuming that the line energy density scales linearly with the extent of damage that we see in microscope cross section, we compared the experimentally observed morphology of the Airy beam in combination with our non-linear simulations and found a rather good quantitative agreement for $\tau_c = 20$ fs. While this is relatively high compared to the values that are mostly used in previous literature, this value was used for all further simulations in this work.

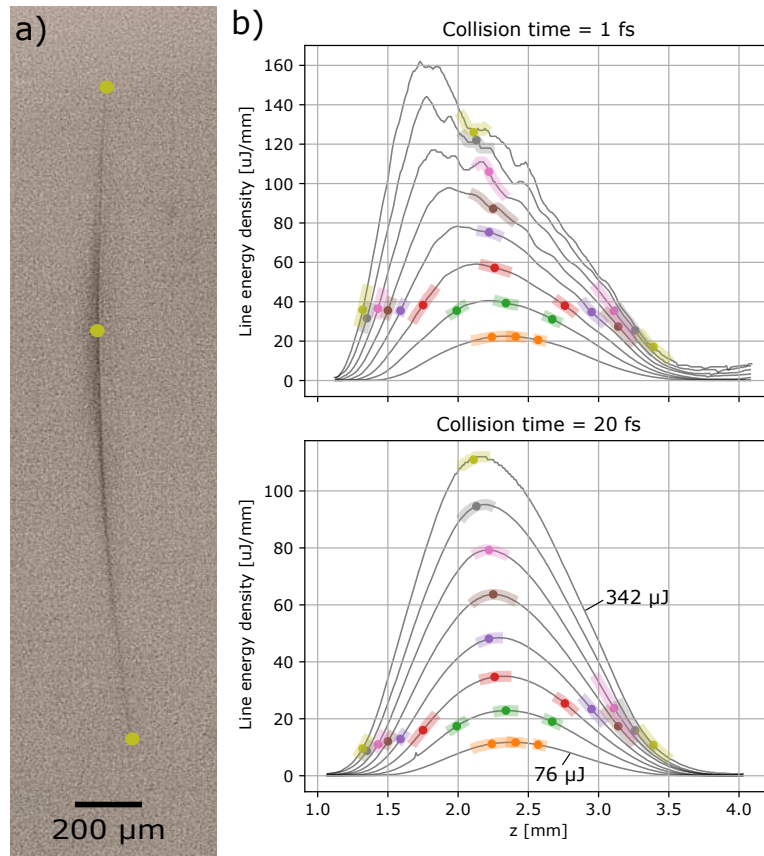


FIGURE C.1: Longitudinal cross section of volume modification (a) for $f = 20$ mm, $t_p = 10$ ps and $E_p = 342$ J with the ends and the maximum indicated by yellow dots. These characteristic points are also marked on the graphs of the energy loss or line density of deposited energy (b) for various pulse energies and two values of the assumed collision time. The error of determining the position on the microscope image is shown as a broad bar. The longer collision time $\tau_c = 20$ fs yields good agreement, with the energy density at the ends being nearly constant across all pulse energies and the energy density maxima occurring at the positions of maximum damage.

Appendix D

Curved Beams

D.1 Multispot

The maximum curvature and edge angles of the non-diffracting beams and their relatives presented is limited by the NA of the focussing optics. No angles above the NA within the target material can be reached. A completely different approach for defining a curved - or indeed an arbitrary - laser damage surface for separation consists in defining this surface by a multitude of focal spots, that are created with a phase mask by a multiplexing scheme [Fla+19]: The extra phase contribution for each spot at position (p_x, p_y, p_z) behind a lens with focal length f relative to the focal spot without an extra phase respectively is given by

$$\phi(x, y) = \phi_{\text{bg}} + \phi_{\text{lens}} + \phi_0 = (k_x x + k_y y) + (k_0(x^2 + y^2)/(2f_{\text{def}})) + \phi_0 \quad (\text{D.1})$$

where the blazed grating phase ϕ_{bg} creates the transversal displacement according to $k_x = \sin(\tan(p_x/f))$, similarly for y , and the additional lens term ϕ_{lens} , with a defocus focal length $f_{\text{def}} = -f^2/p_z$, see also Eq. 3.12 and Eq. 3.14, and an individual constant phase offset ϕ_0 . The total complex transmission for j spots is then calculated as

$$T(x, y) = \sum_j^{j_{\text{max}}} T_j = \sum_j^{j_{\text{max}}} \exp[i\phi_j(x, y)] = A_{\text{tot}}(x, y) \exp[i\phi_{\text{tot}}(x, y)]. \quad (\text{D.2})$$

The complex valued transmission $T(x, y)$ is subsequently reduced to a phase only modulation by simply neglecting the amplitude modulation and setting $A_{\text{tot}}(x, y) = 1$. This negatively affects the uniformity of the focal spots, but [Fla+19] report, that this can be satisfyingly be compensated by adjusting the individual phase offsets ϕ_0 of the spot contributions by an iterative optimization routine.

An application [Fla+22] of this multiplexing scheme to a curved profile and the resulting volume modifications are shown in Fig. D.1. While the high edge angles obtained by this method make it a very interesting candidate for glass cutting, the elongation of the focal spots along the propagation direction, which is determined by Gaussian optics, poses a particular challenge for mechanical separation as the crack will tend to run into the convex edge, along the orientation of the focal spots.

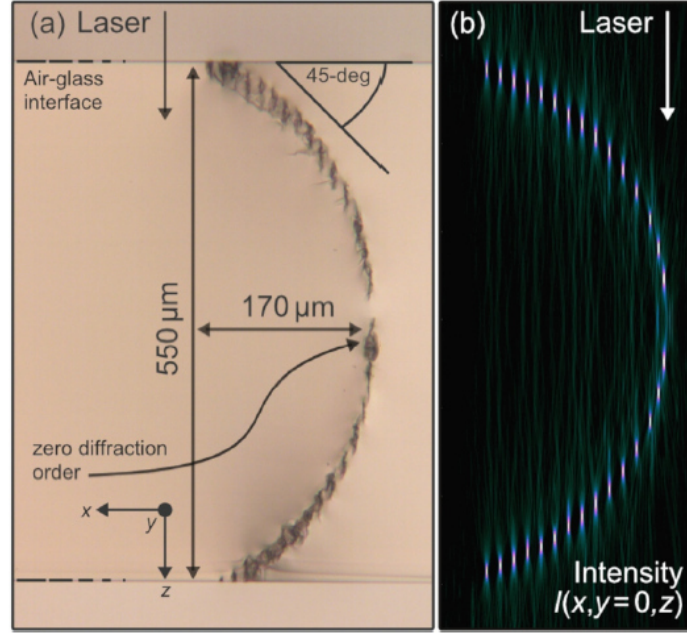


FIGURE D.1: Cross section view of volume glass modifications (a) induced by a multi spot intensity distribution (b) [Fla+22].

D.2 Accelerated Bessel

An arbitrary focal trajectory $\mathbf{p}(z) = (p_x(z), p_y(z))$ can be created by a beam shaping method, that relies on conical contribution to the a given point on this trajectory, similar to a Bessel beam, see Fig. D.2. The theoretical method for constructing such an accelerate Bessel beam was proposed in 2012 [Chr+12], which was rapidly followed by its experimental demonstration [Zha+13] and the theoretical extension to non-paraxial beams in 2013 [CE13]. The phase mask is constructed by a mapping of a given point of the trajectory to a locus that is defined by the intersection of a cone, whose rotation axis is tangent to the trajectory $\mathbf{p}(z)$ at the chosen depth, and the input plane. Avoiding an overlap of different cone sections limits the curvature of $\mathbf{p}(z)$. With $p_y(z) = 0$ for a beam that remains in one plane, the limiting condition

$$\frac{\partial^2 p_x}{\partial z^2} < \frac{\gamma}{z} \quad (\text{D.3})$$

for a Bessel cone angle γ . Choosing a large γ seems favorable, as it both allows larger curvatures and enables harder focussing. However, here the NA of the focussing optics is the main limiting factor, specifically

$$\frac{\partial p_x}{\partial z} + \gamma < NA. \quad (\text{D.4})$$

In practice this means that for a given microscope objective much larger curvatures could be achieved with an Airy beam, see Fig. 6.1.

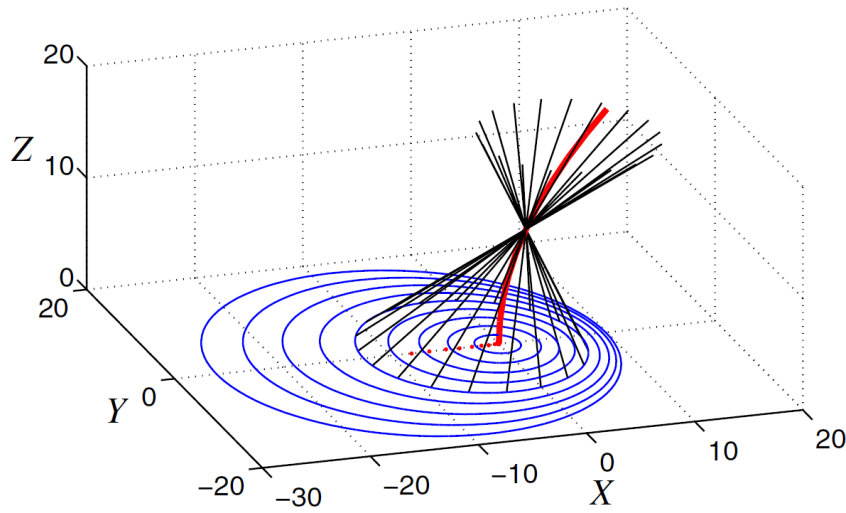


FIGURE D.2: Focussing concept for an accelerated Bessel beam, showing the cone mapping of the loci (blue) on the input plane that contribute to a different points along the focal line (red) respectively [Chr+12].

D.3 Oblong Airy beam

The parameters that have been used in previous glass cutting experiments with the “oblong” Airy beam are summarized in Tab. D.1.

Parameter	Value
Laser wavelength λ [nm]	1064
Focal length f [mm]	15
Cubic phase scale factor β [mm ⁻¹]	1.06* [†]
Width of Gaussian input beam $(2w_x, 2w_y)$ [mm]	(8, 24)
Half width of phase shift region x_π [mm]	n/a
Size Spatial light modulator [mm ²]	10.7 × 17.6
Focal contrast standard Airy	1.6
Focal contrast improved Airy	3.6

* in front of microscope objective, not directly given, inferred from other values

TABLE D.1: Parameters of the oblong Airy in [UL21].

Acknowledgements

I thank my supervisors Prof. Dr. Stefan Skupin and Dr. Jens Ulrich Thomas for their continuous support and encouragement. In particular, I thank Stefan for the in depth discussions concerning non linear optics and the numerical simulations as well as the efficient and enjoyable digital collaboration, and Jens for making sure I would have everything that I need for the experimental part of this study as well as his effective use of the red pen when it comes to text work.

I thank Wiebke Schöttler for the creative collaboration at the laboratory setup, machine whisperer Michael Kluge for trust and support and Dr. Andreas Koglbauer for gripping corridor chats about laser physics. For the friendly and inspiring working conditions at SCHOTT I thank all past and present colleagues, especially those of the post processing research group.

Thanks also go to Stefanie Zuerner for carrying out cleaving trials on the stepped roll and to Vanessa Glaesser and Johan Hedman and their input with respect to Weibull analysis and analysis of simulation data respectively.

Last but not least I thank all people that have back me up morally during this work, especially Magdalena, Oliver and my parents.